THE UNIVERSITY *of* LIVERPOOL

Development of Advanced Power System Protection and Power Quality Measurement Algorithms Using Mathematical Morphology

Thesis submitted in accordance with the
requirements of the University of Liverpool
for the degree of Doctor of Philosophy

in

Electrical Engineering and Electronics

by

Zhen Lu, B.Eng., M.Sc.(Eng.)

October 2006

Development of Advanced Power System Protection and Power Quality Measurement Algorithms Using Mathematical Morphology

by

Zhen Lu

Acknowledgements

First and foremost, I wish to express my deepest appreciation and acknowledgement to my supervisor, Professor Q.H. Wu, for his support and guidance at every stage of this research. He not only provided a keen insight into this research, but also taught me innumerable lessons at the workings of academic research. His intellectual advice and encouragement were indispensable for this dissertation and I consider myself privileged to have had the opportunity to work under his guidance. I am also grateful to Mr. David Turner, for his guidance of language improvement during my graduate study.

I am deeply grateful to Dr. Wenhu Tang, Dr. Junqiu Feng and Mr. Shan He for all the help and support I received along the way. Also I would like to thank the members of the Intelligence Engineering and Automation Group, Ms. Wenjia Tang, Mr. Chen Ma, Mr. Zhen Yang, Mr. Mengshi Li, Mr. Almas Shintemiro and Ms. Tianyao Ji for their friendship and valuable discussions. Specially I would like to thank Dr. Jihong Wang for her helpful suggestions on my thesis revision.

Many thanks go to the Department of Electrical Engineering and Electronics in the University of Liverpool, for providing the research facilities that make it possible for me to conduct this research. I am indebted to both the University of Liverpool for the studentship (2003 – 2006) and University UK for the 'Overseas Research Students Awards Scheme' (2003 – 2006).

Finally, I wish to acknowledge the blessings and encouragement of my parents, my girlfriend, and my sister, whose love and support miles away was a constant source of encouragement, without which this research would not have been complete.

Abstract

The basic operating principles of the most common types of relays have not changed for more than half a century. The relays measure the fundamental frequency component and harmonics of signals from power systems as the major attributes of the operating principles. The Fourier transform is commonly applied for measuring these attributes in a long and fixed sampling window of the continues signals. However, complex calculations of the Fourier transform have to be undertaken during each sampling interval. These calculations introduce many problems for the relay performance, in terms of fast response, accuracy and reliability. As a result, there is a need for a next generation relay which is more reliable and faster than the conventional relays.

This thesis is concerned with the development of a new generation of protection relaying system for power systems, based on *Mathematical Morphology* (MM). MM is a nonlinear signal processing technique derived from set theory and geometry. It analyses signals in terms of shape by retrieving the features of the signals using a pre-defined Structuring Element (SE). Mathematical morphological operations have been applied successfully to a wide range of fields including image enhancement, image restoration, edge detection, texture analysis and noise reduction, *etc.*

The accuracy of estimating the fundamental frequency component from a signal is crucial for protection relays. The current and voltage signals contain large harmonics and DC offset during the fault period. The presence of the exponentially decaying DC offset in the signals affects the accuracy of the estimation. A method that takes advantages of morphological operations, is developed for the removal of the exponentially decaying DC offset. This method

is very effective to solve the distortion problem of signals and improves the accuracy of the estimation of the fundamental component. As a result, the reliability of the protection relays is improved.

Apart from the method mentioned above, a morphological multi-resolution decomposition scheme is implemented for the discrimination of magnetising inrush current waveform from internal fault conditions for large power transformers. The scheme is presented to decompose current waveforms into a group of peaks and valleys which explore the features of currents in details. It is able to distinguish the internal fault and inrush currents reliably. More importantly, the scheme works satisfactorily using a sampling window which is much shorter than that adopted by the conventional methods, *i.e.*, the second harmonics restraint principle.

With the combination of advantages offered by lifting schemes, a new class of mathematical morphological schemes called Morphological Lifting Schemes (MLSs) is developed for protection purposes. One of MLSs is designed for Current Transformer (CT) saturation detection and compensation. In a CT, the shape of the secondary current waveform is severely distorted when the CT is forced into deep saturation. The morphological lifting scheme can extract features contained in the waveform of the current. The points of the inflection in the secondary current waveform are found with the scheme applied. Based upon the detection results, a compensation algorithm is presented to reconstruct healthy secondary current waveforms. For the purpose of improving the reliability of Ultra-High-Speed (UHS) protection relays for Extra-High-Voltage (EHV) transmission lines, another MLS is applied to the feature extraction from a travelling-wave signal. The MLS focuses on eliminating noise in a noise-contaminated travelling wave, while preserves the gradients of wavefronts. With the MLS used, the wavefronts can be captured precisely. The accurate response can be provided to the protection relays of the transmission lines under different fault types and positions in a noisy environment.

The problem of electric power quality has received growing interest in recent years due to the proliferation of sensitive electronic loads in power systems. As

another aspect of this thesis, it deals with the application of MM to power quality monitoring. Firstly, a brief introduction of power quality is presented and the description of power quality problems is given; and then the approaches based on MM are proposed to investigate the power quality problems, including the power disturbance identification and harmonic estimation.

In order to detect and classify different power disturbances, a method adopting morphological operations is applied to extract the features of disturbances from the signals in the time domain, and to detect the location and duration of the disturbances. The extracted features are used to classify different power disturbances. The method can localise the disturbances even in a noisy environment, and also able to be implemented in real-time due to the fast calculation of morphological operations.

A growing interest has been placed to inter-harmonics and sub-harmonics by investigating the distortion of current and voltage waveforms in power systems. It has been shown that great difficulties arise in the inter-harmonics or sub-harmonics detection and measurement with acceptable levels of accuracy, due to the spectral leakage and the resolution limit of Fourier transform. A morphological low-pass filter, is constructed for the accurate estimation of harmonics and detection of inter-harmonics or sub-harmonics. Furthermore, the filter is applied to extract a sub-harmonic component, from a ferroresonant voltage of a power transformer.

At the end of the thesis, a systematic summary is given, and further research work is suggested. The major contribution of the work in this thesis is the utilisation of the advanced performance of MM for feature enhancement, extraction and noise suppression in signals of power systems. This thesis mainly describes, for the first time, original work on the systemic application of MM to various protection relays, which may lead to the development of the next generation of power protection relaying system.

Contents

List of Figures

List of Tables

List of symbols and abbreviations

Symbols

$\in$	Element of
$\notin$	Not an element of
$\subset$	Contained in
$\subseteq$	Contained in or equals
$\supset$	Contains
$\supseteq$	Contains or equals
$\cap$	Intersection
$\cup$	Union
$\forall$	Universal quantifier
$\oplus$	Dilation
$\ominus$	Erosion
$\circ$	Opening
$\bullet$	Closing
E	Arbitrary set
$\mathbb{E}$	Arbitrary group of E
$\mathbb{E}^d$	The d-dimensional product of $\mathbb{E}$
$\rho(\mathbb{E}^d)$	Power set of $\mathbb{E}^d$
$\mathbb{R}^d$	The d-dimensional product of real numbers
$\mathbb{Z}^d$	The d-dimensional product of discrete integers
G_x	The translation of G by a vector $\overrightarrow{x}$
$\check{G}$	The reflection of G around its origin

G^c	The complement of G
$A \setminus B$	Set difference
$A \oplus B$	Binary dilation of A by B
$A \ominus B$	Binary erosion of A by B
$A \circ B$	Binary opening of A by B
$A \bullet B$	Binary closing of A by B
$a \oplus b$	Grey-scale dilation of a by b
$a \ominus b$	Grey-scale erosion of a by b
$a \circ b$	Grey-scale opening of a by b
$a \bullet b$	Grey-scale closing of a by b
g	Morphological gradient
g^-	Internal morphological gradient
g^+	External morphological gradient
ψ	A morphological filter
$E_d(A)$	The dilation residual edge of image A
$E_e(A)$	The erosion residual edge of image A
$TH_o(A)$	The opening top-hat transformation of image A
$TH_c(A)$	The closing top-hat transformation of image I
$S(A)$	The skeleton of A
$\psi^{\downarrow}$	Synthesis operator
$\psi^{\uparrow}$	Analysis operator
$\bigvee$	Supremum
$\bigwedge$	Infimum
∇	Derivative
$H(z)$	Low-pass filter
$G(z)$	High-pass filter
$\widetilde{H}(z)$	Synthesis low-pass filter
$\widetilde{G}(z)$	Synthesis high-pass filter
$c[n]$	Scaling coefficients
$d[n]$	Wavelet coefficients
P	Predictor operator
U	Update operator

Abbreviations

ANSI	American National Standards Institute
ATP	Alternative Transients Program, a power system simulation software
CBEMA	Computer Business Equipment Manufacturers Association
CT	Current Transformer
Daub	Daubechies Wavelets
DIP	Delft Image Processor
DFT	Discrete Fourier Transform
DWT	Discrete Wavelet Transform
EHV	Extra-High-Voltage
EPRI	Electrical Power Research Institute
EMC	Electro Magnetic Compatibility
EMD	Empirical Mode Decomposition
EMTDC/PSCAD	Power system simulation softwares
FFT	Fast Fourier Transform
FIR	Finite Impulse Response
GPS	Global Positioning System
HT	Hilbert Transform
IEC	International Electrotechnical Commission
IEEE	Institute of Electrical and Electronics Engineers
IIR	Infinite Impulse Response
IMF	Intrinsic Mode Functions
LSE	Least Squares Error
ITE	Information Technology Equipment
ITI	Information Technology Industry
MATLAB	A programming language for scientific research
MF	Morphological Filter
MG	Morphological Gradient

MLS	Morphological Lifting Scheme
MM	Mathematical Morphology
MMF	Morphological Mean Filter
MMG	Multi-resolution Morphological Gradient
NEMA	Nation Electrical Manufactures Association
NFPA	National Fire Protection Association
PLL	Phase Locked Loop
RMS	Root Mean Square
SC	Series Compensation
SE	Structuring Element
SNR	Signal to Noise Ratio
STFT	Short-Time discrete Fourier Transform
UHV	Ultra-High-Speed
VLSI	Very-Large-Scale Integration
VT	Voltage Transformer
WT	Wavelet Transform

Chapter 1

Introduction

1.1 Overview of power protection systems

In a large power system network comprising of hundreds of complex interacting elements, there always exists a possibility of disturbance and fault. The operations of early fault identification and rapid equipment isolation are imperative to maintain the reliability and integrity of the system. The failure of insulation or breaking of conductors and accidents may bring extensive damage to the equipment and interruption in the power supply to the customers. To minimise these problems, power system equipment must be protected adequately. Protection relays are designed and applied in power systems to protect equipment from excessive damage and to maintain system integrity and stability. The function of a protection relay in association with a circuit breaker is to remove the system element as quickly as possible from which a fault has been developed. Fast and correct protection relays resume power supply swiftly, which can improve system reliability and safety.

Besides speed, the other three important features of a satisfactory protection relay are reliability, selectivity and sensitivity. Reliability of a protection relay is defined as the probability that the system will function correctly when required to act. The reliability has two aspects: first, the system must operate in the presence of a fault that is within its protection zone, and secondly, it

must refrain from unnecessary operations when the fault is outside its protective zone or there is no fault at all. Selectivity refers to the overall design of protective strategy wherein only those protective devices closest to a fault will operate to isolate the faulted component. Sensitivity depicts the ability of the system to identify an abnormal condition that exceeds a nominal "pickup" or detection threshold values. The system will initiate protection action as the sensed quantities exceed the threshold.

1.2 Early developments of protection relays

The fuse was the first form of protection for power apparatus in early electrical power systems. It was constructed from a piece of copper designed to melt when excessive current flowing through it. As power systems have been rapidly developed, the fuse element could no longer provide adequate and satisfactory protection for power systems. Consequently, electro-mechanical technology-based relays replaced the fuse to protect power systems. However, these relays suffered from several associated disadvantages like long operating time due to the inertia of moving parts, high burden on Current and Voltage Transformers (CTs and VTs) and high maintenance cost, which made it necessary to use more sophisticated relaying techniques.

Static relays were the next generation used. The fabrication of static relays using solid-state components was an improvement over the electro-mechanical relays. Some of the drawbacks of the electro-mechanical relays were eliminated, but the static relays still suffered from other limitations such as sensitivity to temperature and voltage spikes, aging of components and damage due to overloading. The early designs of static relays were vacuum tube devices, which were introduced in the 1930s. These systems required considerable maintenance and were not as reliable as electro-mechanical relays. Hence, their applications were limited. In the early 1950s, transistor-based relays became available and immediately provided reliable protection for power system, which made the static relays begin to disappear in quantity in the mid-1960s.

Associated with the development of integrated operational amplifiers, integrated relays are devised to improve the capabilities of relays. Integrated relays are similar to static relays in design and function, but using integrated circuits rather than discrete components. Integrated circuitry allows these relays to combine together the three-phase current protection, metering, communication, control and monitoring capabilities.

The first digital relay was developed and reported by Rockfeller in the earlier 1980s [1]. Much literature reported digital relays shortly afterwards. Nowadays, the concept of digital relays has grown rapidly as digital computers become more powerful, reliable and cheaper. The inherent features of a digital relay, such as memory action and complex shaping of operational characteristics, lead to better performance and the integration of diagnostic functions make the relay much more reliable. The feature of advanced programmable functions maximise the flexibility and monitoring capabilities as well. The microprocessor replaces most of the electronic circuitry, thereby maximising integration of advanced protection functions, control, monitoring, alarms, metering and communication into a single device. In comparison with electro-mechanical and static relays, digital relays have a higher immunity to electromagnetic fields and transients and can be adapted to a wider range of operating temperatures.

A typical digital relay has a measurement unit and a computation unit. The former is comprised of data acquisition, conversion and storage; the latter executes the relaying algorithm with the data provided by the measurement unit. The process of measurement, fault computation and decision making are completed within the time interval between consecutive data sampling instants.

1.3 Recent developments of protection schemes

The introduction of digital relays offers the possibility in developing new protection techniques in power systems. Over the last 30 years, much attention has been paid to the development of new protection algorithms for different

power system equipment.

1.3.1 Adaptive protection

Study on adaptive protection relay began in the 1980s [2]. With the development of computers, communication and artificial intelligence technology, realisation of adaptive protection relaying systems have become possible. A function within a protection relay or system that automatically adjusts the operating characteristics of the relaying system in response to changing power system conditions can be said to be adaptive. The adaptive protection can automatically find the optimal condition depending on relay settings and alter the protection settings, functions and characteristics online. It makes the digital relays on-line changes possible by computing and transmitting new operating parameters from a central site or from an expanded communication system. Various adaptive protections have been developed since the 1980s: rapid coordination calculation experiments; use of synchronised phasor measurement [3]; circuit breaker auto re-closure [4] and transformer protection; agent, decision trees and wide-area based protection systems [5].

1.3.2 Protection based on transient signals

The introduction of Extra-High-Voltage (EHV) transmission lines to the modern power system brings new and relatively difficult problems, which require the fast fault clearance to improve the system stability. The development of transient-based protection systems for transmission lines started in the late 1970s [6]. Considerable efforts have been made to research the detection of fault generated transients and have covered many aspects of power system protection.

Transient-based protection detects the occurrence of a fault by measuring high frequency transient current or voltage signals generated by the fault. The transient signals are directly extracted from the CTs or VTs, by using fast signal processing algorithms [7]. The fault can be identified accurately and

rapidly, without the effect of fault path impedance, power swing or Current Transformer (CT) saturation. These transient-based techniques have been developed and applied in the fields of fault location, power line protection, power apparatus protection and circuit breaker auto re-closure, *etc* [8][9].

1.3.3 The applications of artificial neural network in protection

Artificial Neural Networks (ANNs) are biologically inspired; that is, they are composed of elements that perform in a manner that is analogous to the most elementary functions of the biological neuron. These elements are then organised in a way that may be related to the anatomy of the human brain. From the engineering point of view, ANN, which is a technique of large scale pattern, may have any number of variables, so that it can detect and respond to all the parameters describing the process studied and determine its current state. Successful applications of ANN in engineering have demonstrated that this tool can be utilised as an alternative method to solve problems accurately and efficiently.

ANNs have demonstrated their potential in terms of non-linearity, generalisation, prediction capabilities and handling complex interactions of time varying voltages and currents under fault conditions. Numerous applications based on ANN have been developed for power system protection, which include: directional protection, distance protection, differential protection, circuit breaker re-closure [10], fault location, phase selection [11] and unit protection [12]. These ANN-based techniques improve the performance of protection relaying system greatly.

1.3.4 Wavelet transform methods

Wavelet Transform (WT) is a new powerful mathematical tool introduced for digital signal processing. It has attracted great attention, and become more and more popular since the 1980s [13]. The WT procedure is to adopt a wavelet

prototype function, called "analysing wavelet" or "mother wavelet". Temporal analysis is performed with a contracted, high-frequency version of the prototype wavelet, while frequency analysis is performed with a detailed, low-frequency version of the prototype wavelet. Compared to Fourier-based techniques, which rely on a single basis function, WT has a number of prototype basis functions for selection. An appropriate wavelet function is selected as a mother wavelet to perform analysis based on the shift and dilation of the selected wavelet.

The main attribution of WT is the ability of not only decomposing a signal into its frequency components, but also providing a non-uniform division of the frequency domain, whereby it focuses on short time intervals for high frequency components and long intervals for low frequencies. WT provides a powerful time-frequency localisation property along with signal decomposition.

Multi-resolution analysis of WT refers to the procedures for obtaining low-pass approximations and band-pass details from original signals. An approximation contains the general trend of original signal while a detail embodies the high-frequency contents. The original signal is divided into different scales of approximations and details through a succession of convolution processes. It is useful for the detection and analysis of signal features, especially for analysing transient phenomena such as those associated with line faults or switching operations, since it has the ability to analyse a localised area of a signal and reveal aspects of data like break points or discontinuities. Thus WT is useful in detecting the onset of a fault, which has been widely applied in power system protection including high impedance fault detection [14], fault-phase identification [15], travelling wave fault location [16] and directional transformer protection [17].

1.4 The development of protection relays using Mathematical Morphology

Mathematical Morphology (MM) was introduced in 1964 by Matheron [18] and Serra [19][20], both researchers at the Paris School of Mines in Fontainebleau.

Their objective was to characterise physical or mechanical properties of certain materials, such as the permeability of porous media, by examining the geometrical structure [21]. In that year, they both published their first reports concerning some of the methods that are part of MM now. Matheron rediscovered Minkowski algebra, which defined the set addition (dilation) in 1903. In that period, Matheron had undertaken the study of permeability for porous media in relation with their geometry on a more theoretical level [22]. The notion of a morphological opening and closing was introduced and associated with the convexity of the Structuring Element (SE), leading to granulometry. In January 1966, Serra finished the analysis of binary images using any SE based on straight lines along the three axes of the hexagonal grid. Later that year, Matheron and Serra coined the term "mathematical morphology". The centre of MM, founded on April 20, 1968, is considered as the birthplace of MM, which is still an important centre for research in the field today.

Since its launching in 1964, MM has grown rapidly in the seventies on the theoretical level. The major contribution of Matheron's work during this period includes topological foundations, random sets, increasing mappings, convexity and several models of random sets. Based on iterative processing, binary thinning, skeleton, ultimate erosion, conditional bisector and their geodesic framework were introduced. With the significant development of automated visual inspection, substantial developments in morphology were stimulated in 1980s. The most important development of MM in that period is the setting of the method in the mathematical framework of complete lattices. The theory of complete lattice provides a compact theoretical foundation for grey-scale morphological operations. The theory of morphological filtering was also presented in eighties. Some real-time applications of morphological filtering were developed, such as Delft Image Processor (DIP). In nineties, the growth of MM was focused on its applications, which include robot vision, medical imaging, visual inspection, texture and scene analysis *etc.* The theoretical works on the concept of connection, in combination with the connected filters have made MM a remarkable powerful tool for segmentation. Slope transform was developed by

endowing morphological operators with eigenfunctions and their related transfer functions. Furthermore, a relatively new approach of MM, soft morphology was introduced by Koskinen [23]. The recent trends in soft morphology including the algorithms and implementations can be found in [24] and [25]. Other extensions of MM include fuzzy morphologies, which attempt to apply fuzzy set theory to MM [26, 27, 28]. With over three decades of development, MM has become a powerful tool for geometrical shape analysis.

In the field of signal processing, MM prefers to depict the profile of signal waveform in the pure time domain rather than most filtering methodologies such as WT emphasising on the response of frequency domain. The underlying basis of the morphological filtering technique is to process signals by a function, known as the SE or the structuring function generally. An SE slides through the signal as a moving window, inspects its interaction with the signal, and detects specific features in the neighbourhood of every point in the signal. A mathematical morphological filter is composed of various combination of fundamental morphological operators, which can preserve or suppress the feature represented by SE and obtain a signal with only components of interest. When operating upon a signal of complicated shapes, morphological filters are capable of decomposing a signal into certain parts with specific purposes and highlighting them from the background.

A transient signal is normally generated with a fault occurred in a transmission line. It is always represented as the foreground in comparison with the steady-state fundamental signal, which acts as the background. Mathematical morphological techniques have the ability to characterise and recognise the unique features of the transient signal, which are a series of sudden changes superimposed on the fundamental waveform. With the help of the morphological techniques, a new generation of protection relays, called morphological protection relays, are developed. Both the reliability and the accuracy of the protection system are effectively improved.

1.5 Motivation and objective

In contrast with the integral transform algorithms, such as Fourier transform and WT, morphological operators handle a signal in a completely different way. A signal is able to be decomposed into meaningful parts by morphological operators. These parts are separated from the background for identification or other purposes, and the main shape characteristics of the signal are preserved. Unlike WT decomposing a signal into parts of different frequency bands, the morphological operators process a signal by a function known as an SE in general or a structuring function for a 1-D signal. The technique is able to preserve or suppress the feature represented by the SE and obtain a signal with only components of interest. Therefore, for a distorted signal, its underlying shapes are able to be identified, reconstructed and enhanced. Furthermore, the mathematical calculation involved in MM includes only addition, subtraction, maximum and minimum operations, without any multiplication or division. Hence, morphological operators calculate faster than traditional integral transforms when processing the same signal.

The basic principle of the design and operation of protection relays has not changed for more than half a century, even after the introduction of digital relays to replace their analogue counterparts. All power system protection relays measure the fundamental frequency and harmonics of the signals from the power system using mathematical integral transforms, such as the Fourier transform and WT. These integral transform based algorithms have difficulty in satisfying the demands for high speed protection purposes where fast relay action to faults is playing a crucial role for power system stability. For most of the protection relays, complex calculations of integral transform coefficients, relevant to the attributes of fault signals and fault conditions, have to be undertaken within a sampling interval. These calculations introduce many problems for the relay performance, such as accuracy, fast responses, noise, disturbance rejections and reliability.

The concept of MM is systematically and comprehensively introduced in the design of different algorithms for protection relays. An attempt to apply

a morphological filter to fault currents or voltages has been made, aiming at extracting the exponentially decaying DC components from the fault current or voltage signals. With the help of the morphological filter, the accuracy of the estimation of fundamental frequency components in fault currents or voltages is effectively improved. Furthermore, a multi-resolution morphological filter is constructed for the identification of transformer magnetising inrush currents. An inrush current is decomposed into a series of peaks and valleys, which represent the different characteristics between the inrush and fault currents. Compared with the Fourier-based protection schemes which estimate the contents of the second harmonics of the currents, the trip time of the protection relays for transformer is significantly reduced with the application of the morphological filter.

CT saturation is an important problem of protection relays. It produces distorted secondary currents which cause protection relays' mal-operation or even prevent tripping. By combining the morphological filter technique with the concept of lifting schemes, a Morphological Lifting Scheme (MLS) is applied for the detection of CT saturation. With the advantage of shape recognition of morphological operators, the distorted sections in the secondary currents are discriminated from the healthy ones. In addition, an attempt to employ an MLS to enhance the reliability and sensitivity of EHV transmission line protection has been made. As a tool with the ability of features extraction, the scheme can distinguish between wavefronts and noises in travelling waves. The noises are eliminated and the accuracy of the wavefronts location is improved.

Power quality is an important issue for modern power systems. The power quality problem is represented as different distortion in current or voltage waveforms. It can cause system equipment malfunction, computer data loss and erratic operation of electronic controls. Fourier transform has been regarded as the basis of modern spectral and harmonic analysis. However, it can not provide any information of signals in the time domain. Time-frequency information of the signal is very important, since in power quality analysis, some particular distorted portions are most important and time-frequency informa-

tion is needed simultaneously for this particular portion of the signal. For the purpose of analysing different power quality problems effectively, a number of methods are developed based on MM. With the application of a designed morphological operation, various types of disturbances are detected and classified online in a noisy environment. In addition, a multi-resolution morphological low-pass filter is implemented for harmonic estimation and sub-harmonic detection based on instantaneous reactive power theory. These methods provide us a new methodology for power quality monitoring.

1.6 Major contributions of this thesis

The major contributions arising from this research are the utilisation of the advanced performance of MM for feature enhancement, extraction, noise suppression and background normalisation. MM is systemically introduced as a new methodology to decompose signals based on the features in the time domain instead of frequency domain, which is adopted by conventional integral methods. This thesis initiatively investigates the application of MM to power system protection relays and power quality monitoring. The contributions concentrate on the following topics:

- For the first time, a method based on MM is developed and implemented for the removal of exponentially decaying DC components from post-fault current or voltage waveforms. It improves the accuracy of the estimation of fundamental frequency components and harmonics, which are the basis of operating principles for digital protection relays.

- The identification of inrush currents is a difficult problem for transformer protection relays. In this thesis, a morphological decomposition operation is applied to discriminate between transformer inrush and internal fault currents. The method provides fast identification of inrush even when there are only low levels of the second harmonic content. The non-linear morphological operators also reduce the computational complexity.

- The advancement of lifting schemes provides us a methodology to construct non-linear wavelets. Based on the theory of MM and lifting schemes, two MLSs are designed for the detection of CT saturation and the noise elimination for EHV transmission line protection relays. These schemes inherit the merits of the multi-dimension and multi-level analysis of the lifting scheme for wavelets, and extend the original wavelet from linear domain to non-linear domain with the applications of morphological operators.

- Initial investigation of MM is made in power quality analysis [29, 30, 31]. A morphological scheme is constructed for the detection and classification of power disturbances. The features of different power disturbances can be extracted by a pre-defined morphological operation. Based on these extracted features, the power disturbances could be accurately located, and further classified according to the extracted features.

- A morphological filter is implemented to protection relays for the estimation of harmonics and the detection of inter-harmonics [32]. The fundamental frequency components including integral harmonics are able to be transformed into DC components by a coordinate transformation. The morphological-based DC filter is developed to estimate the harmonic components effectively.

1.7 Overview of this thesis

This thesis is structured as follows:

Chapter 2 This chapter introduces the theoretical background of MM, which starts with a review of basic morphological operators. With the understanding of basic morphological operators, other useful operations such as morphological gradient, top-hat transform, skeleton are introduced. In addition, the design of a morphological filter is theoretically presented. The construction of morphological wavelets is also discussed. Further-

more, the concept and construction of lifting schemes are presented in this chapter.

Chapter 3 In this chapter, a morphological filter is constructed especially for the extraction of exponentially decaying DC components from a signal. The filter removes the DC components from their background, the post-fault currents or voltages. The accuracy of the estimation of fundamental frequency components from distorted currents or voltages, is improved by the application of this method.

Chapter 4 This chapter introduces a scheme using a morphological multi-resolution operator for the identification of transformer magnetising in-rush currents. A brief introduction of the transformer protection is firstly given, followed by the theoretical description of the produce of inrush transients. The proposed scheme is then described, which is to discriminate the inrush current from internal fault conditions by using the morphological operator to decompose the current waveform into a series of valleys and peaks. By quantifying these extracted valleys or peaks, the inrush current is then identified with a simple criterion.

Chapter 5 This chapter presents the design and implementation of an MLS for on-line CT saturation detection and compensation. The scheme is able to discriminate the saturation periods from the secondary currents directly. Firstly, a simple introduction of the characteristics of CT is given, and then the scheme is constructed according to the features of saturation using both the advantages of lifting schemes and MM. Furthermore, a compensation algorithm is developed based upon the detection results. The simulation results on a sample power system indicate that the proposed scheme can successfully detect and compensate the distorted secondary current of a saturated CT without a prior knowledge of parameters.

Chapter 6 Another designed MLS is presented for noise reduction in EHV transmission line protection in this chapter. Aiming at eliminating the

noise, and preserving the features of wavefronts as well, an MLS is designed for both of noise elimination and wavefront identification. The principle of transient-based protection is simply introduced at the beginning of the chapter, followed by the scheme, which is given step by step. Typical EHV transmission system simulation models are set for the validation of the scheme. The conducted simulation results show that the scheme is capable of providing accurate responses under various fault conditions. The comparison results represent the advantages of the proposed scheme.

Chapter 7 The basic concepts of power quality, including its definition, standards and disturbance types are introduced in this chapter. For transient disturbances, a Morphological Mean Filter (MMF) and a Multi-resolution Morphological Gradient (MMG) are described for the development of a method to extract features from disturbances in a noisy environment. The extracted features are used for the further disturbance classification. The simulation results of applying the morphological approach to different types of simulated power disturbances are given. The results indicate that the proposed method is effective for power quality analysis. Another powerful tool, named Empirical Mode Decomposition (EMD), is also presented and applied for power quality monitoring in this chapter. Firstly, the theoretical background of EMD is briefly introduced and analysed. Then the technique is presented in details and used for power quality monitoring. Finally the practicality and advantages of the EMD method are discussed.

Chapter 8 This chapter describes the application of a morphological filter for the estimation of power system harmonics and detection of interharmonics. With a coordinate transformation based on instantaneous reactive power theory, all integral harmonics including fundamental frequency components are transformed into DC components in another coordinate. Therefore, these components are able to be extracted by a

morphological low-pass filter. This method also provides a solution for the detection of inter-harmonics in a transformer ferroresonance voltage.

Chapter 9 The development of a multi-resolution morphological filter, based on the theory of MM and multi-resolution decomposition schemes is presented in this chapter. The filter is flexible and adaptive. It has better performance in eliminating pulse noise compared with linear filters.

Chapter 10 This chapter concludes this thesis and some suggestions are given for future work.

1.8 Auto-bibliography

1. **Z. Lu**, D.R. Turner, Q.H. Wu, J. Fitch, S. Mann. Morphological transform for detection of power quality disturbances, *2004 International Conference on Power System Technology, PowerCon 2004*, Singapore, Vol. 2, pp. 1644 - 1649, 21-24 Nov., 2004.

2. **Z. Lu**, J.S. Smith, Q.H. Wu and J. Fitch. Empirical mode decomposition for power quality monitoring, *Transmission and Distribution Conference and Exhibition: Asia and Pacific, 2005 IEEE/PES*, Dalian, China, pp. 1-5, 15-18 Aug., 2005.

3. **Z. Lu**, Q.H. Wu and J. Fitch. A morphological filter for estimation of power system harmonics, *2006 International Conference on Power System Technology, Powercon 2006*, Chongqing, China, pp. 1-6, 22-26 Oct., 2006.

4. Z. Yang, **Z. Lu**, C. Ma, Q.H. Wu and J. Fitch. Improving control ability of relay protection system with intelligent agents, *2006 International Conference on Power System Technology, Powercon 2006*, Chongqing, China, pp. 1-6, 22-26 Oct., 2006.

5. **Z. Lu**, J.S. Smith, Q.H. Wu and J. Fitch. Identification of power disturbances using morphological transform, *Transactions of the Institute*

of Measurement and Control, to appear in 2006.

6. **Z. Lu**, J.S. Smith and Q.H. Wu. Morphological lifting scheme for current transformer saturation detection and compensation, submitted to *IEEE Transactions on Circuits and Systems-I: regular papers* in Jan., 2006.

7. **Z. Lu** and Q.H. Wu. EHV transmission line protection using a morphological lifting scheme, submitted to *IEEE Transactions on Power Delivery* in Jul., 2006.

Chapter 2

Mathematical Morphology and The Lifting Scheme

2.1 Introduction

From a general scientific perspective, the word *morphology* refers to the study of forms and structures. The goal of MM is to investigate the geometrical structure of sets. This chapter reviews the basics of MM and introduces the morphological operators which will be used in the following chapters. A series of morphological operators, including dilation, erosion, opening and closing, are introduced.

2.2 Basic concepts of mathematical morphology

When first introduced, morphology was based on the set theory, which meant it was limited to quantitatively describing shape and size for binary images. In 1978, Nakagawa and Rosenfeld linked the binary dilation and erosion operations to the maximum and minimum filters applied to grey-value images [33]. The notion of umbra was also introduced by Sternberg around 1978, which made it possible to apply all the mathematics developed for binary images to

grey-scale images [34]. As a result of the pioneering work, nowadays MM has achieved the status of a powerful tool in image processing with applications in material science, microscopic imaging, pattern recognition, medical imaging, and computer vision, *etc.*

Given a set G defined in $\mathbb{E}^d$, where $\mathbb{E}^d$ is d-dimensional Euclidean space [35], the following definitions can be developed [36]:

- *Translation*: The translation of G by a vector x, denoted as G_x, is defined as:

$$G_x = \{g : g = a + x; a \in G\}. \tag{2.2.1}$$

- *Reflection*: The reflection of G based on its origin, denoted as $\check{G}$, is defined as:

$$\check{G} = \{-g : g \in G\}. \tag{2.2.2}$$

- *Complement*: The complement of G, denoted as G^c, is defined as:

$$G^c = \{g : g \notin G\}. \tag{2.2.3}$$

Letting two sets $A, B \subseteq \mathbb{E}^d$ represent the binary input set and the binary SE respectively, the dilation of A by the SE B can be developed as $A \oplus B$ with the definition of [36]:

$$A \oplus B = \bigcup_{b \in B} (A + b). \tag{2.2.4}$$

The opposite of dilation is known as erosion. The same as dilation, given two sets $A, B \subseteq \mathbb{E}^d$, A is the input set and B is the binary SE. The erosion can be developed as $A \ominus B$, its definition is [36]:

$$A \ominus B = \bigcap_{b \in B} (A - b). \tag{2.2.5}$$

To visualise the geometrical behaviour of binary dilation and erosion, it is helpful to consider two dimensional sets as depicted in Fig. 2.1. A circular SE, $B \subseteq \mathbb{E}^2$, the centre of which is the centre of the circle, slides as a probe across the image $A \subseteq \mathbb{E}^2$, testing the spatial nature of the image at every point.

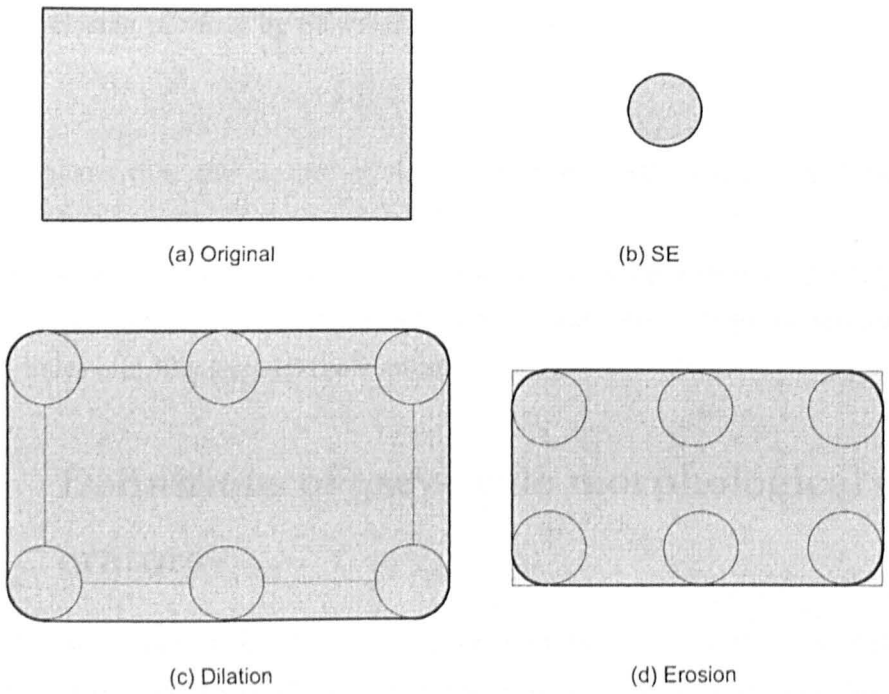

Figure 2.1: Dilation and erosion by a circular disc with the origin at the centre of the disc.

All the other morphological transforms are developed by composing the two basic morphological operators, dilation and erosion. The concepts of opening and closing are proposed by Matheron who studied them within the framework of an axiomatisation of the concept of size [18].

The opening of a set A by an SE B, denoted $A \circ B$, is defined as [18]:

$$A \circ B = (A \ominus B) \oplus B, \tag{2.2.6}$$

which means that the opening of A by B is simply the erosion of A by B, followed by a dilation of the result by B.

Opening breaks a connected feature into several unconnected parts and eliminate small peaks and islands. In image processing, opening can be used to smooth contours, break narrow isthmuses and eliminate small islands or sharp peaks by a disk SE.

The closing of set A by SE B, denoted $A \bullet B$, is defined as:

$$A \bullet B = (A \oplus B) \ominus B, \tag{2.2.7}$$

which means that the closing of A by B is simply the dilation of A by B, followed by a erosion of the result by B.

Closing is a morphological dual to opening. Closing also tends to smooth sections contours, but it fuses narrow breaks and long thin gulfs, eliminates small holes and fills gaps in the contour.

2.3 Definitions of grey-scale morphological operators

Grey-scale digital signal can be represented as sets defined in two dimensional discrete Euclidean space [35]. Grey-scale dilation, erosion, opening and closing can be obtained by extending binary morphology operators to grey-scale signals or images.

2.3.1 Grey-scale dilation and erosion

Let $a(n)$ and $b(n)$ denote an input signal and a 1-D grey-scale SE, where n is the discrete time index. D_a and D_b are the domains of $a(n)$ and $b(n)$ respectively. Grey-scale dilation of $a(n)$ by $b(n)$, denoted as $(a \oplus b)(n)$, is defined as:

$$(a \oplus b)(n) = \max_v \{a(n+v) + b(v)\}, \tag{2.3.1}$$

where $v \in D_b$ and $(n+v) \in D_a$. Note that $b(n)$ is now a function rather than a set. If $b(n)$ is flat (*i.e.*, $b(k) = 0, \forall k \in D_b$), the above equation can be simplified to:

$$(a \oplus b)(n) = \max_v \{a(n+v)\}. \tag{2.3.2}$$

Because dilation is based on choosing the maximum value from $a(n+v) + b(v)$ in the neighbourhood defined by the shape of the SE, the general effect of performing dilation on a grey-scale image/signal is:

- if all the values of the elements in the SE are positive, the output image turns to be brighter than the input;
- dark details are reduced even eliminated, depending on how their values and shapes relate to the SE.

Grey-scale erosion is denoted as $a \ominus b$. It is defined as:

$$(a \ominus b)(n) = \min_{v}\{a(n+v) - b(v)\}, \tag{2.3.3}$$

where $v \in D_b$ and $(n+v) \in D_a$. If the SE $b(n)$ is flat, then the equation can be simplified to:

$$(a \ominus b)(n) = \min_{v}\{a(n+v)\}. \tag{2.3.4}$$

Since erosion is based on choosing the minimum value of $(a(n+v)-b(v))$ in a neighbourhood defined by the shape of the SE, the general effect of performing dilation on a grey-scale image is:

- if all the elements of the SE are positive, the output image tends to be darker than the input image;
- bright details in the input image that are smaller in "area" than the SE are reduced to a certain degree determined by the grey values surrounding them.

2.3.2 Grey-scale opening and closing

Similar to binary operators, combining the grey-scale erosion and dilation, the operation of grey-scale opening and closing can be developed as:

$$(a \circ b)(n) = \max_{v}\{\min_{u}\{a(n+u-v) - b(u) + b(v)\}\}, \tag{2.3.5}$$

$$(a \bullet b)(n) = \min_{v}\{\max_{u}\{a(n-u+v) + b(u) - b(v)\}\}, \tag{2.3.6}$$

where $u, v \in D_b$ and $(n+u-v)$, $(n-u+v) \in D_a$. If the SE is flat, the above equations are simplified to:

$$(a \circ b)(n) = \max_{v}\{\min_{u}\{a(n+u-v)\}\}, \tag{2.3.7}$$

$$(a \bullet b)(n) = \min_{v}\{\max_{u}\{a(n-u+v)\}\}. \tag{2.3.8}$$

2.4 Other morphological operators

2.4.1 Morphological gradient

In addition to the operations discussed earlier, dilation and erosion are often used to calculate the basic Morphological Gradient (MG) of an image or signal, denoted as g:

$$g = (a \oplus b) - (a \ominus b), \tag{2.4.1}$$

where, a is original image or signal and b is the SE. There are also two kinds of half-gradient. One is called internal gradient, denoted as g^-, which is defined as the difference between the original signal or image and the eroded result:

$$g^- = a - (a \ominus b). \tag{2.4.2}$$

The other one is external gradient g^+, which is defined as the difference between the dilated result and the original signal or image:

$$g^+ = (a \oplus b) - a. \tag{2.4.3}$$

Morphological gradients are effective transforation tools to extract the sudden changes in processing a signal.

2.4.2 Top-hat transformation

The edge of image A, denoted by $E_d(A)$, can be defined as the difference of the dilation domain of A and the domain of A. This is also known as dilation residue edge detector:

$$E_d(A) = (A \oplus B) - A. \tag{2.4.4}$$

Equivalently, the edge of image A, denoted by $E_e(A)$, can also be defined as the difference set of domain of A and the erosion domain of A. This is also known as erosion residue edge detector:

$$E_e(A) = A - (A \ominus B). \tag{2.4.5}$$

The opening top-hat transformation of image A, denoted as $\mathrm{TH}_o(A)$, is defined as the difference set of the domain of A and the opening domain of A. It is defined as:

$$\mathrm{TH}_o(A) = A - (A \circ B). \tag{2.4.6}$$

Similarly, the closing top-hat transformation of image I, denoted as $\mathrm{TH}_c(A)$, can also be defined as the difference set of the closing domain of A and the domain of A. It is defined as:

$$\mathrm{TH}_c(A) = (A \bullet B) - A. \tag{2.4.7}$$

2.4.3 Skeleton

Suppose A is a continues set in d-dimension. Then the skeleton of A, denoted as $S(A)$, is the set of the centres of the maximum open balls [37] ρB_o contained in A. Similarly, we denote $s_p(A)$ as the set of centres of a maximum open balls of radius $\rho > 0$ (B_o is the open unit ball).

Such maximum balls do exist, since every limit of open balls contained in A is an open ball. Then by Zorn's lemma [38], every open ball contained in A is also contained in the maximum open ball.

So $S(A)$ can be defined as [20]:

$$S(A) = \bigcup_n \{S(A;n) : n = 0, 1, 2 \cdots\}. \tag{2.4.8}$$

It can be proved that:

$$S(A;n) = (A \ominus nB) \setminus [(A \ominus nB) \circ B]. \tag{2.4.9}$$

So $S(A)$ can be expressed to:

$$S(A) = \bigcup \{(A \ominus nB) \setminus [(A \ominus nB) \circ B]\}. \tag{2.4.10}$$

The datum of set A is equivalent to that of its skeleton $S(A)$, together with the maximum radius ρ associated with each point of $S(A)$. The maximum radius function is the restriction to $S(A)$ of the quench function [19].

2.5 Morphological filters

A morphological filter is an increasing operator ψ which is idempotent: $\psi^2 = \psi$ [39]. It locally modifies the geometrical features of signals or image objects. In MM, a transformation or operator is called a filter if it is increasing and idempotent.

Two well-known classes of morphological filters are openings and closings. It is easy to prove that both opening and closing satisfy the properties of increasing and idempotent.

Probably the most well-known method to construct morphological filters other than openings and closings, is composed by the two classes, such as:

$$\psi = (a \circ b) \cdot (a \bullet b), \tag{2.5.1}$$

$$\psi = (a \bullet b) \cdot (a \circ b), \tag{2.5.2}$$

or:

$$\psi = [(a \circ b) \cdot (a \bullet b) + (a \bullet b) \cdot (a \circ b)]/2. \tag{2.5.3}$$

These morphological filters are widely used to eliminate noise in signals or image [40][41].

2.6 Morphological wavelets

For a long time, it has been recognised that multi-resolution signal decomposition schemes provide convenient and effective ways to process information. Pyramids, wavelets, multi-rate filter banks, granulometries, and skeletons are among the most common tools for constructing multi-resolution signal decomposition schemes [42][43].

A popular way to get a multi-resolution signal decomposition scheme is to smooth the given signal using a linear low-pass filter, so as to remove high frequencies, and sub-sample the result in order to obtain a reduced-scale version of the original signal. A collection of signals at decreasing scale can thus be produced by repeating this process. These signals, stacked on top of each

other, form a basic signal decomposition scheme, known as the multi-resolution pyramid.

From a frequency point of view, the resulting detail signals form a signal decomposition in terms of high-pass-filtered copies of the original signal. The original signal can be reconstructed from the detail signals. So the detail signals provide a multi-resolution signal representation that guarantees perfect reconstruction. One of the best known examples of such a scheme is the Laplacian pyramid of Burt and Adelson [44].

To obtain a mathematical representation for a multi-resolution signal decomposition scheme, we need a sequence of signal domains, assigned at each level of the scheme, and analysis/synthesis operators that map information between the different levels. The analysis operators are designed to reduce information in order to simplify signal representation whereas the synthesis operators are designed to undo the decomposition process and resume the information. It is a widely accepted approach to multi-resolution signal decomposition.

Let j be an index set indicating the levels in a multi-resolution signal decomposition scheme. A domain V_j of signals is assigned at each level j. In this framework, signal analysis consists of decomposing a signal by increasing the level j. This task is accomplished by analysis operators $\psi_j^{\uparrow} : V_j \rightarrow V_{j+1}$. On the other hand, signal synthesis proceeds in the direction of decreasing j, by means of synthesis operators $\psi_j^{\downarrow} : V_{j+1} \rightarrow V_j$. Here, the upward arrow indicates that the operator $\psi^{\uparrow}$ maps a signal to a level higher in the pyramid, whereas the downward arrow indicates that $\psi^{\downarrow}$ maps a signal to a level lower in the pyramid. The analysis operator $\psi_j^{\uparrow}$ is designed to reduce information in order to simplify signal representation at level $j+1$, whereas the synthesis operator $\psi_j^{\downarrow}$ is designed to map this information back to level j.

The signal can be re-constructed from any level i in the pyramid to a higher level j by successively composing analysis operators. This gives an operator:

$$\psi_{i,j}^{\uparrow} = \psi_{j-1}^{\uparrow}\psi_{j-2}^{\uparrow}\cdots\psi_i^{\uparrow}, \quad j > i, \tag{2.6.1}$$

which maps an element in V_i to an element in V_j. On the other hand, the

composed synthesis operator:

$$\psi^{\downarrow}_{j,i} = \psi^{\downarrow}_{i}\psi^{\downarrow}_{i+1}\cdots\psi^{\downarrow}_{j-1}, \quad j > i, \tag{2.6.2}$$

takes us back from level j to level i. Finally, the composition:

$$\hat{\psi}_{i,j} = \psi^{\downarrow}_{j,i}\psi^{\uparrow}_{i,j}, \quad j > i, \tag{2.6.3}$$

a signal from level i to level j and back to level i again.

Since the analysis operators $\psi^{\uparrow}_{j}$ are designed to reduce signal information, they are not generally invertible, and information loss cannot be recovered by using only the synthesis operators $\psi^{\downarrow}_{j}$. Therefore, $\hat{\psi}_{i,j}$ can be regarded as an approximation operator that approximates a signal at level i, by mapping the reduced information at level j, back to level i.

The WT is recognised as a linear tool in its original form. However, the introduction of the lifting scheme has made it possible to be extended to non-linear system/non-linearity since it has provided a useful way to construct non-linear wavelets in the decomposition process. In [45], an adaptive lifting step using a non-linear selection criterion has been proposed by Claypoole *et al.* In [46], [47], [48], linear and non-linear lifting steps are combined based on a median operator and its applications in image compression and noise removal is also discussed.

As a non-linear branch of image and signal processing, MM may be used to construct a family of non-linear wavelets, called morphological wavelets. Its major difference from the classical linear wavelet is that the linear signal analysis filter in the morphological wavelet is replaced by the morphological operators, erosion and dilation. The framework and fundamental theories of morphological wavelets have been proposed by Heijmans in [49], which provides a set of fundamental theories for constructing morphological multi-resolution decomposition schemes.

The morphological Haar wavelet, both in one and two dimensions, is introduced as a simple example in [49]. Assume that there exists two subsets V_j and W_j. V_j refers to the signal at level j in the approximate space and

W_j refers to that in the detail space. The signal analysis operators and detail analysis operators are defined as $\psi_j^{\uparrow} : V_j \to V_{j+1}$ and $\omega_j^{\uparrow} : W_j \to W_{j+1}$. On the other hand, the signal synthesis proceeds by means of synthesis operators $\Psi_j^{\downarrow} = \psi^{\downarrow} \dot{+} \omega^{\downarrow} : V_{j+1} \times W_{j+1} \to V_j$. Given an input signal $x \in V_j$ and detail $y \in W_j$, the analysis and synthesis operators of the morphological Haar wavelet in one dimension are defined as:

$$\psi^{\uparrow}(x)(n) = x(2n) \wedge x(2n+1), \tag{2.6.4}$$

$$\omega^{\uparrow}(x)(n) = x(2n) - x(2n+1), \tag{2.6.5}$$

$$\psi^{\downarrow}(x)(2n) = \psi^{\downarrow}(2n+1) = x(n), \tag{2.6.6}$$

$$\omega^{\downarrow}(2n) = y(n) \vee 0, \tag{2.6.7}$$

$$\omega^{\downarrow}(y)(2n+1) = -(y(n) \wedge 0). \tag{2.6.8}$$

Here "$\wedge$" denotes minimum and "$\vee$" denotes maximum. Compared with the linear Haar wavelet decomposition scheme whose analysis filters are linear low-pass filters, the signal analysis filters in the morphological Haar case are non-linear and may do a better job at preserving the edge information for a image or signal.

2.7 The lifting scheme

Wavelets based on dilations and translations of a mother wavelet are referred to as the first generation wavelets or classical wavelets [50]. The lifting scheme provides a much more flexible method for constructing wavelets, which are named as the second generation wavelets. Unlike the classical ones, wavelets based on the lifting scheme are not necessarily translations and dilation of one function. Therefore, these wavelets can be used conveniently to define wavelet bases for bound intervals and irregular sample grids, solve equations, and analyse data on curves or surfaces. In addition, the classical wavelets can be implemented with the lifting scheme by factoring them into lifting steps.

2.7.1 Wavelets and the lifting scheme

Wavelets

The DWT represents a signal in terms of shifts and dilations of a low-pass scaling function $\varepsilon(t)$ and a bandpass wavelet function $\rho(t)$ [51]. The transform is multi-scale, which creates a set of coarse coefficients representing signal information at the lowest scale, and a set of detail coefficients with increasingly finer resolution. As shown in Fig. 2.2, the transform is typically implemented as a filter bank with analysis low-pass filter $H(z)$ and high-pass filter $G(z)$. $c[n]$ and $d[n]$ are the scaling and wavelet coefficients respectively.

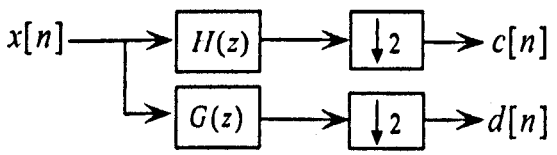

Figure 2.2: Filter bank implementation of the wavelet transform.

The inverse transform uses synthesis low-pass filters $\widetilde{H}(z)$ and high-pass filters $\widetilde{G}(z)$ as shown in Fig. 2.3. The underlying wavelets and scaling functions form a biorthogonal basis and provide perfect reconstruction with special choices of $H, G, \widetilde{H}, \widetilde{G}$. The transform is typically iterated on the output of the low-pass band $c[n]$ to create the series of detail coefficients at different scales.

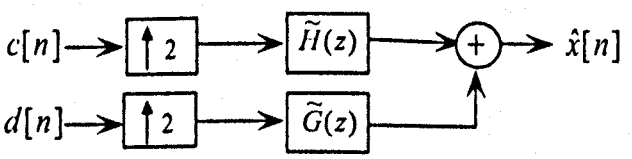

Figure 2.3: Filter bank implementation of the inverse wavelet transform.

The economy of the wavelet transform stems from the fact that DWT tends to compress real-world signals into just a few coefficients of large magnitude. The compression follows from the "vanishing moments" property of wavelets,

which guarantees that the wavelet coefficients of low-order polynomial signal are zero [51].

If a signal is exactly polynomial, it can be completely described using scaling coefficients. However, the signal is not polynomial in more realistic situations, yet can be well-approximated by a piecewise polynomial function. Because wavelet functions also have local support, most of the wavelet coefficients will be zero except those corresponding to wavelets having support near the break-points of the polynomial segments.

The DWT is fruitful to be viewed as a predication-error decomposition. The scaling coefficients at a given scale n are predictors for the data at the next high scale. The wavelet coefficients are simply the prediction errors between the scaling coefficients and higher resolution data that they attempt to predict. This interpretation has led a new framework for DWT design known as the lifting scheme.

The lifting scheme

Lifting is a spatial domain construction of biorthogonal wavelets, introduced by Sweldens [52]. Lifting can also be considered as an alternate implementation of classical wavelet transforms. The lifting scheme provides an entirely spatial-domain interpretation of the transform, as opposed to the traditional frequency-domain based constructions. The feature of local spatial interpretation enables us to adopt the transform to the data, thereby introducing non-linearities in the process of multi-scale transforms. Compared with Fourier transforms using the same filter all the time and wavelets being translation and dilation of one given function, lifting adapts local data irregularities in the transform process.

The basic idea behind the lifting scheme is very simple that the redundancy will be removed by using the correlation in the data. To reach this goal, the data are first split into two subsets, odd subset with the odd-indexed samples and even subset with the even-indexed ones which is called split stage. And then, the odd subset is predicted from the even subset, which is called predict

stage. At last, the prediction error, which is the difference between odd-indexed sample and its prediction, is used to update the even-indexed data. It is called the update stages. The block diagram of these three stage: split, predict and update, are illustrated in Fig. 2.4.

Split stage: Let $x[n]$ represent a discrete signal and split it into even and odd components $x_e[n]$ and $x_o[n]$ respectively, where

$$\begin{aligned} x_e[n] &= x[2n], \\ x_o[n] &= x[2n+1]. \end{aligned} \tag{2.7.1}$$

If the signal $x[n]$ corresponds to the sample of a smooth and slowly varying function, then the components of $x_e[n]$ and $x_o[n]$ are highly correlated. So it should be possible to accurately predict each odd polyphase coefficient from the nearby even polyphase coefficients.

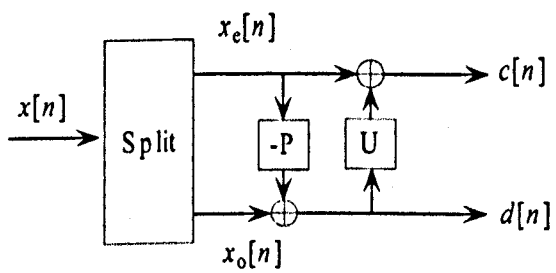

Figure 2.4: Typical lifting steps (analysis): Split, Predict (P) and Update (U). $c[n]$ and $d[n]$ are the scaling and wavelet coefficients, respectively.

Predict stage: In the interpolating formulation of lifting, the odd polyphase coefficients $x_o[n]$ can be predicted from the neighbouring even coefficients $x_e[n]$. Normally, the predictor for each $x_o[n]$ is a linear combination of neighbouring even coefficients:

$$P(x_e[n]) = \sum_l p_l x_e[n+l], \tag{2.7.2}$$

where the domain of l lies on how many even coefficients are using for the prediction. If N ($N = 2D$) coefficients are used in symmetry, then:

$$-D+1 \leq l \leq D. \tag{2.7.3}$$

A new representation of $x[n]$ may be obtained by replacing $x_o[n]$ with the prediction residual $d[n]$:

$$d[n] = x_o[n] - P(x_e[n]). \tag{2.7.4}$$

The prediction residual will be small if the underlying signal is locally smooth. Furthermore, the same information of the original signal $x[n]$ is preserved in the residual $d[n]$ since the odd polyphase coefficients $x_o[n]$ can be recovered by noting that:

$$x_o[n] = d[n] + P(x_e[n]). \tag{2.7.5}$$

Actually, the prediction procedure is equivalent to applying a high pass filter to the original signal $x[n]$.

Update stage: The last lifting step transforms the even polyphase coefficients $x_e[n]$ into a low pass filtered and sub-sampled version of $x[n]$ by updating $x_e[n]$ with a linear combination of the prediction residuals $d[n]$. $x_e[n]$ is replaced with:

$$c[n] = x_e[n] + U(d[n]), \tag{2.7.6}$$

and normally $U(d)$ is a linear combination of the values of d, denoted as:

$$U(d[n]) = \sum_l u_l d[n + l]. \tag{2.7.7}$$

No information is lost in the update step. Assuming the same U is chosen for synthesis, given $d[n]$ and $c[n]$, we have:

$$x_e[n] = c[n] - U(d[n]). \tag{2.7.8}$$

The inverse lifting stage is shown in Fig. 2.5. It corresponds to a critically sampled perfect reconstruction filter bank with c and d.

2.7.2 Example: linear prediction

From the second-generation viewpoint, one transform step of a discrete one-dimensional signal $x = \{x_k\}$ looks like:

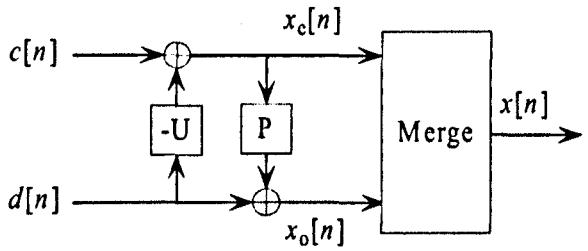

Figure 2.5: Typical inverse lifting steps (synthesis): Update (U), Predict (P) and Merge.

Splitting: Split the signal into even samples and odd samples:

$$c_i \leftarrow x_{2i},$$
$$d_i \leftarrow x_{2i+1}.$$

Prediction: Predict the odd samples using linear interpolation:

$$d_i \leftarrow d_i - \frac{1}{2}(c_i + c_{i+1}).$$

Update: Update the even samples to preserve the mean value of the samples:

$$c_i \leftarrow c_i + \frac{1}{4}(d_{i-1} + d_i).$$

As a result, the signal $c = \{c_k\}$ is a coarse representation of the original signal x, while the signal $d = \{d_k\}$ contains the high-frequency information that is lost when going from resolution level $j+1$ to resolution level j.

The same kind of interpolation scheme can be used to interpolate polynomials of higher degree. To the wavelets where the discrete data set are defined, these lifting schemes need some special care at the boundaries. In this way, a whole family of lifting schemes can be constructed as the above example.

Note that these lifting schemes are working on one-dimensional data. For two-dimensional data, such as image, it can be applied row and column separably, resulting a tensor product wavelet transform.

2.7.3 Boundary treatment

Real-world signals are limited in time and do not extend to infinity as shown in Fig. 2.6, however, the lifting scheme assumes that the signal is infinitely long. Thus, it is a problem to process the boundary of signals. One option is extending signals whit zeros, call zero padding. Nevertheless, the number of coefficients of the transformed signal will be obviously more than the original signal in this case. Furthermore, extending the signal with zeros can results in coefficients with large values as signals do not generally converge to zero towards the ends, which leads to significant coding inefficiencies. Truncating the number of coefficients to the number of samples of the original signal, or quantisation error of coefficients with large values will significantly distort the reconstructed signal.

Making the signal periodic is another option. As shown in Fig. 2.7, a finite signal as shown in Fig. 2.6 is extended by putting copies of itself in front of and behind the original signal. As the values at the left and right ends of the signal are not necessarily the same, as a result, discontinuity appear at the ends of the signal. A similar problem can arise as mentioned in zero padding.

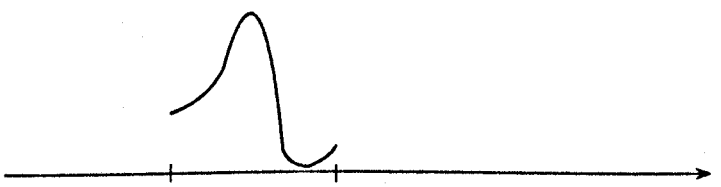

Figure 2.6: A finite signal.

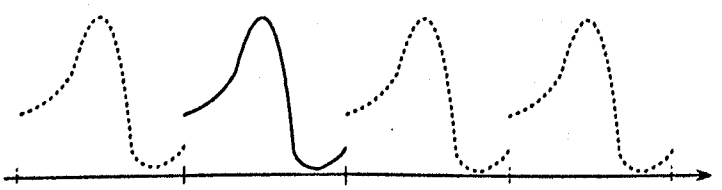

Figure 2.7: Periodic extension of a finite signal.

For symmetric lifting schemes or wavelets, extending the signal or image via

reflection is an effective strategy for handling boundaries. Figure 2.8 illustrates the symmetric extension of the finite signal in Fig. 2.6. Such an extension preserves continuity at the boundaries and usually leads to much smaller wavelet coefficients than if discontinuities were presented at the boundaries.

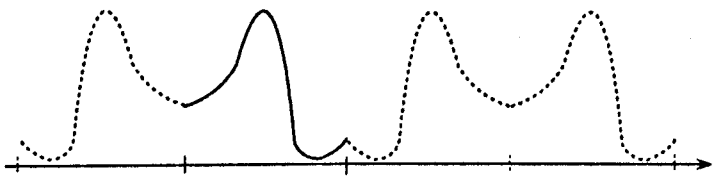

Figure 2.8: Symmetric extension of a finite signal.

2.7.4 Advantages of the lifting scheme

Compared with the classical filter bank algorithm, the lifting scheme has the following advantages:

- Lifting leads to a speedup, which is referred to as fast lifting wavelet transform when compared to the classic implementation.
- All operations within the lifting scheme are entirely done in parallel while only sequential part is the order of lifting operations.
- The lifting scheme allows a fully in-place calculation of the wavelet transform. No auxiliary memory is needed since it does not need other samples than the output of the previous lifting step. The value in original signal can be replaced with its transform.
- The inverse wavelet transform based on the lifting scheme is obtained immediately from the forward transform with only operations and toggle reversed.

2.8 Summary

The intention of this chapter is to present the fundamental concepts of MM. The basic operators involved in MM are defined. It has shown that there are only two basic operators: dilation and erosion, and the rest of the operations are obtained by proper combinations of them. More advanced morphological operators, including morphological gradient, top-hat transform, skeleton, are presented as well. Furthermore, the concepts of morphological filter, with recently developed morphological wavelets are introduced in this chapter.

In this chapter, the lifting scheme implementation of the wavelet transform is also briefly described. Three simple steps, namely split, predict and update, are used to calculate the wavelet coefficients. These three steps are also discussed to explain how the inverse transform can be easily calculated in a similar way. Furthermore, a summary of the advantages of the lifting scheme is given. Conclusively, the lifting scheme provides a simple and adaptive method of implementation of wavelet transform in comparison with the traditional filter bank.

Chapter 3

A Morphological Transform for Decaying DC Offset Removal

Transmission line networks frequently adopt digital distance protection relays. The input signals of the relays contain harmonics and exponentially decaying DC offset components when a fault has occurred. The decaying DC offset components in the signals cause fairly large errors in the Fourier transform, which may make the relays mal-operation. This chapter presents a novel application of an MM transform to extract the decaying DC offset components from fault currents or voltages. The performance of the Fourier transform is improved with this method, in the estimation of fundamental frequency components for digital protection relays.

3.1 Introduction

During the fault interval in digital distance protection of transmission lines, the input signals of relays contain large harmonics and exponentially decaying DC components. These DC components and the harmonics ought to be excluded and only the quantities of the fundamental frequency components should be retained in these signals. Hence, for the distance protection relays, it is necessary to identify the fundamental frequency components accurately.

The Fourier transform is one of the most popular algorithms used for a variety of measurements in protection systems. It can be used to extract the harmonic components accurately from the signals if the following assumptions are satisfied:

- The highest frequency of the input signal is less than $(N/2)f_1$, where N is the number of sampling points per fundamental frequency (f_1) cycle.
- There is no exponentially decaying DC component.

Practically, a well-designed low-pass filter can be used to meet the requirement of the first assumption; but for the second assumption, it is not likely to be satisfied in a fault condition. The exponentially decaying DC offset in some signals can introduce fairly large errors, as a result it can not be removed satisfactorily in the fault condition. The calculated amplitudes by the Fourier transform may deviate from the real values by more than 15% in the worst case. Such a large relative error highly reduces the accuracy of digital protection relays, therefore, the exponentially decaying DC components need to be removed as well as the harmonic components in the fault signals.

An algorithm using a full-cycle Discrete Fourier Transform (DFT) for one cycle plus two samples to calculate and compensate for the DC offset, is presented in [53]. The proposed algorithm demands complex calculations for DC offset removal. The data window and amount of calculations are of concern when the algorithm is used for real-time applications. In [54], the exponentially decaying DC component is taken into account without knowing its time constant. The first two terms of the Taylor series expansion are used to represent the decaying DC component, and the Least Squares Error (LSE) curve fitting technique is applied to estimate the fundamental and other harmonics. Other approaches such as a Kalman filter are also evaluated in [55]. However, most of these methods require prior knowledge of the system parameters for the estimation.

This chapter introduces the system characteristics when a fault occurs in a power system, followed by presenting the algorithms which are frequently

adopted by digital protection relays, including the Fourier transform. Aiming at reducing the estimation error of the Fourier transform, a method based on a morphological transform is presented to extract the decaying DC offset from the fault signals. Thanks to the above techniques, the estimation accuracy of the fundamental frequency component using DFT is greatly improved.

3.2 System fault characteristics

Fault currents in a power system depend on the impedance of the system between the generating sources and the fault location, the pre-fault current flowing in given line contributing to the total fault, and the point on the sinusoid voltage waveform at which the fault occurs. An ideal network is shown in Fig. 3.1 simulate the system with a fault occurring at a certain point.

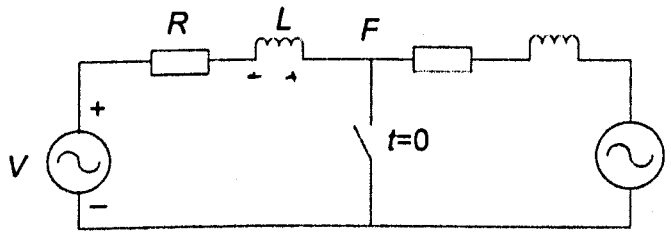

Figure 3.1: Ideal network for Fourier transform error estimation

The power system network is represented by the resistance R and the inductance L, which are Thevenin equivalent parameters [56] of the entire system to the left side of the fault point F. The differential equation of the circuit on the left side is presented as follows:

$$L\frac{di}{dt} + Ri = V_m \sin(\omega t + \beta), \tag{3.2.1}$$

where V_m is the maximum value of the sinusoidal source voltage and β represents the angle of the supply voltage at which the fault is applied. In the system, the shunt susceptances of the transmission line are neglected, which is an acceptable assumption in fault studies since the voltages are severely de-

pressed in the vicinity of the fault. This assumption needs to be checked when applied to high-voltage systems.

Solving the above equation for the fault current, the total fault current is obtained and divided into two components, a steady-state component i_s and a transient component i_t:

$$\begin{aligned} i(t) &= i_s(t) + i_t(t) \\ &= \tfrac{V_m}{Z}\sin(\omega t + \beta - \theta) + \left[\tfrac{V_m}{Z}\sin(\theta - \beta) + i(0^+)\right] e^{-Rt/L}. \end{aligned} \tag{3.2.2}$$

where $Z = \sqrt{R^2 + X^2}$, $X = \omega L$ and $\theta = \tan^{-1}\left(\frac{\omega L}{R}\right)$. The steady-state component, i_s, has the frequency of the applied voltage, but is shifted in phase by the angle β and the constant angle of the system impedance θ. The transient component, i_t, has two parts, one of which depends on the angle β on the voltage waveform when the fault is applied. In many cases this pre-fault load current is negligible compared with the large magnitudes of the transient fault current.

3.3 Digital protection relay algorithms

Digital relaying algorithms continuously process data representing samples taken from the measurement of instantaneous voltages and currents during normal operation. The algorithms can extract information from the measured values, such as amplitudes and phase angles using sequential samples. Faulted or other system conditions can be determined by comparing the measured values to pre-determined threshold. These algorithms have been widely developed and implemented in digital relays.

Mann and Morrison algorithm

The Mann and Morrison algorithm [57] only uses one sample and one derivative to calculate the amplitude and phase of the signal, which is based on the assumption that the voltage and current maintain sinusoidal form after the fault [58]. Therefore, the amplitude and phase of the voltage or current can be obtained from a limited number of samples.

If the samples are from a sinusoidal signal described by:

$$v(t) = V_1 \sin(\omega_0 t), \tag{3.3.1}$$

then, the derivation of the signal is:

$$v'(t) = \omega_0 V_1 \cos(\omega_0 t), \tag{3.3.2}$$

where $v'(t) = \mathrm{d}[v(t)]/\mathrm{d}t$. From the above equations, the peak value of the sinusoidal signal can be expressed as:

$$V_1 = \sqrt{v(t)^2 + \left(\frac{v'(t)}{\omega_0}\right)^2}. \tag{3.3.3}$$

The above equations are valid for any instant. The derivatives of the signal can be obtained from two consecutive samples if the signal is considered linear. The derivative can be estimated as the slope of the linear segment of the signal, which can be calculated by:

$$v'[k] = \frac{\Delta v}{\Delta t} = \frac{v[k+1] - v[k]}{\Delta t}, \tag{3.3.4}$$

where Δt is the time interval between two consecutive samples.

The amplitude and phase angle of the signal can therefore be calculated and updated after each new sample using the two equations as follows:

$$\begin{aligned} V[k] &= \sqrt{v[k]^2 + \left(\frac{v[k+1]-v[k]}{\omega_0 \Delta t}\right)^2}, \\ \phi[k] &= \tan^{-1}\left(\frac{v[k]\omega_0 \Delta t}{v[k+1]-v[k]}\right). \end{aligned} \tag{3.3.5}$$

A significant disadvantage of Mann and Morrison algorithm is that the length of the filter window is so short that missing or delayed samples would make the output of this algorithm unstable.

Rockefeller and Udren algorithm

The Rockefeller and Udren algorithm uses both of the first and second derivative, which is one sample longer than the previous Mann and Morrison algorithm. It can reduce errors due to the decaying DC component. Using the

same notations used in the Mann and Morrison algorithm, the first and second derivatives of the sinusoidal signal are expressed as:

$$v'[k] = \frac{v[k+1] - v[k-1]}{2\Delta t}, \tag{3.3.6}$$

$$v''[k] = \frac{v[k+1] - 2v[k] + v[k-1]}{(\Delta t)^2}. \tag{3.3.7}$$

The amplitude and phase angle of the sampled signal are:

$$V[k] = \frac{1}{\omega_0}\sqrt{(v'[k])^2 + \left(\frac{v''[k]}{\omega_0}\right)^2}, \tag{3.3.8}$$

and

$$\phi[k] = -\tan^{-1}\left(\frac{v''[k]}{\omega_0 v'[k]}\right). \tag{3.3.9}$$

Rockefeller and Udren algorithm utilises three data samples, so it has the same problems of delayed packets of data as Mann and Morrison algorithm. These algorithms are extremely sensitive to deviations of the apparent sampling rate. It is impossible to use these classical solutions for processing non-sequential samples, as it can be seen from the equations which only represent the amplitude and phase angle of the sampled signals. In order to accommodate for non-sequential and delayed samples, algorithms using large number of samples are required. In fact, the most stable and widely used algorithm in digital protection relays is the DFT [59][60].

Full-cycle Fourier transform

The full-cycle Fourier transform is the most widely used algorithm that can extract the amplitude and phase angle of a signal. It is immune to invariable DC components and can filter integral harmonics [61][62].

Any measured periodic voltage signal can be expanded into its Fourier series representation [63] as:

$$v(t) = a_0 + \sum_{n=1}^{\infty} a_n \cos(n\omega_0 t) + \sum_{n=1}^{\infty} b_n \sin(n\omega_0 t). \tag{3.3.10}$$

The values of the coefficients a_0, a_n and b_n can be obtained as:

$$a_0 = \frac{1}{T}\int_{t_0}^{t_0+T} v(t)dt, \tag{3.3.11}$$

$$a_n = \frac{2}{T}\int_{t_0}^{t_0+T} v(t)\cos(n\omega_0 t)dt, \quad n = 1, 2, \cdots \infty, \tag{3.3.12}$$

$$b_n = \frac{2}{T}\int_{t_0}^{t_0+T} v(t)\sin(n\omega_0 t)dt, \quad n = 1, 2, \cdots \infty, \tag{3.3.13}$$

where T is the period of the fundamental component of the signal. If the measured signal is considered to be represented as discrete, real numbers with N samples, the real and imaginary parts of the phasor representing the sampled signal are obtained as:

$$V_{Re}(k) = \frac{2}{N}\sum_{n=0}^{N-1} v[k-n]\cos(\frac{2\pi n}{N}), \tag{3.3.14}$$

$$V_{Im}(k) = \frac{2}{N}\sum_{n=0}^{N-1} v[k-n]\sin(\frac{2\pi n}{N}). \tag{3.3.15}$$

The amplitude and phase angle of the signal are obtained using the real and imaginary components respectively as:

$$V(k) = \sqrt{(V_{Re}(k))^2 + (V_{Im}(k))^2}, \tag{3.3.16}$$

$$\phi[k] = \arctan\left(\frac{V_{Im}(k)}{V_{Re}(k)}\right). \tag{3.3.17}$$

Half-cycle Fourier transform

To cut the response time of the algorithm in half, the samples during half cycle of the fundamental component are used. Hence, the coefficients of the series expansion can be obtained as:

$$a_0 = \frac{1}{T/2}\int_{t_0}^{t_0+T/2} v(t)dt, \tag{3.3.18}$$

$$a_n = \frac{2}{T/2}\int_{t_0}^{t_0+T/2} v(t)\cos(n\omega_0 t)dt, \quad n = 1, 2, \cdots \infty, \tag{3.3.19}$$

$$b_n = \frac{2}{T/2}\int_{t_0}^{t_0+T/2} v(t)\sin(n\omega_0 t)dt, \quad n = 1, 2, \cdots \infty, \tag{3.3.20}$$

where T is the period of the fundamental component of the signal. Using the same approach as for the full-cycle Fourier transform, the real and imaginary parts of the phasor representing the sampled signal are obtained as:

$$V_{Re}(k) = \frac{4}{N}\sum_{n=0}^{N/2-1} v[k-n]\cos(\frac{2\pi n}{N}), \tag{3.3.21}$$

$$V_{Im}(k) = \frac{4}{N}\sum_{n=0}^{N/2-1} v[k-n]\sin(\frac{2\pi n}{N}). \tag{3.3.22}$$

Similarly, the amplitude and phase angle of the signal can be obtained using the real and imaginary components. The disadvantage of the half-cycle Fourier transform is that it is not able to filter out DC component and even harmonics from the signal.

Least Square Error algorithm

The LSE digital relaying algorithm can be implemented for multiple variables, which was proposed by Sachdev and Baribeau [64]. If a sampled signal contains only odd harmonics, and a previous low-pass filter has been applied to eliminate the high-frequency components, with only a decaying DC component, fundamental and third harmonic left, the sampled signal can be expressed as:

$$v(t) = K_0 e^{-\frac{t}{\tau}} + K_1\sin(\omega_1 t + \theta_1) + K_3\sin(\omega_3 t + \theta_3), \tag{3.3.23}$$

where τ is the time constant describing the decaying exponential. With the first three elements of the Taylor series expansion of the DC component used, the previous equation can be rewritten as:

$$\begin{aligned} v(t) = &\ K_0 - K_0 t/\tau + K_0 t^2/2\tau^2 + K_1\sin(\omega_1 t + \theta_1) + K_3\sin(\omega_3 t + \theta_3) \\ = &\ K_0 - K_0 t/\tau + K_0 t^2/2\tau^2 + K_1\sin(\omega_1 t)\cos\theta_1 \\ &+ K_1\cos(\omega_1 t)\sin\theta_1 + K_3\sin(\omega_3 t)\cos\theta_3 \\ &+ K_3\cos(\omega_3 t)\sin\theta_3. \end{aligned} \tag{3.3.24}$$

The above equation is valid for any value of t. With the following notations:

$$\begin{aligned} V &= [\ v_{k1}\ \ v_{k2}\ \ v_{k3}\ \ v_{k4}\ \ v_{k5}\ \ v_{k6}\ \ v_{k7}\ ]^T \\ &= [\ 1\ \ \sin(\omega_1 t_k)\ \ \cos(\omega_1 t_k)\ \ \sin(\omega_3 t_k)\ \ \cos(\omega_3 t_k)\ \ t_k\ \ t_k^2\ ]^T. \end{aligned}$$

and

$$\begin{aligned} X &= [\ x_1\ \ x_2\ \ x_3\ \ x_4\ \ x_5\ \ x_6\ \ x_7\ ]^T \\ &= [\ K_0\ \ K_1\cos\theta_1\ \ K_1\sin\theta_1\ \ K_3\cos\theta_3\ \ K_3\sin\theta_3\ \ -K_0/\tau\ \ K_0/2\tau^2\ ]^T. \end{aligned}$$

Equation (3.3.24) can be written for consecutive values $t_1, t_2, \cdots, t_m$ as:

$$\begin{aligned} S &= [\ S_1\ \ S_2\ \ \cdots\ \ S_m\ ]^T \\ &= [\ \sum_{n=1}^{7} v_{1n}x_n\ \ \sum_{n=1}^{7} v_{2n}x_n\ \ \cdots\ \ \sum_{n=1}^{7} v_{mn}x_n\ ]^T. \end{aligned} \tag{3.3.25}$$

The values of x_j can be obtained using the pseudo-inverse of matrix $V = [v_{ij}]$, where $i = 1, 2, \cdots m$ and $j = 1, 2, \cdots 7$. The matrix of (3.3.25) can be written as:

$$S = VX, \tag{3.3.26}$$

where $X = [x_j]$, with $j = 1, 2, \cdots 7$. Subsequently,

$$\begin{aligned} &V^T S = V^T V X, \\ &(V^T V)^{-1} V^T S = (V^T V)^{-1} V^T V X. \end{aligned} \tag{3.3.27}$$

As a result:

$$X = (V^T V)^{-1} V^T S. \tag{3.3.28}$$

The amplitudes and phase angles of the fundamental and the third harmonic can be obtained from X.

3.4 Impact of DC offset on the Fourier transform

The Fourier transform is frequently employed in digital relays to estimate the fundamental complex phasor element and remove the DC component and

harmonics. However, a large decaying DC offset can cause the estimated magnitude of the Fourier transform to deviate from the real value. This error can be investigated from the ideal network shown in Fig. 3.1.

In this ideal network, the fault current $i(t)$ can be represented as:

$$i(t) = A_0 e^{-\frac{t}{\tau}} + A_1 \sin(\omega t + \beta - \theta), \tag{3.4.1}$$

where $\tau = \frac{L}{R}$, $A_0 = \frac{V_m}{Z}\sin(\theta - \beta) + i(0^+)$ and $A_1 = \frac{V_m}{Z}$. Uniformly sampling i_t every $\Delta T = 1/f$ under the frequency of f, a set of discrete values are obtained over a fundamental frequency cycle, which are represented as:

$$i_k = A_0 r^k + A_1 \sin(\frac{2\pi}{N}k + \beta - \theta) \quad k = 0, \cdots, N, \tag{3.4.2}$$

where $r = e^{-(\Delta T/\tau)}$, N is the number of sampling points per fundamental frequency cycle. Applying the Fourier transform to these discrete values, the fundamental frequency components $Z_{\text{real}}(k)$, $Z_{\text{imag}}(k)$ can be obtained as follows:

$$Z_{\text{real}}(k) = \frac{2}{N}\sum_{r=k-N+1}^{k} i(r)\cos(\frac{2r\pi}{N}), \tag{3.4.3}$$

$$Z_{\text{imag}}(k) = \frac{2}{N}\sum_{r=k-N+1}^{k} i(r)\sin(\frac{2r\pi}{N}), \tag{3.4.4}$$

and the fundamental frequency amplitude and phasor are calculated as:

$$A_k = \sqrt{Z_{\text{real}}(k)^2 + Z_{\text{imag}}(k)^2}, \tag{3.4.5}$$

$$\theta_k = \tan^{-1}\frac{Z_{\text{imag}}(k)}{Z_{\text{real}}(k)}. \tag{3.4.6}$$

Figure 3.2 is an example of using the Fourier transform to estimate the amplitudes of the fundamental frequency component for a fault current $i(t)$ in the ideal network shown in Fig. 3.1. The curve shown in Fig. 3.2 represents the estimated amplitudes of the fault current with a decaying DC offset included. From Fig. 3.2, it can be observed that the maximum and minimum values calculated during the first cycle of the fault current, may cause more than 15% relative error. Through the evaluation of the errors using the ideal network, a conclusion can be drawn that the presence of decaying DC offset

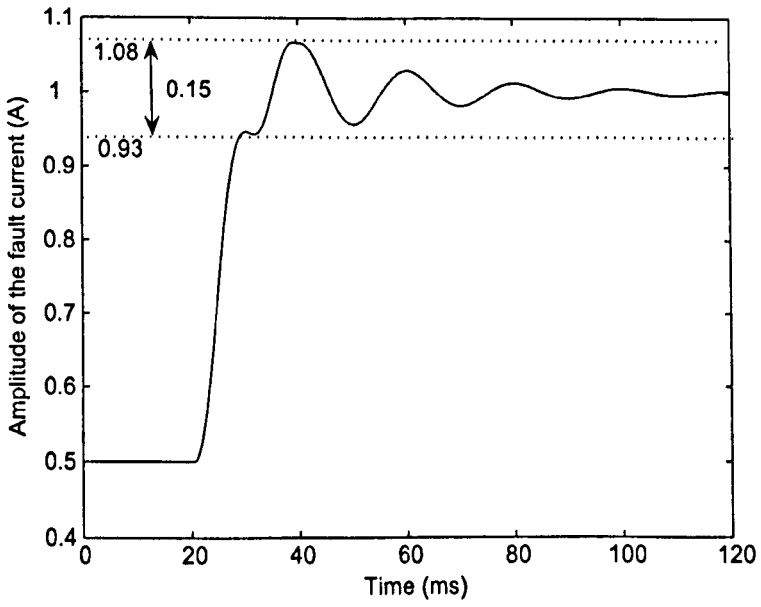

Figure 3.2: The fundamental amplitudes of the fault current $i(t)$ estimated by Fourier transform.

components has a drastic impact on the Fourier transform. Therefore, a correction measurement needs to be adopted to filter the exponentially decaying DC components.

3.5 A morphological transform for DC offset extraction

The transient fault current of relays is processed by the following morphological transform:

$$y = (a \circ b \bullet b + a \bullet b \circ b)/2, \tag{3.5.1}$$

where a is the input current signal, b is the SE and y is the output result. A flat SE with its origin at the centre is taken. Its length should be a half of the duration of the power system fundamental waveform, either 10 ms or 1/120 s, to extract the 50/60 Hz fundamental frequency component and its higher harmonics from the input signal, leaving only the DC offset component in the

output signal, y, the dotted line, as illustrated in Fig. 3.3.

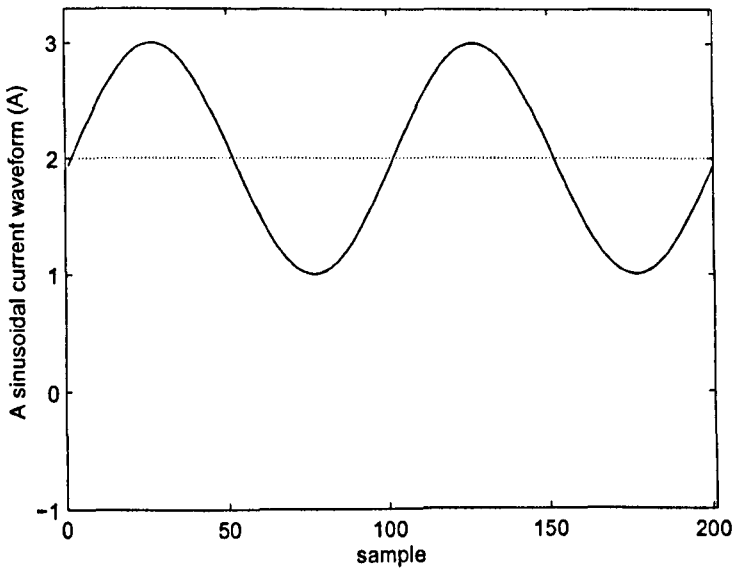

Figure 3.3: A morphological transform for the extraction of DC offset (dotted line) in a sinusoid (solid line).

Furthermore, the samples within a quarter cycle of the waveform are able to be used to extract the DC components in half a cycle, since another quarter cycle of waveform can be symmetrically simulated. In this chapter, the length of a cycle represents the duration of each fundamental frequency cycle. So an SE half a cycle long is applied to extract the DC offset in each quarter cycle of the input signal. The detailed procedure is illustrated in Fig. 3.4.

The proposed method can be used to extract the DC offset along the time axis. The DC offset component in fault current $i(t)$ is presented as the straight lines in Fig. 3.5. Figure 3.6 is a comparison of the real decaying DC offset waveform with the extracted results.

A series of straight lines are extracted by the morphological transform as discussed in the previous section. Moreover, the straight lines can be used to calculate the real values of the exponentially decaying DC component.

A linear segment with a slope is treated as an approximation of the exponentially decaying DC component in each half cycle. The mathematical

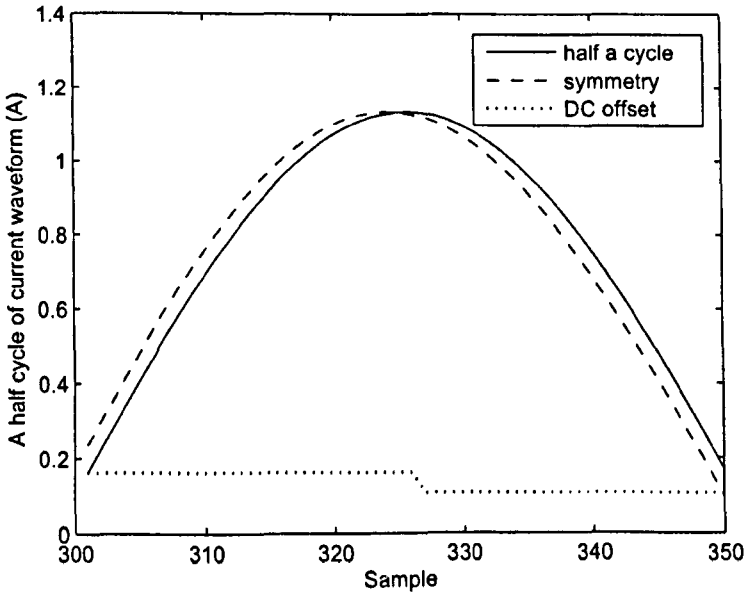

Figure 3.4: The extraction of the DC offset from a half cycle of waveform and its symmetry.

expression of the linear segment is determined by the first order Taylor-series expansion at $(T_1/2)$ over the interval $[0, T_1]$, which is represented as:

$$\begin{aligned} A_0 e^{-\frac{t}{\tau}} &\cong C_0 + C_1(t - \tfrac{T_1}{2}) \\ &= B_0 + B_1 t. \end{aligned} \tag{3.5.2}$$

Here T_1 represents the time interval of a fundamental cycle of the signal.

Let K_1, K_2 denote the values of two samples estimated by the morphological transform as shown in Fig. 3.4. Apply the two samples to the equation of the linear segment and get:

$$\begin{aligned} K_1 &= B_0 + B_1 t, \\ K_2 &= B_0 + B_1(t + \tfrac{N}{2}\Delta t), \end{aligned} \tag{3.5.3}$$

where N is the number of sampling points per fundamental frequency cycle and $\Delta t = T_1/N$ is a time interval between two consecutive samples. So B_0 and B_1 can be calculated with the values of K_1 and K_2.

The derivatives of the exponentially decaying DC offset for both sides of

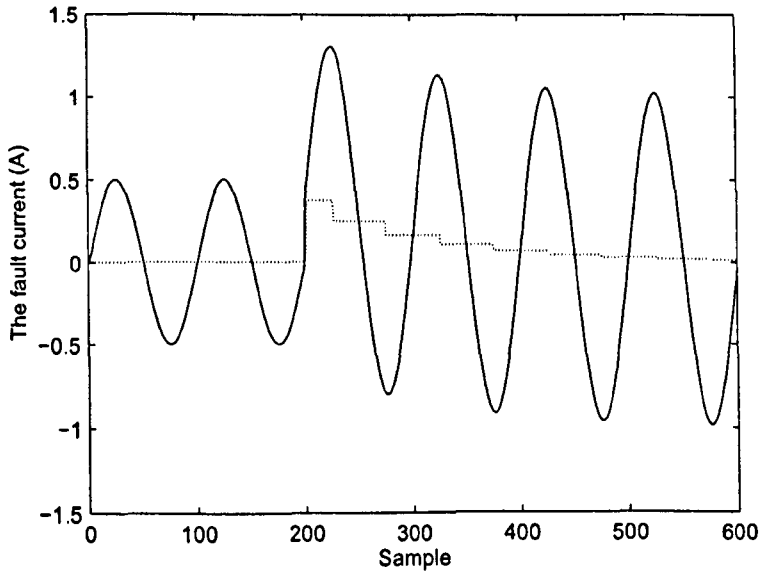

Figure 3.5: The DC offset (dotted line) extracted from the fault current (solid line) using the morphological transform.

the equation (3.5.2) are represented as:

$$\begin{aligned}(A_0 e^{-\frac{t}{\tau}})' &= -\tfrac{A_0}{\tau} e^{-\frac{t}{\tau}}, \\ (B_0 + B_1 t)' &= B_1,\end{aligned} \tag{3.5.4}$$

So B_1 equals to the slope of the decaying DC offset $-\frac{A_0}{\tau}e^{-\frac{t}{\tau}}$ approximately when $t = 0$. That is:

$$B_1 = -\frac{A_0}{\tau} e^{-\frac{0}{\tau}} = -\frac{A_0}{\tau} \tag{3.5.5}$$

Let B_2 denote the slope of the linear segment to approximate the following half cycle of DC offset. Its value amounts to the slope of the DC offset at $t = T_2/2$, which is:

$$B_2 = -\frac{A_0}{\tau} e^{-\frac{T_2/2}{\tau}} = B_1 \cdot e^{-\frac{T_2/2}{\tau}}. \tag{3.5.6}$$

Since

$$K_2 = K_1 \cdot e^{-\frac{T_2/2}{\tau}}, \tag{3.5.7}$$

B_2 can be calculated as:

$$B_2 = \frac{K_2 B_1}{K_1}. \tag{3.5.8}$$

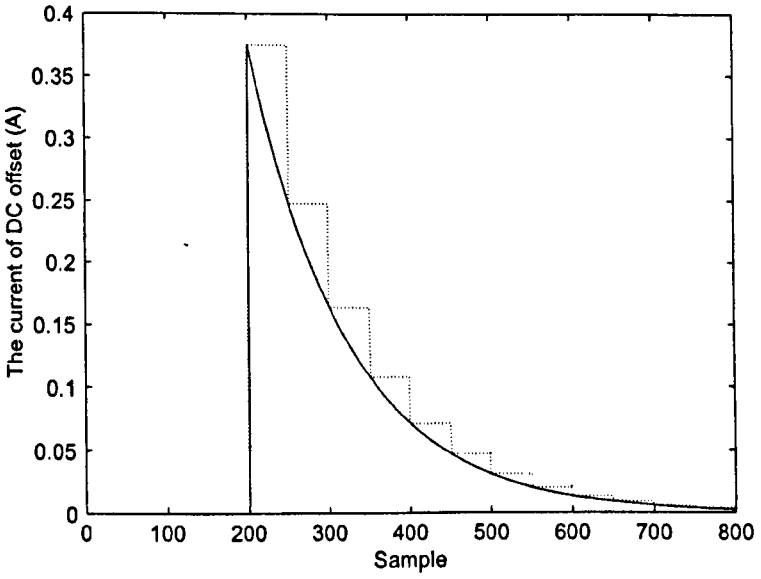

Figure 3.6: The extracted DC offset (dotted line) and real exponentially decaying DC offset (solid line) in simulation.

Therefore, each point of the DC offset for the following half cycle can be estimated with the values of B_2 and K_2. A whole cycle of the exponentially decaying DC offset can be estimated accurately. The estimation result of the DC offset is shown in Fig. 3.7.

With the exponentially decaying DC offset subtracted from the input current, the estimation results of the fundamental frequency amplitudes by the Fourier transform are presented as the solid line in Fig. 3.8. The dotted line denotes the estimated amplitudes of the fundamental frequency component of the input current without extracting the DC offset.

The ideal network can be re-used here to evaluate the effectiveness of the proposed method using the Fourier transform under different sampling rates. The most commonly used sampling rates in digital relays are investigated and the evaluation results are listed in Table 3.1, where FOU stands for the Fourier transform without DC offsets extracted, and MM for the results with the application of the proposed method. $Am_{\max}$ and $Am_{\min}$ denote the maximum and minimum magnitudes of the results.

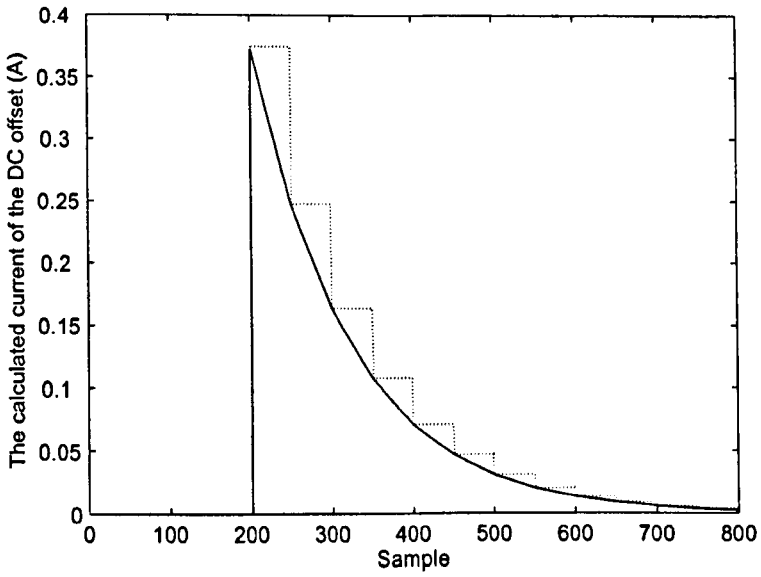

Figure 3.7: The calculated DC offset (solid line) based on the extracted result (dotted line) with the morphological transform.

From the simulation results shown in Table 3.1, it can be observed that the peak value changes a little for different sampling rates. For each sampling rate, the proposed method narrows the amplitude deviation. It reduces the overshoot of the maximum peak from 1.0664 to 1.0001; and for the minimum, it descends from 0.9563 to 0.9997. Other simulations are carried out by changing the angle of the supply voltage in Fig. 3.1, which is denoted as β in (3.2.1). The position where the peak occurs changes with different β, while the variation

Table 3.1: Peak values under different sampling rates

Sampling rate	FOU		MM	
N	$Am_{\max}$	$Am_{\min}$	$Am_{\max}$	$Am_{\min}$
12	1.0612	0.9563	1.0031	0.9839
24	1.0650	0.9568	1.0011	0.9985
36	1.0659	0.9571	1.0005	0.9994
48	1.0661	0.9573	1.0004	0.9996
100	1.0664	0.9577	1.0001	0.9997

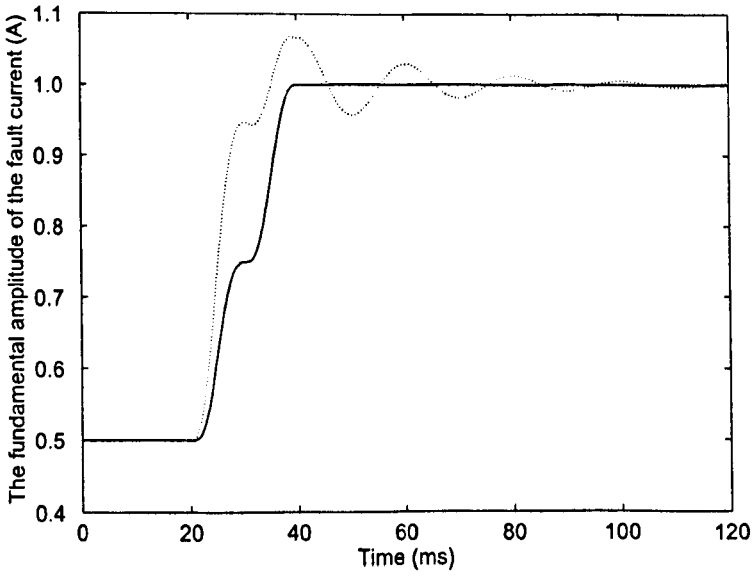

Figure 3.8: The fundamental amplitude estimated by the Fourier transform with (solid line) and without (dotted line) the extraction of the DC offset .

of the peak value itself is very small. Hence, the similar results are obtained using the proposed method and the details are not listed here.

3.6 Summary

The current and voltage signals contain large harmonics and exponentially decaying DC offset components during a fault period. The Fourier transform is normally used as a low-pass filter to filter high order harmonics. However, it is unable to extract the exponentially decaying DC components of transient post-fault signals accurately using a short sampling window.

In this chapter, a new method based on a morphological transform is proposed to eliminate the influence of the decaying DC offset on the Fourier transform. The method performance evaluation based on the current signals from the idea network demonstrated the method can extract the exponentially decaying DC offset components from fault signals and improve the performance of the Fourier transform.

Chapter 4

A Morphological Scheme for Fast Identification of Transformer Inrush Currents

This chapter presents a novel morphological scheme for distinguishing between magnetic inrush and internal fault currents for power transformer differential protection. This scheme is based on the synthesis and analysis operators of MM used for multi-resolution decomposition of signals. It is employed to extract the features of current accurately within a much shorter sampling window than that of the conventional methods. Simulation studies have been undertaken to evaluate the scheme based on an Alternative Transients Program (ATP) transformer model operating under different conditions of a three-phase high voltage power transformer. The simulation results show that the proposed scheme is able to identify the inrush current accurately within 10 ms, a half cycle of the fundamental waveform. With the scheme proposed, the replaying time of the transformer protection relay is reduced.

4.1 Introduction

Power transformers are a class of very expensive and important components in electric power systems [65]. Design of relays for power transformer protection has been a challenging problem for many years. Traditionally, a differential protection relay is always selected as the primary protection of most power transformers [66][67]. In a differential protection relay, differential currents can provide quite significant information about the nature of the current flowing through power transformer windings. Such information may include frequency contents, transient nature, periodicity, non-periodicity and frequency-time relations. There are many factors that should be considered when attempting to design differential protection for power transformers such as magnetising inrush current, over-excitation and CT saturation.

The main challenge in power transformer protection is to avoid false trip action under the magnetising inrush current, *i.e.* the ability of the relaying algorithm to distinguish different magnetising inrush currents from internal faults, external faults and normal currents [68]. Inrush current is frequently encountered when the transformer is energised. While a transformer is connected to a power source, the inrush current may reach 10 to 20 times of the transformer's rated value, which is as high as that of internal fault currents. Therefore, it is difficult to distinguish between the inrush and internal fault currents, which may make conventional differential relays take a trip action. Such a malfunction will affect both the reliability and stability of the whole power system.

To avoid the unnecessary trip caused by inrush currents, accurate identification of inrush currents has been investigated for a long time. The methods are based on identifying the second harmonic component which are commonly used for blocking differential relays since the inrush currents normally contain a large second harmonic [69][70]. However, the second harmonic of an inrush current is significantly decreased when the core steel of modern power transformers has been improved [71]. Moreover, the second harmonic component may also be produced by internal faults of the power transformer due to the

presence of a shunt capacitor or the distributive capacitance in a long extra high voltage transmission line which is connected to the transformer [72]. Consequently, the techniques based on second harmonic identifications will not be sufficiently effective when they are used in differential protection relays, as they cannot accurately identify transformer inrush, using the content of the second harmonic component. Furthermore, the second harmonic based methods slow down the operating speed of the transformer relays, since a wide sample window is required for calculating the second harmonic component using a Fourier transform technique. To improve the accuracy and speed of the transformer protection relays, an alternative way for inrush identification.

The methods based on the direct detection of the distortion of waveform shapes have been investigated for find the difference between the internal fault and inrush currents. A major group of these methods are based on the identification of the differential current peaks. If successive peaks of the differential current fail to occur over a period of 7.5 $\sim$ 10 ms, the relay operation will be blocked [73]. Recognising the length of the time interval between the zero-crossing points of the differential current has been considered as another well-known principle for distinguishing between the internal fault and inrush currents [74, 75, 76]. For inrush currents, the relay will be blocked if the time interval, during which the amplitude of the current is close to zero, is longer than a threshold. However, for inrush currents, the interval may decrease due to CT saturation. Recently, a novel blocking scheme called waveform correlation has been proposed in [77]. It compares the symmetry between the first half-cycle and the second half-cycle of the waveform using a complete fundamental cycle of sampling data. In this method, internal fault and inrush currents can be distinguished if the correlation coefficient between the two groups of data obtained from the first half-cycle and second half-cycle respectively is over a given threshold. However, using this method, it is still difficult to identify the inrush currents which are symmetric. Moreover, a whole cycle of data is required for correlation calculation. Recently, several alternative algorithms have been developed. In [78] and [79], an artificial neural network has been trained to

distinguish between inrush and internal fault currents. A fuzzy logic method was suggested to develop differential protective relays [80]. Moreover, some algorithms based on Wavelet analysis were reported in [81] and [82]. Most of these approaches are still liable to cause the malfunction of the relay in the case that inrush current has a low second harmonic component and internal fault current has a high second harmonic component. In addition, the Wavelet method involves complicated calculation.

A method based on MM was proposed to identify inrush currents in [83]. This method is simple and effective, but needs a sampling window more than a complete fundamental cycle. In this chapter, an alternative fast approach based on morphological decomposition is proposed for distinguishing between the internal fault and inrush currents within a sampling window of 10 ms, which is half a fundamental cycle. The morphological operations decompose a current into a series of components, the features of which are extracted for inrush current detection. The proposed scheme is evaluated by using a simulated transformer model and experimental data. The presented simulation and experiment results clearly show that the morphological scheme can accurately and promptly distinguish between the internal fault and inrush currents for power transformers.

4.2 Inrush transients

The magnetising inrush current can not be easily predicted, thus the characteristics of this type of current are very complex and difficult to analyse. It depends on many factors such as the instant of connecting the supply to the power transformer, the residual flux, the type of winding connection, the core type material and the type of relation between current and voltage [84][85].

When a transformer is first energised, there is a transient inrush current establishing the magnetic field of the transformer. Considering a transformer that is energised from a sinusoidal busbar voltage, the steady-state flux is the

integral of the voltage shown as follows:

$$\Phi = \frac{1}{N}\int \sin\omega t dt = \frac{-1}{\omega N}\cos\omega t, \tag{4.2.1}$$

where N is the number of turns of the winding. The instantaneous magnitude of the core flux at the instant of energisation is the residual flux Φ_r. The amount of offset of the sinusoidal flux generated by the voltage is dependent upon the point of the voltage wave where the transformer is energised. Assuming the peak magnitude of the normal core flux is labelled as Φ_m, the peak core flux can therefore reach $2\Phi_m + \Phi_r$, which will drive the core into saturation. The worst case is that the transformer is energised at zero point of the voltage wave with a residual flux of Φ_m. In this case the saturation will be even greater and a significant inrush current will be excited.

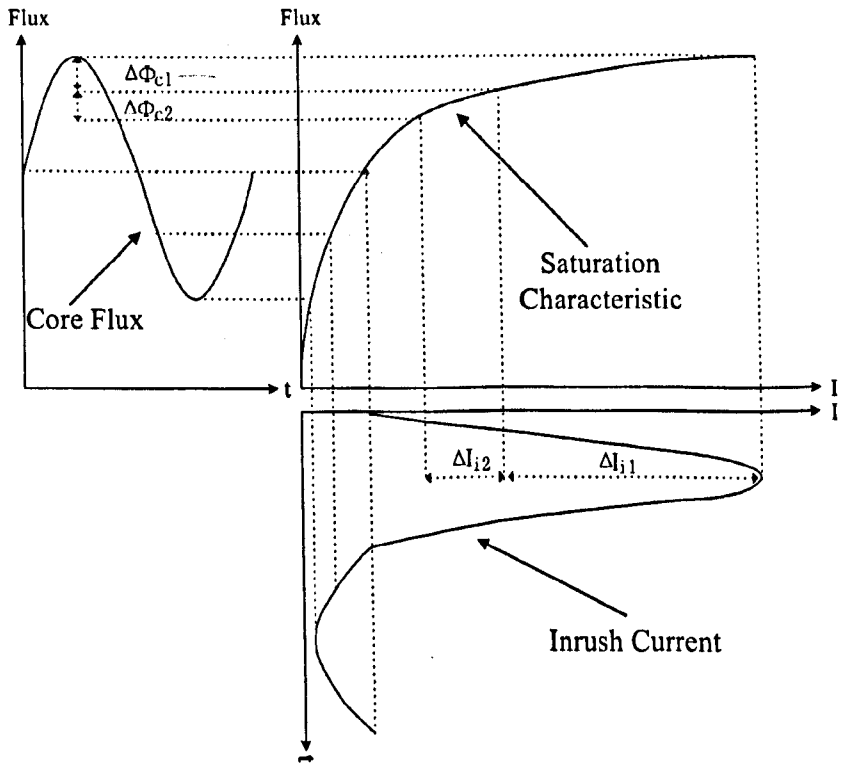

Figure 4.1: Derivation of the inrush current wave from the saturation curve.

The occurrence of inrush is illustrated in Fig. 4.1. For each point on the flux wave at the top left of Fig. 4.1, a corresponding point can be found on the

saturation curve, at the top right, plotted against the current, in time evolution, as shown in the lower part of the figure. Fig. 4.1 illustrates the operation of mapping the magnetic flux onto the inrush current via the saturation curve in a full cycle of the current. It can be clearly seen that the inrush waveform is not a sinusoidal wave, since the saturation curve is not a linear line. The first half cycle of the inrush current looks like a bell, with a peak occurring at the maximum flux, and is not symmetrical to the second half of the cycle. In contrast to a sinusoidal wave, the inrush current is distorted by the magnetic saturation. Also shown in Fig. 4.1, two equal increments of flux in a sinusoid wave, $\Delta\Phi_{c1}$ and $\Delta\Phi_{c2}$, produce dramatically different increments of inrush current, ΔI_{i1} and ΔI_{i2} respectively. It should be noted that there is a significant difference between the inrush and normal currents, in particular in the features of their changes in slop and symmetries. These features may be extracted by our methodology presented in the following section.

4.3 A morphology decomposition scheme for inrush identification

Morphological decomposition filters [86][87] can be used to separate signal into various levels in detail. In this section, a multi-resolution morphological filter is constructed to decompose the signal I of a transformer current. Let V_j represent the signal space and W_j the detail space at level j respectively. We can define $\psi_j^{\uparrow}$: $V_j \rightarrow V_{j+1}$ as the signal analysis operator and $\omega_j^{\uparrow}$: $W_j \rightarrow W_{j+1}$ as the detail analysis operator. The synthesis operator $\Psi_j^{\downarrow}$ maps the information of the signal at level j back to a lower level. These operations can be constructed by a specifically designed sequence of fundamental morphological operators, dilation and erosion. Here, the analysis and synthesis operators are defined as:

$$\begin{aligned} \psi_j^{\uparrow}(r_j) &= r_{j+1} = \gamma(r_j), \\ \omega_j^{\uparrow}(r_j) &= s_{j+1} = r_j - r_{j+1}, \\ \Psi_j^{\downarrow}(\psi_j^{\uparrow}(r_j), \omega_j^{\uparrow}(r_j)) &= r_j = r_{j+1} + s_{j+1}, \end{aligned} \tag{4.3.1}$$

where $r_1 = I$, $s_1 = \varnothing$ and $j = 1, 2, \cdots$. Let $\gamma(r_j) = (r_j \ominus g_j) \oplus g_j$, where $\ominus$ and $\oplus$ denote the morphological erosion and dilation respectively and g_j is the SE at level j of decomposition. The signal I is decomposed as a set of components s_j $(j = 2, 3, \cdots)$, and can be reconstructed by $I = \sum_j s_j$. With such a scheme, the waveform of the signal I is decomposed into a collection of segments which reflect the shape information of the signal.

To perform the decomposition of current I with N samples per fundamental cycle, the current waveform is transformed to obtain two signals, I' and its mirror signal I'', by adding up a predetermined constant which makes the input signals I' and I'' calculable by the morphological operators, e.g., $I' \geq 0$ and $I'' \geq 0$. I' denotes the half-cycles which contain peaks, while I'' represents the half-cycles with valleys. The SE g_j is a simple zero-valued flat line with a length of l_j. Assuming f_r represents the system sampling frequency, then $l_j = j/f_r$ $(j = 1, 2, \cdots, \frac{N}{4})$. The decomposition process starts at the peak point of a complete signal in half a cycle, with a length of SE, $l_2 = 2$. Two more points are included at level j in comparison with that at level $j-1$. The highest level for the decomposition is one fourth of the sample points, N, in each fundamental cycle. Based on the decomposition using (4.3.1) under g_j, a set of peak values, I_j, the magnitudes of the components s_j extracted from the current I' and I'' in half a cycle at different levels. I' and I'' are obtained during a fundamental cycle, which are indicated in Fig. 4.2, where I' and its mirror signal I'' are illustrated and a constant of 2 kA is added to make $I' \geq 0$ and $I'' \geq 0$. Assuming the current is sampled with 12 points per cycle, 3 pairs of samples can be used to gain the peak values with 3 levels of decomposition. I_1, I_2 and I_3 are attained from the current I', at the peak in the first half-cycle. For the second half-cycle containing a valley, another group of values, I_1, I_2 and I_3, are obtained from I'' respectively.

A feature criterion σ_j can be employed to quantify the feature of the current waveform, based on the extracted values, I_j, in comparison with value estimated from a standard sinusoidal wave, as follows:

$$\sigma_j = \frac{I_j}{\cos((j-1) * \varphi) - \cos(j * \varphi)}, \qquad (4.3.2)$$

where $j = 1, 2, \cdots, \frac{N}{4}$, $\varphi = f_s * 2\pi / f_r$ and f_s is the system frequency, equalling to 50 Hz. For each half-cycle data of the current updated, a new group of values of σ_j can be obtained and regrouped as a time series, σ_t.

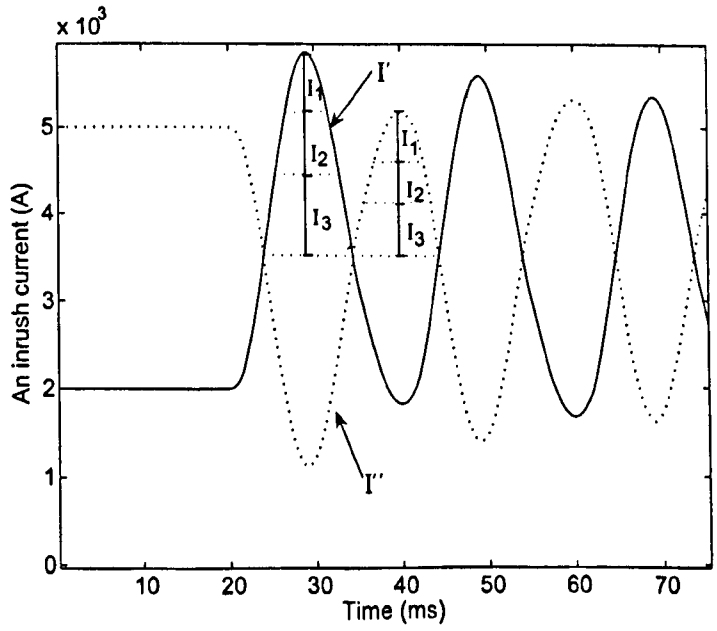

Figure 4.2: The morphological decomposition of a current waveform.

According to the characteristics of inrush current, σ_t reflects the slopes of the saturation curve and is variable from time to time. While for internal fault currents, σ_t, remains the same all the time. This difference can be utilised to distinguish between the internal fault and inrush currents.

4.4 Transformer model

The transformer simulation model is the one supplied by the BCTRAN, an auxiliary routine of the ATP simulation software. It calculates two matrices $[R]$ and $[L]$ modelling the transformer based on positive and zero sequences excitation and short-circuit tests [88][89]. For a three-phase transformer with two windings as shown in Fig. 4.3, the transformer can be described with two

6×6 matrices, $[R]_{6\times6}$ and $[L]_{6\times6}$ as follows:

$$R = \begin{bmatrix} R_1 & 0 & 0 & 0 & 0 & 0 \\ 0 & R_2 & 0 & 0 & 0 & 0 \\ 0 & 0 & R_3 & 0 & 0 & 0 \\ 0 & 0 & 0 & R_4 & 0 & 0 \\ 0 & 0 & 0 & 0 & R_5 & 0 \\ 0 & 0 & 0 & 0 & 0 & R_6 \end{bmatrix}, \tag{4.4.1}$$

$$L = \begin{bmatrix} L_1 & M_{12} & M_{13} & M_{14} & M_{15} & M_{16} \\ M_{21} & L_2 & M_{23} & M_{24} & M_{25} & M_{26} \\ M_{31} & M_{32} & L_3 & M_{34} & M_{35} & M_{36} \\ M_{41} & M_{42} & M_{43} & L_4 & M_{45} & M_{46} \\ M_{51} & M_{52} & M_{53} & M_{54} & L_5 & M_{56} \\ M_{61} & M_{62} & M_{63} & M_{64} & M_{65} & L_6 \end{bmatrix}, \tag{4.4.2}$$

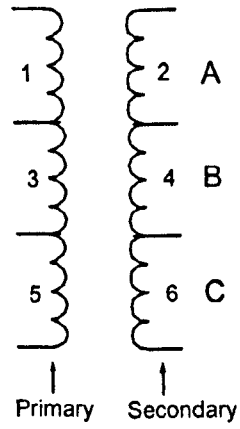

Figure 4.3: A three-phase transformer model with two windings

To model the case of a turn-to-earth fault, the corresponding faulty winding is divided into two sub-coils as shown in Fig. 4.4. In this situation, the transformer can be described with two modified 7×7 matrices $[R]_{7\times7}$, $[L]_{7\times7}$.

In a turn-to-turn case, the faulty coil is divided into three segments as shown in Fig. 4.5, thus the matrices $[R]_{8\times8}$ and $[L]_{8\times8}$ are used to simulate the fault.

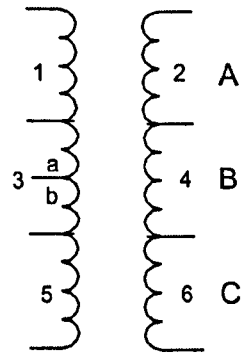

Figure 4.4: The diagram for the study of a turn-to-earth fault

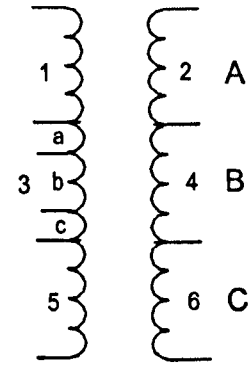

Figure 4.5: The diagram for the study of a turn-to-turn fault

Figure 4.6 shows a transformer connected to a power source. The characteristics and parameters of the transformer model are listed in Table 4.1. The sampling rate of the simulated system is 2.4 kHz at 50 Hz fundamental frequency.

4.5 Simulation results

Various cases of internal fault and inrush currents are simulated in this section. For the former, the terminal and internal winding faults are both taken into consideration. For the latter, the inrush currents are simulated with different energising angles and different remnant fluxes in the core of the transformer. The transformer is energised from the high-voltage side and there

Table 4.1: The parameters of the simulated transformer model

Transformer connection	Y_o/Δ (HV/LV)
Rated apparent power	750 MVA
Short-circuit power	4600 MVA
Rated ration	420 kV/27 kV
Iron core	Type-96
Saturation flux density	$B_s = 1.15B_m$
Source impedance	$Z = 0.01 + 0.06j\ \Omega$

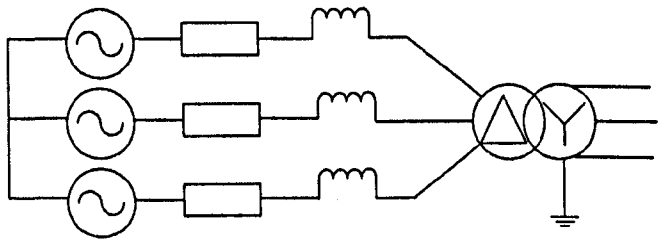

Figure 4.6: Transformer model

is a circuit breaker on the low-voltage side.

An extreme condition is given for generating inrush currents, the residual fluxes of which are $B_{ra} = 0.9B_m$, $B_{rb} = B_{rc} = -0.9B_m$ and the inception angle for phase A voltage source is 30°. The inrush currents are shown in Fig. 4.7. In such a test, the ratio of the second harmonic to the primary current component in the inrush current is less than 15%, and the minimum phase is 8%. In this case, it will cause a malfunction of the relay if a threshold of the second harmonic restraint is set to be 15% or above.

The feature criterion, σ_j, in (4.3.2), is calculated and arranged to σ_t. The phase B current, i_b, is selected for decomposition, since it has the smallest second harmonic ratio, 8%. For the convenience of comparison, σ_t is normalised by σ_t/σ_1, where σ_1 is the first value calculated at the beginning of the cycle. Because the sampling rate of the current is 48 points per cycle, the number of values of σ_t in one cycle is halved, e.g., 24 points in each cycle.

Figure 4.8 graphically illustrates the values σ_t of the inrush current i_b. The

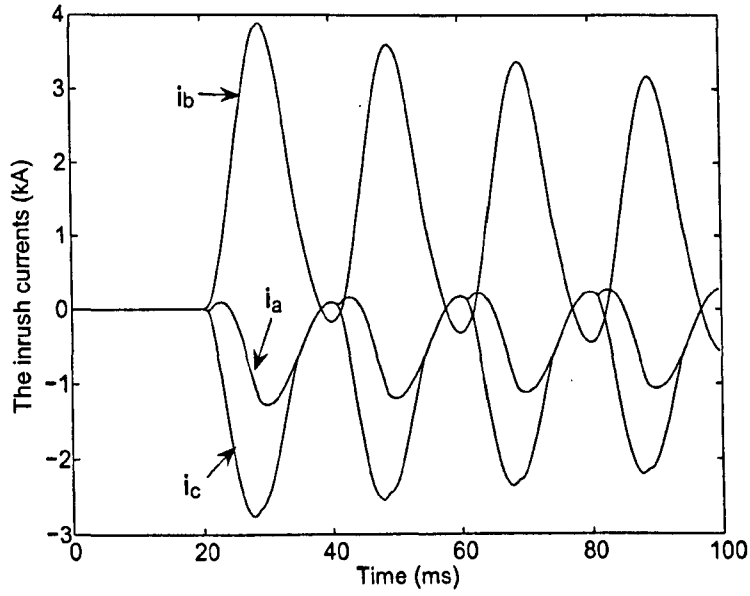

Figure 4.7: Three phase inrush currents

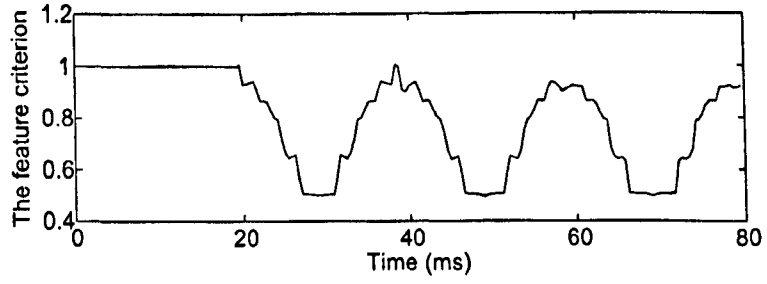

Figure 4.8: The value σ_t for the inrush current i_b

value of σ_t decreases in the first half-cycle and then increases in the second half-cycle. In the second cycle, this pattern repeats, which indicates the characteristic of a saturation curve. From the results, it can be seen that the developed scheme can accurately identify the feature of the inrush current in Fig. 4.7. The capture of this feature can be used to generate a blocking trip signal to the relay after the occurrence of the inrush current in no more than 10 ms. Other simulation cases are considered with different residual fluxes and inception angles, higher the second harmonic contents found in the inrush currents, larger variations of σ_t obtained. Therefore, the results of σ_t show a

similar pattern.

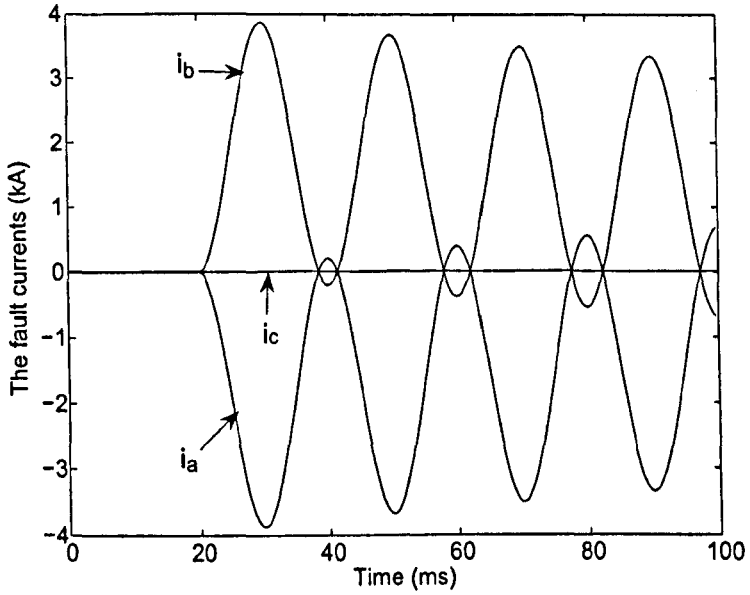

Figure 4.9: Three phase internal fault currents

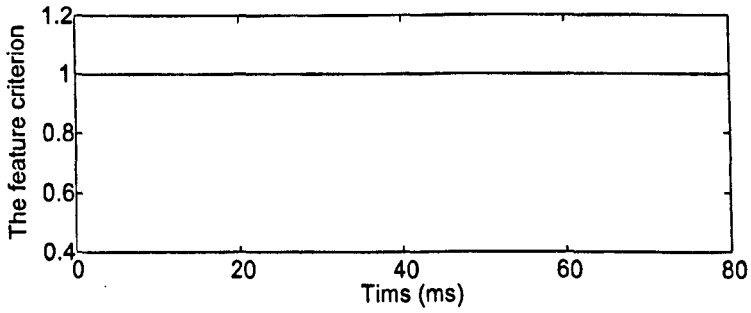

Figure 4.10: The value σ_t for the internal fault current i_b

Figure 4.9 shows the three phase currents generated by a terminal double phase fault at the high voltage winding. It is difficult to distinguish between the fault current in Fig. 4.9 and the inrush current of Fig. 4.7 by comparing the shapes directly. However, the difference may be easily identified by the proposed scheme. The fault current i_b in Fig. 4.9 is decomposed using the same scheme and the values of σ_t are calculated and shown in Fig. 4.10. In

this case, the value of σ_t almost remains the same as a straight line. Based on the values of σ_t, the fault current may be identified and a trip signal may be issued. More simulation studies for different fault types and locations are carried out to testify the validity the proposed scheme. The values of σ_t are not smaller than 0.65 even for the case when the fault current has the highest second harmonic content. Hence, an optimum threshold of σ_t is set at 0.5.

The proposed scheme has been evaluated on the internal fault and inrush currents obtained from a laboratory power transformer connected to a power source respectively. Figure 4.11 shows the current waveforms sampled from the laboratory transformer and the results obtained using the developed scheme. The scheme is only employed when a large differential current is detected by comparing the current samples at two sides of the transformer.

In Fig. 4.11, the value of σ_t for inrush current is significantly different from that of the internal fault. For the inrush current beginning at $t = 100$ ms, the minimum of σ_t during the first half-cycle is 0.08. If the threshold of σ_t, σ_{set}, is set at 0.5 (the optimum threshold based on simulations) as a criterion for the transformer relay, the inrush current can be identified easily when $\sigma_t < \sigma_{\text{set}}$. For the fault current, since the value of σ_t is larger than σ_{set} during the whole period of the first half-cycle, it can be used as a criterion for issuing a trip signal after the first half-cycle.

4.6 Summary

A novel fast scheme for transformer inrush current identification has been presented in this chapter. The proposed scheme is based on extracting the features of the current using the morphological synthesis and analysis operators. The scheme is able to decompose the observed current into a group of peaks and valleys which explore the features of the current in detail. The simulation studies have been undertaken, based on a typical high voltage power transformer connected to a power source, to verify the effectiveness of the proposed scheme. The simulation results show that the proposed scheme works satis-

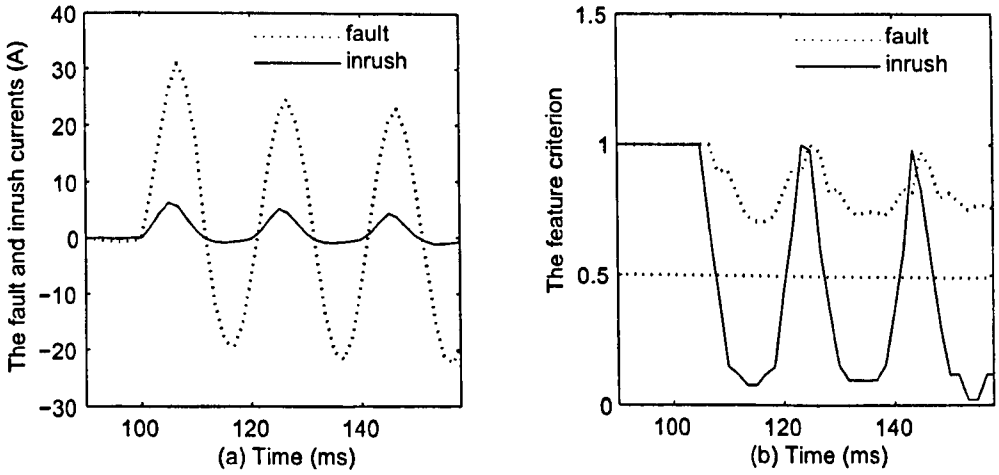

Figure 4.11: a) Sampled waveforms of internal fault (dashed line) and inrush current (solid line); b) The values of σ_t for the internal fault (dashed line) and inrush current (solid line).

factorily to distinguish between the internal fault and inrush currents. The scheme can be used to improve the performance of differential protection relays for power transformers. Further research will be conducted to validate its reliability.

Chapter 5

A Morphological Lifting Scheme for Current Transformer Saturation Detection and Compensation

CT saturation can cause protection relay mal-operation or even prevent tripping. The wave shape of the secondary current is severely distorted as the CT is forced into deep saturation when the residual flux in the core adds to the flux change caused by faults. In this chapter, a Morphological Lifting Scheme (MLS) is proposed to extract features contained in the waveform of the signal. The detection of the CT saturation is accurately achieved and the points of the inflection, where the saturation begins and ends, are found by the scheme used. This chapter also presents a compensation algorithm, based upon the detection results, to reconstruct healthy secondary currents. The proposed MLS and compensation algorithm are demonstrated on a sample power system. The simulation results clearly indicate that they can successfully detect and compensate the distorted secondary current of a saturated CT with residual flux.

5.1 Introduction

CT are widely used for both measurement and protection purposes in electrical power systems. Distorted secondary currents, due to CT saturation, can cause measurement error and protection relay malfunction [90]. Thus, the CT saturation problem has to be considered when designing a protection relay is designed.

Some methods for detecting CT saturation onset have been suggested in [91, 92, 93]. These methods only successfully detect the saturation based on some given assumptions such as the current collapses to zero as soon as the CT saturates and the residual flux at the beginning of the calculation is zero. These assumptions make the methods' applicability limited since they are not always satisfied in real systems.

An impedance-based CT saturation detection scheme for bus-bar differential protection is proposed in [94]. It uses the first-order differential equation of a secondary current, at the relay position, to detect the beginning and end points of inflection during CT saturation. As the value of the first-order differential at the instant next to the first point of inflection beginning is not large enough, another saturation detection algorithm is proposed, using the 3rd-order differential of the secondary current [95]. However, compared with the methods which only require the knowledge of the first-order differential, it needs a longer calculation time to get more distinct results, and suffers more from signal disturbances.

The approach of reducing the impact of CT saturation is to reconstruct the secondary current waveform, using a compensation algorithm. For the purpose of reconstruction, a function with given CT parameters was applied to approximately represent the non-linear core characteristics of a specific model of CT [92]. Another method, using an ANN [96], attempts to learn the non-linear characteristics of CT magnetisation and restructure the waveform based on the learned characteristics. However, due to the variations of CT saturation characteristics and secondary burdens, these methods cannot be universally applied in various situations.

In order to tackle the problem of CT saturation, advanced signal processing techniques are sought to deal with the shapes of the signals. The wavelet transform has been recognised as a powerful tool for analysing the transient shape distortion, but it can not be adaptively and universally applied to different situations since it is linear in its original form. The linear limitation makes it unable to deal with the CT saturation detection since it is difficult to distinguish the beginning and end points of inflection during CT saturation from the disturbances of noise. The emergence of lifting scheme [52] has made non-linear extensions of the wavelet transform possible since it provided a useful way to construct non-linear wavelets in the decomposition process. In [45], an adaptive lifting step using a non-linear selection criterion has been proposed by Claypoole *et al.* In three other references [46], [47], [48], they combined linear and non-linear lifting steps (based on a median operator), and discussed its applications in image compression and noise removal. As a non-linear branch of image and signal processing, MM may be used to construct a family of non-linear wavelets, called morphological wavelets. Its major difference with the classical linear wavelet is the linear signal analysis filter in lifting scheme is replaced by the morphological operators.

A new method of MLS, based on the morphological wavelets, is proposed in this chapter as a powerful analysis tool to detect CT saturation, and then a compensation algorithm is developed to reconstruct the distorted secondary current. The proposed scheme is a signal decomposition method based on the shape of the secondary current waveform. The method has the ability to extract important features from the distorted signal when CT saturation occurs, and it does not require any presetting parameters. Based on the detection of CT saturation characteristics, a real-time compensation of the distorted secondary current can be achieved.

In this chapter, the CT characteristics and saturation detection and compensation are addressed in Section 5.2. An MLS for CT saturation detection and a compensation algorithm, based upon the detection results, are expatiated in detail in Section 5.3 and 5.4 respectively. Their performance, tested

under various faults and CT conditions, is analysed based on a simple power system model in Section 5.5. Finally, summaries are drawn in Section 5.6.

5.2 The characteristics of current transformer

The AC-type protection relays are actuated by current and voltage supplied by current and voltage transformers. These transformers provide insulation against the high voltage of the power circuit, and also supply the relays with quantities proportional to those of the power circuit. The proper application of current and voltage transformers involves the consideration of several requirements such as mechanical construction, type of insulation, ratio in terms of primary and secondary currents or voltages.

Types of CTs

All types of CTs are used for relaying protection purposes. The iron core toroidal CT is usually chosen for relaying in higher-voltage circuits. The type of CT consists only of an annular-shaped core with a secondary winding. It is built into equipment such as circuit breakers, power transformers, generators or switch-gear. The core is arranged to encircle an insulating bushing through which a power conductor passes.

Calculation of CT accuracy

For relaying purpose, it is necessary to determine the phase-angle error of a CT. The load on the secondary of a CT is generally of such highly lagging power factor that the secondary current is practically in phase with the exciting current. Hence, the effect of the exciting current on the phase-angle accuracy is negligible. Furthermore, most relaying applications can tolerate a phase-angle error for metering purpose. If the ration error is tolerable, the phase-angle error can be neglected.

CT burden

The external load applied to the secondary current of a CT is called the "burden". The burden is expressed preferably in terms of the impedance of the load and its resistance and reactance components. The term "burden" is applied not only to the total external load connected to the terminals of a CT but also the elements of the load. The publications of manufacturers give the burdens of individual relays, from which the total CT burden can be calculated together with the resistance of interconnecting leads. The CT burden impedance decreases as the secondary current increases, because of saturation in the magnetic circuits of relays and other devices.

CT saturation

The iron core toroidal CT is widely used throughout the electrical power industry for the measurement of current. This kind of CT is not a linear transducer because of the iron core. Different levels of saturation occur in almost all CTs depending on the magnitude of the fault current being measured.

Figure 5.1 shows a simplified equivalent circuit of a CT for transient analysis. Z_m is the excitation impedance, R_2 and L_2 are the secondary inductance and resistance respectively. Normally, the value of Z_m is very large when the iron core runs at a low magnetic density, so the secondary current I_2 can be perfectly transformed from the primary current I_1.

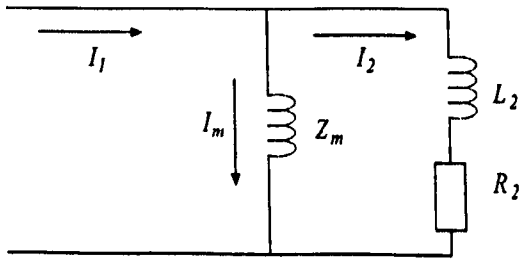

Figure 5.1: Simplified equivalent circuit of a CT for transient analysis.

When a system fault occurs, the fault current through the primary circuit of a CT can be considered as the superimposition of a sinusoidal component

and an exponential component, given by:

$$i_1(t) = Ae^{-\alpha t} + B\sin\phi_t, \tag{5.2.1}$$

where A, B, α and ϕ_t are the initial values of the exponential component, amplitude of the sinusoidal component, decaying coefficient, and a fault inception angle, respectively.

With a large exponential component added to the primary current, the magnetic density is promptly boosted to saturation which will cause Z_m to descend, thus the magnetising current I_m through the iron core will increase and distort the secondary current I_2. When the system runs under heavy saturation, Z_m is almost zero and all the current flows through the excitation coil, which makes the secondary current I_2 decrease to almost zero. This will lead to the gross measurement errors or malfunctions in relay tripping.

An important factor that affects CT saturation is the CT core. Increasing the size of CT core or using a core material that supports large flux densities can avoid CT saturation. But both options can affect the cost of transformer applications. A practical method used to correct CT saturation needs to be implemented in the existing device without adding the cost. To this end, an MLS for CT saturation detection and a compensation algorithm are investigated to deal with the CT saturation problem which influences seriously the operation of various protection relays in power systems. Figure 5.2 is a block diagram showing how the scheme and algorithm can be implemented for real-time detection and compensation of CT saturation. The secondary current I_2, transformed from the primary current I_1 by a CT, is sampled into a discrete-time sequence of values, $i_2(t)$, by a data-acquisition module. If a sample of $i_2(t)$ is determined within a saturation portion of the fault current waveform by the CT saturation detection scheme, a compensated sample will be generated by a compensation algorithm. Finally, the compensated currents are supplied to protection relays.

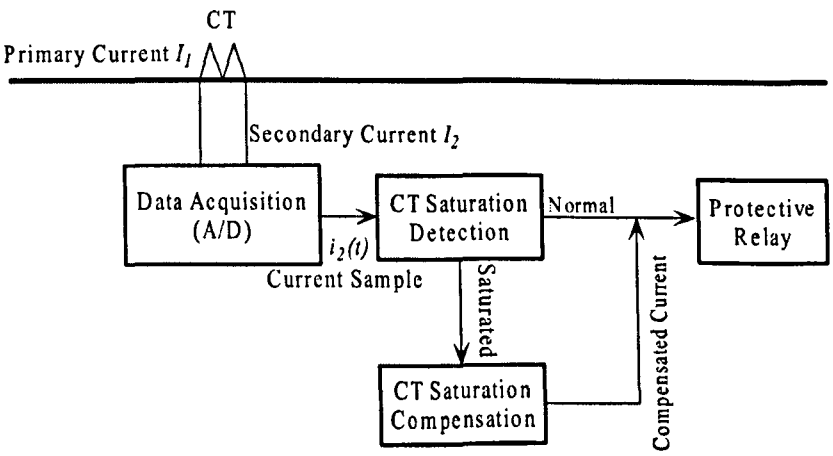

Figure 5.2: Real-time detection and compensation of CT saturation.

5.3 Current transformer saturation detection scheme

In order to make a new morphological scheme applicable in the detection of CT saturation in power systems, new morphological operators need to be introduced. Since the basic power system signals are composed of sinusoids, a symmetric SE, k_m, with the characteristics of a sinusoid can be employed as:

$$k_m = [\cos(2m+1)\varphi, \cdots \cos\varphi, \cos\varphi, \cdots \cos(2m+1)\varphi], \tag{5.3.1}$$

where $\varphi = 2\pi ft$; f is the power system frequency and t is the sampling time interval of the system. The total length of k_m is $2m$, where m is a positive integer.

According to the designed SE, a new type of erosion and dilation are defined as:

$$(x \oplus k_m)(n) = \max_{n-v\in D_x, v\in D_k} \{x(n-v)/k_m(v)\}, \tag{5.3.2}$$

$$(x \ominus k_m)(n) = \min_{n+v\in D_x, v\in D_k} \{x(n+v)/k_m(v)\}, \tag{5.3.3}$$

where x is the signal to be processed and D_x and D_k denote the domains of x and k_m respectively.

In the lifting scheme, the original data stream of signal $x(n)$ is split into two data streams: $x_e[n]$ and $x_o[n]$. Therefore, the detail signal d is obtained as the prediction residue lifted by:

$$d[n] = x_o[n] - P(x_e[n]), \tag{5.3.4}$$

where P represents the morphological prediction operator here, which is the mean of dilation and erosion results using different SEs with different lengths. It is defined as:

$$P(x_e) = \frac{1}{2l}\sum_{i=1}^{l}(x_e \oplus k_i + x_e \ominus k_i), \tag{5.3.5}$$

where k_i is an SE with a length of $2i$ $(i = 1, 2, \cdots, l)$ as defined in (5.3.1). When $i = l$, there are total $2l$ even samples (x_e) used in prediction, with l samples at left and l at right. If only one pair of even samples on the left and right are used, the prediction is denoted as:

$$P(x_e) = \frac{1}{2}(x_e \oplus k_1 + x_e \ominus k_1), \tag{5.3.6}$$

where $k_1 = [\cos\varphi,\ \cos\varphi]$. This MLS is highly adaptive for the sinusoidal signal compared with the classic morphological operators or the classic wavelet transforms. If the original signal x_n is a pure sinusoid in fundamental frequency, the detail signal d should always have a zero output since the steady component of the original signal is eliminated and the high-frequency components are left only in prediction residuals.

Since the current abruptly changes when CT saturation sets in, the MLS can successfully detect the saturation period based on the distorted secondary current. In a non-saturation period, the detail signal should have an output value near to zero, however, it stays at a large value whilst the CT is in saturation.

5.4 Current transformer compensating algorithm

The distorted secondary current can be compensated based on the detection of the CT saturation period. As shown in Fig. 5.1, the relationship between the secondary current $i_2(t)$ and the core flux $\lambda(t)$ of CT can be expressed as follows:

$$\frac{d\lambda(t)}{dt} = Ri_2(t). \tag{5.4.1}$$

Let t_0 represent the starting time of saturation, therefore the integration of λ from t_0 to t is:

$$\lambda(t) - \lambda(t_0) = R\int_{t_0}^{t} i_2(t)dt. \tag{5.4.2}$$

The core flux $\lambda(t)$ is determined by the magnetisation current $i_m(t)$ according to the magnetising curve. For the purpose of simplification, the saturated section of the magnetising curve is regarded as a straight line with a slope of K. The unit of K is H/S^{-1}. Hence the magnetising current can be obtained as:

$$K(i_m(t) - i_m(t_0)) = R\int_{t_0}^{t} i_2(t)dt. \tag{5.4.3}$$

Since the value of $i_m(t)$ at time t_0 is near to zero, $i_m(t)$ is calculated as:

$$i_m(t_0 + n\cdot\Delta t) = \frac{R}{K}\sum_{j=0}^{n} i_2(t_0 + j\cdot\Delta t), \tag{5.4.4}$$

where Δt represents the time interval between two samples and n is the n^{th} sample counting from time t_0. In (5.4.4), the value of $\frac{R}{K}$ can be deduced by a linear interpolation for the first point of the magnetising current $i_m(t_0 + \Delta t)$:

$$\begin{aligned} i_m(t_0 + \Delta t) = \; & [i_2(t_0) + (i_2(t_0) - i_2(t_0 - \Delta t))] \\ & -i_2(t_0 + \Delta t); \end{aligned} \tag{5.4.5}$$

$$\frac{R}{K} = i_m(t_0 + \Delta t)/(i_2(t_0) + i_2(t_0 + \Delta t)). \tag{5.4.6}$$

Then the secondary current referred as to the distorted current, $i_2'(t)$, is reconstructed by summing the measured secondary current $i_2(t)$ with the estimated

magnetising current $i_m(t)$ point by point. The compensation process is illustrated in Fig. 5.3.

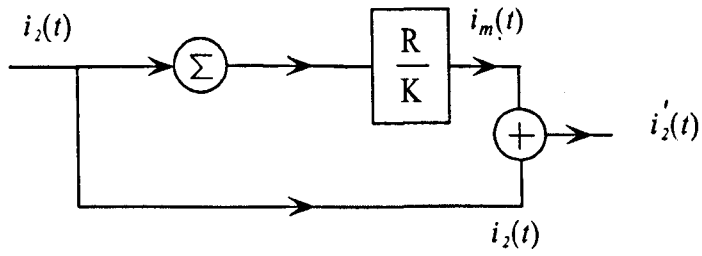

Figure 5.3: The compensation process.

5.5 Case studies

A sample power system is considered to demonstrate the effectiveness of the proposed MLS for CT saturation detection and the compensation algorithm. It consists of two sources and a single line as shown in Fig. 5.4. S1 and S2 are equivalent sources, with Z_{S1} and Z_{S2} as their equivalent impedances, respectively. The phase-to-phase voltage of the sources is 120 kV RMS and the system frequency is 50 Hz. The total length of the transmission line is 200 km. The CT saturation is simulated when a fault occurs near the CT location with a sampling frequency of 5 kHz.

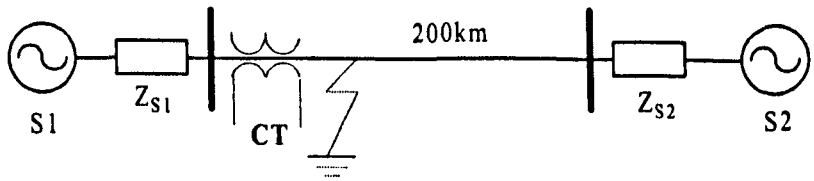

Figure 5.4: Model of the sample power system.

A CT model of a saturable transformer component was employed for case studies. The 2000:5 tap was selected from a C400 class CT which is the CT used in this simulation study. The magnetising branch is represented internally as a

non-linear inductor. Since the residual flux in the core needs to be considered, the Type-96 inductor was employed for its ease of initialising the residual flux in the CT core. To use the model, the CT hysteresis characteristics should be evaluated in advance. The saturation knee point is set at 10 p.u. (per unit) flux. Different faults were simulated in the study by changing the residual flux from -80% to 80% of the flux at the saturation point.

In the following discussion, the secondary current is firstly processed using the MLS and then reconstructed by the compensation algorithm. An SE, k_2, with a length of 4, *e.g.*, a moving window of 7 samples was used in the computation process. The proposed scheme and algorithm were tested for a variety of cases. The cases presented cover a wide range of fault conditions, including the changes of residual flux, fault inception angle and fault types. Despite the wide variety of cases, the simulation results clearly indicate that all distorted sections of the secondary currents are satisfactorily detected and then reconstructed using the proposed method.

5.5.1 -80% residual flux

Figure 5.5 shows the detecting result in the case of a remanence of -80% flux in the CT core. The polarity of the remanence is opposite to that of the DC offset, which results in a slight distortion beginning at the second cycle of the fault secondary current, as shown in Fig. 5.5. From Fig. 5.5 to Fig. 5.8, dotted and solid lines represent the primary and distorted secondary current respectively.

The detail signal d is extracted by the proposed scheme as shown in Fig. 5.5(b). It is composed of six periods of the wave with a similar pattern. The absolute values in these periods are much larger than zero, which indicates the CT runs in a saturated state. Figure 5.5(c) is the output of the detector in a binary mode, where '1' means the CT is saturated, while '0' represents an unsaturated state. The detection results clearly show that the proposed MLS successfully detects the interval of the saturation.

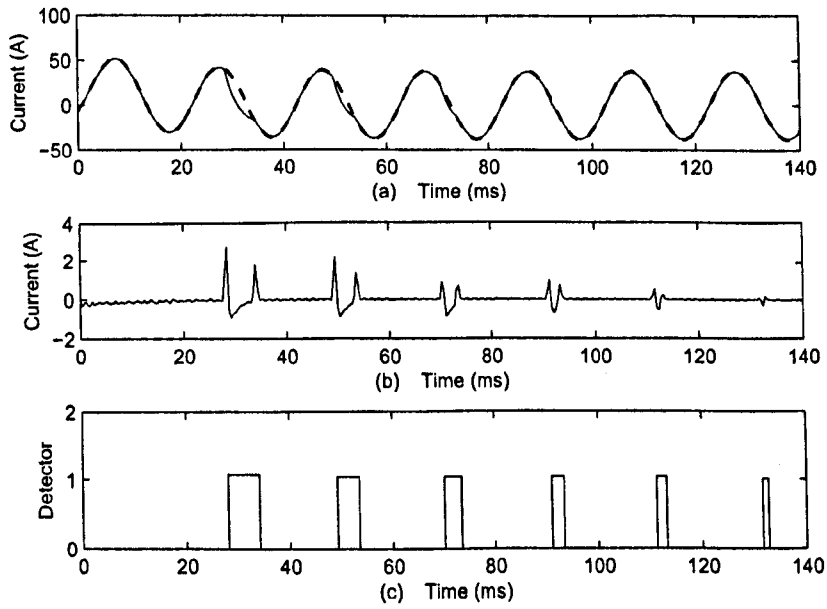

Figure 5.5: The case of an -80% residual flux with a single phase-ground fault; (a) the primary (dashed line) and distorted secondary current (solid line); (b) the detail signal d extracted from the secondary current; (c) saturation detection output.

5.5.2 0% residual flux

The extent of the distortion gradually becomes more severe as the remanence increases from a negative value to a positive value. The case shown in Fig. 5.6 has 0% remanence within the CT core. The distortion of the secondary current starts at the first cycle after the fault occurs.

Figure 5.6(c) clearly shows that the proposed MLS accurately detects the distorted sections of the original secondary current waveform.

5.5.3 80% residual flux

Figure 5.7 illustrates the distortion associated with 80% residual flux which is the maximum flux possible from a practical CT. Under this situation, the transit flux has a very short effective excursion before saturation occurs. It is apparent from the figure that the distortion of the secondary current is the severest in comparison with other situations. It begins only a few milliseconds

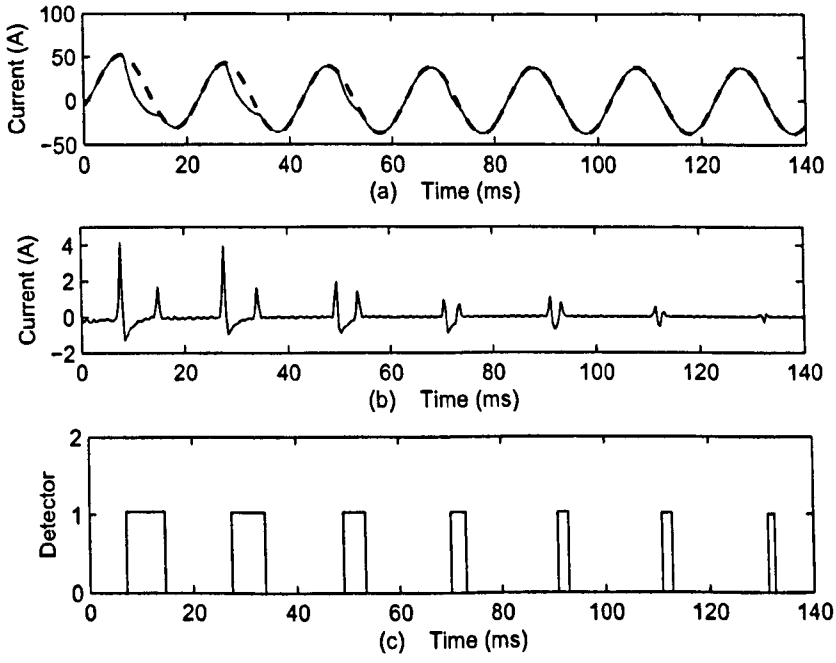

Figure 5.6: The case of a 0% residual flux with a single phase-ground fault; (a) the primary (dashed line) and distorted secondary current (solid line); (b) the detail signal d extracted from the secondary current; (c) saturation detection output.

a fault occurs.

The results indicate that the proposed MLS detects the interval of saturation even when the secondary current is severely distorted due to a high residual flux.

5.5.4 80% residual flux with an opposite fault inception angle

The orientation of the distortion will change if the fault inception angle is adjusted to make the fault current contain a negative DC offset. The secondary current will have upward distortion as shown in Fig. 5.8(a). Consequently, compared with the previous cases, the detail signal obtained has similar shapes with a different polarity. The CT saturation interval is also

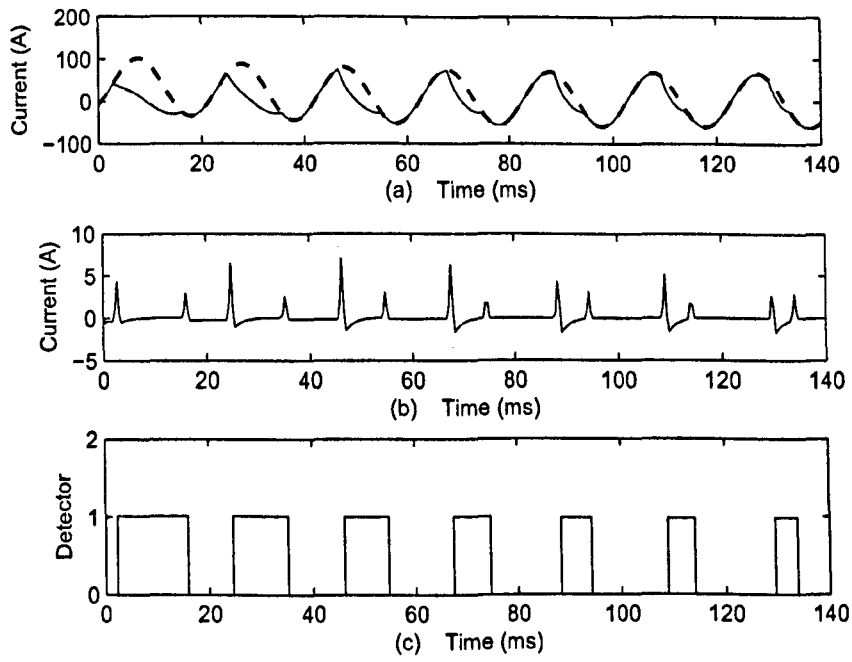

Figure 5.7: The case of an 80% residual flux with a three phase-ground fault; (a) the primary (dashed line) and distorted secondary current (solid line); (b) the detail signal d extracted from the secondary current; (c) saturation detection output.

successfully detected, by the proposed MLS, as shown in Fig. 5.8(c).

Tests on various faults and CT conditions are simulated and the results obtained indicate that the proposed CT saturation detection algorithm accurately estimates the secondary current irrespective of the magnitude of the primary time constant, the fault types, the DC component, or the remanent flux.

5.5.5 Compensation results

The distorted secondary currents in the above cases can be reconstructed, based upon the detection results, using the proposed compensation algorithm. To evaluate the performance of the algorithm, the transient error for the com-

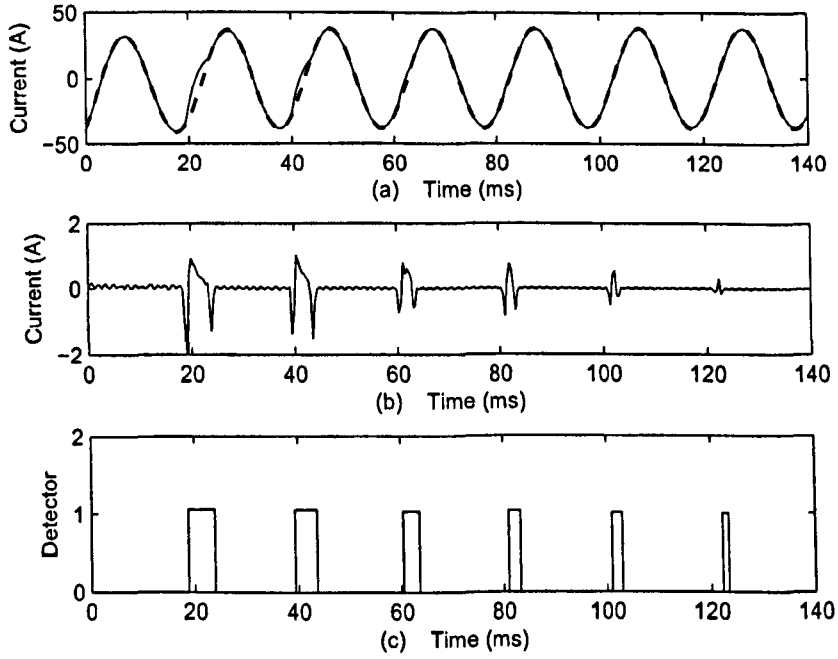

Figure 5.8: The case of an 80% residual flux with a single phase-ground fault; (a) the primary (dashed line) and distorted secondary current (solid line); (b) the detail signal d extracted from the secondary current; (c) saturation detection output.

pensated secondary currents is calculated at each sampling point as follows:

$$\text{transient error } (\%) = \frac{K_t \cdot i_2'(t) - i_1(t)}{I_r} \times 100(\%), \qquad (5.5.1)$$

where I_r is the rated magnitude of primary short-circuit current and K_t is the turns ratio of the CT. In this chapter, $K_t = 400$, since the 2000 : 5 tap was selected for the C400 class CT used in the simulation study.

Figure 5.9(a) is the compensation result of the distorted secondary current in Fig. 5.6(a), which is reconstructed based on the detection results indicated in Fig. 5.6(c). The maximum transient error shown in Fig. 5.9(b) is less than 3%, which indicates that the proposed compensation algorithm can accurately reconstruct the distorted secondary current during the period of CT saturation.

Figure 5.10 illustrates the compensation result for the case of an 80% residual flux with a single phase-ground fault, which has been indicated in Fig. 5.8.

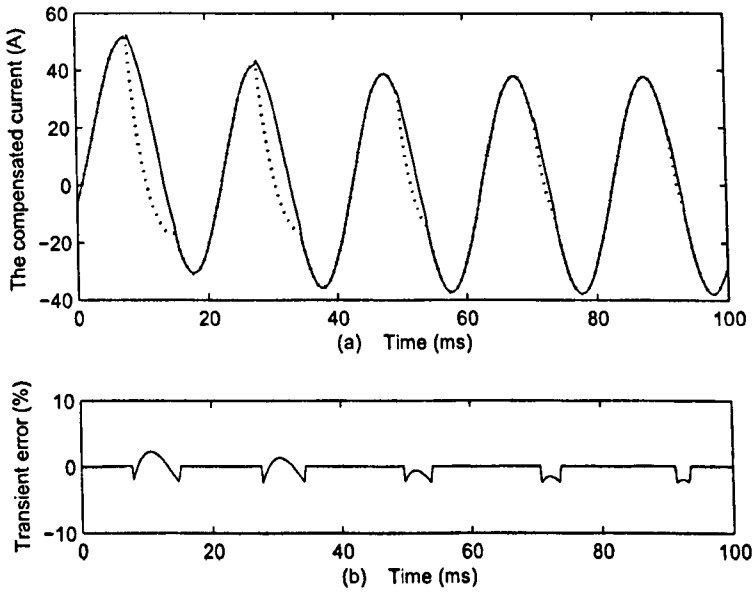

Figure 5.9: The compensation results for the secondary current in Fig. 5.6; (a) the saturated (dashed line) and compensated (solid line) secondary current; (b) transient error.

The solid line in Fig. 5.10(a) is the compensated secondary current obtained point by point at a sampling interval of 0.2 ms. The transient error is calculated and shown in Fig. 5.10(b). The whole compensation process does not require any additional parameters and can be fully implemented in real time.

The proposed MLS and compensation algorithm for CT saturation are much superior over the other existing methods, as most of the existing methods are based upon the assumption that there is no remanent flux in the core of CT. Obviously, this assumption is not practical and it is not used in our approach. In other words, without having the knowledge of the remanent flux, the other existing methods can by no means be compared with the proposed method.

5.6 Summary

This chapter has proposed a promising method using an MLS with a compensation algorithm for the saturation detection and the compensation of the

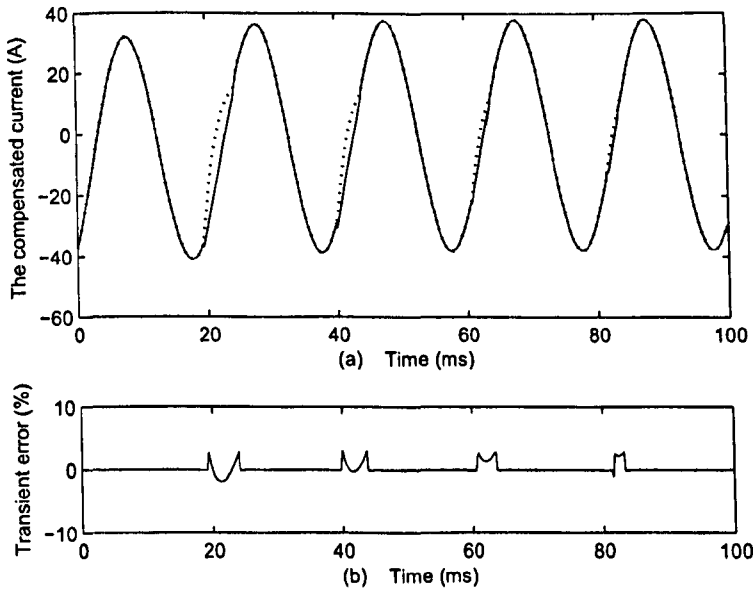

Figure 5.10: The compensation results for the secondary current in Fig. 5.8; (a) the saturated (dashed line) and compensated (solid line) secondary current; (c) transient error.

secondary current of CTs. The proposed method is based on the non-sinusoidal characteristics of the secondary current waveform during the saturation period. The detail level signal, after lifting by the scheme, has a zero or non-zero output, when the CT runs at normal or saturated conditions, respectively. It can accurately distinguish the distorted section from the healthy section in the current waveform. The distorted secondary current can be compensated in real time once saturation begins by using the proposed compensation algorithm.

The effectiveness of the proposed MLS and compensation algorithm have been tested on different cases on a sample power system. The faults used in the evaluation of the method are simulated in a wide range of conditions, including the residual flux in the CT core changing from -80% to 80% and the fault inception angle ranging from 0 to 180 degrees. Despite the wide variations, our method is able to detect the period of secondary current wave distortion accurately in all the test cases and then compensate the distorted secondary current point by point in real time. Since no presetting parameters

are needed for the MLS and compensation algorithm, they can be easily used to incorporate with the existing relays to improve their action speed without using conventional blocking schemes.

Chapter 6

A Morphological Lifting Scheme for Extra-High-Voltage Transmission Line Protection

This chapter presents a novel algorithm for ultra-high-speed (UHS) protection relays of EHV transmission lines, using an MLS. The MLS focuses on identifying the gradient of the wavefront of a travelling wave contaminated by noise. The proposed algorithm can be used for either transient positional or directional protection. It is evaluated through a variety of simulation studies which are carried out on a typical 400 kV EHV transmission system model using the power simulation program PSCAD/EMTDC. The simulation results show that compared with previous algorithms, the algorithm with the MLS provides more accurate responses under various fault conditions in comparison with previous algorithms, such as WT.

6.1 Introduction

Building modern EHV transmission networks is an effective method to increase power transfer. UHS protection has been recognised as an effective way of improving transient stability of power systems [97]. Most UHS protection re-

laying algorithms are transient-based, by analysing fault-generated transients, such as travelling waves or superimposed components [98]. The fault-generated transients are obtained from the incoming currents and voltages of a transmission line under a fault condition [99][100]. In comparison with the conventional protection relaying algorithms which analyse the fundamental component of a fault current or voltage, a transient-based algorithm has the advantages of fast response and immunity to the influences caused by saturation of current transformers, power swing and series capacitor compensation.

Most of the transient-based protection relays are designed for double-ended lines, that is, a directional comparison arrangement is accomplished by linking two terminals of a transmission line with a communication channel. Non-communication protection relays have also been developed by observing only the measurements of a transmission line at one terminal [100]. For the transient-based protection relays, the most important thing is how a sequence of wavefronts in a measured fault-generated transients are extracted. It is difficult for the conventional algorithms, such as Fourier transform, to achieve both high resolution in the frequency domain and accurate location in the time domain while processing a measured fault-generated transient signal, since the transient signal is non-stationary, and many non-periodic components are superimposed on the fundamental frequency waveform.

WT [101] is another approach using a short window for the analysis of high frequency content of a signal, while a long window for low frequencies. Thus WT is able to identify the details of localised transients of the signal rather than Fourier transform and gives a time-frequency representation of the signal, as it can provide the time and frequency information simultaneously. Its application has been widely investigated in fault location [102], high-impedance fault detection [103], as well as power quality detection and classification [104]. The advent of WT has given a great impetus to investigate the possibility of improving UHS protection [16, 105, 106].

Since WT has notable capabilities of detection and localisation of transients, the wavefronts of travelling waves may be possibly extracted by it. However,

its capabilities are often significantly degraded due to the existence of noise riding on the travelling waves, as the spectrum of the noise coincides with that of the transient components. The effect of the noise cannot be excluded by common filters of various filters without affecting the performance of WT. The travelling wave is easily to be contaminated by noise due to high sampling frequencies. WT has difficulty in distinguishing the wavefronts, as they are too faint to be detected from, from the noise or interferences, especially in the case of high impedance faults or low inception fault angles, where the gradients of the wavefronts are quite small. The accuracy of the WT detection result will be affected in such a noisy environment.

MM has been used to extract the wavefronts of travelling waves for UHS protection relays [107], but in a noise-free environment. This chapter presents an adaptive scheme, named MLS, as a powerful tool to eliminate noise. It is a signal decomposition scheme, based on the local shape of a waveform. Based on this scheme, a transient-based protection algorithm is proposed for EHV transmission line relays. In order to evaluate the proposed algorithm, simulation studies are undertaken using a typical 400 kV EHV transmission system model simulated with PSCAD/EMTDC. Various fault scenarios have been considered in different system configurations and operating conditions. The measured travelling waves are contaminated by adding random noise in the simulation cases. The simulation results show that the proposed algorithm is effective to eliminate the noise and capture the wavefronts.

6.2 Principles of transient-based protection

Transient-based protection relays utilise fault-generated high-frequency wave components to trigger fast relaying actions. When a fault occurs on a transmission line, both the travelling-wave voltage and current are transmitted at nearly the speed of light. A travelling-wave voltage or current is captured by a specially-designed transient detector and then converted into an aerial modal signal by modal transform. The fault line section on transmission lines is iden-

tified by comparing polarities of the sequence of wavefronts of the travelling wave, and the fault position is determined by calculating the time tags among the sequence of wavefronts [106].

6.2.1 Transient-based protection

Faults occurring on a high-voltage transmission line at an instant of a non-zero voltage will cause the pre-fault line charge to rapidly discharge, therefore, heavy surges are generated and will propagate as waves along the transmission line. These waves will travel close to the speed of light along both directions of the transmission line from the fault point and reflect at discontinuities along the line, including the fault point. Decaying high-frequency voltages and current transients are produced by repeated reflection of these surges. Each wave is composed of frequencies ranging from a few kilohertz to several megahertz and has a fast rising front and a slower decaying tail. These composite waves have a characteristic impedance that depending on the line parameters. The waves will not vanish until they are damped out and a new power system equilibrium is established. In an EHV transmission line, where the line length and the system capacitance are large, these transients become significant especially with small resistance in the faulty network. These transient signals, which will be identified as travellings waves, can be utilised to detect faults in power transmission lines.

The principle of travelling wave transmission is illustrated in Fig. 6.1. The transmission lines connect two sources at busbars m and n. Once a fault occurs at F, a point in the first half of the transmission line m-n, the travelling wave of voltage or current travels along the transmission line to both directions until it reaches the busbars m, n. The wave passed into the adjacent section and the rest is reflected backward. Let k_m and k_n be the reflection parameters at points m and n respectively. k_f and k_r represent the reflection and refraction parameters at the fault point, F. Suppose τ and τ' are the time periods as the first sequence of transients travelling wavefronts arrive at the busbars m and n

respectively. So the transients' voltages are represented as:

$$\begin{aligned} u_1(t) = \; & k_m u_F(t-\tau) + k_f k_m^2 u_F(t-3\tau) \\ & + k_m k_n k_r u_F(t-\tau-2\tau') + \cdots, \end{aligned} \tag{6.2.1}$$

$$\begin{aligned} u_2(t) = \; & u_F(t-\tau) + k_f k_m u_F(t-3\tau) \\ & + k_n k_r u_F(t-\tau-2\tau') + \cdots, \end{aligned} \tag{6.2.2}$$

where $u_1(t)$ and $u_2(t)$ are forward and reverse travelling-wave voltages observed at the busbar m. In the transient-based protection, the captured wavefronts can be theoretically calculated using (6.2.1) and (6.2.2).

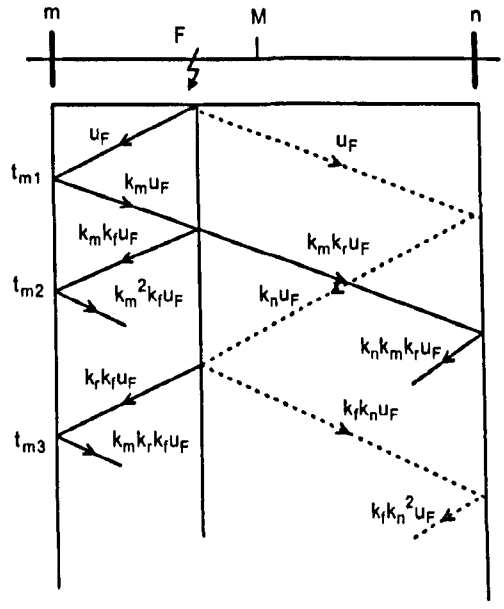

Figure 6.1: The analysis of a typical travelling wave grid.

6.2.2 Modal transformation

A line consisting of n conductors and ground has n modes of propagation, each of which has a particular voltage-current relationship, velocity and attenuation constant at any given frequency. To analyse the transient behaviour of a three-phase system, the voltages and currents need to be converted into modal quantities. Hence, the n-line system will be converted to n independent

modes by the modal transformation. Two transformation matrices are used to transform voltage and current signals:

$$\begin{aligned}[v(t)] &= [S][v^{(m)}(t)],\\ [i(t)] &= [Q][i^{(m)}(t)],\end{aligned} \tag{6.2.3}$$

where $[S]$ and $[Q]$ are the voltage and current modal transformation matrices, respectively. $[v^{(m)}(t)]$ and $[i^{(m)}(t)]$ are the modal voltage and current matrices. The inverse relationship is given as:

$$\begin{aligned}\left[v^{(m)}(t)\right] &= [S]^{-1}v(t)],\\ \left[i^{(m)}(t)\right] &= [Q]^{-1}[i(t)].\end{aligned} \tag{6.2.4}$$

The modal transformation matrices $[S]$ and $[Q]$ can be chosen to give independent modes of propagation. The most commonly used transformation is Clarke transformation [108]:

$$[S] = [Q] = \begin{bmatrix} 1 & 1 & 0 \\ 1 & -\frac{1}{2} & \frac{\sqrt{3}}{2} \\ 1 & \frac{1}{2} & -\frac{\sqrt{3}}{2} \end{bmatrix}, \tag{6.2.5}$$

$$[S]^{-1} = [Q]^{-1} = \frac{1}{3}\begin{bmatrix} 1 & 1 & 1 \\ 2 & -1 & -1 \\ 0 & \frac{1}{\sqrt{3}} & -\frac{1}{\sqrt{3}} \end{bmatrix}. \tag{6.2.6}$$

S is equal to Q in the special case of balances parameters. In general case, S is not equal to Q, and they are complex and frequency-dependent. There are three modes, two aerial modes and an earth mode, included in the modal quantities.

Earth mode [Mode 1]

This is the zero sequence component of the phase voltages and currents which is sent by Global Positioning System (GPS)-based tester. Its velocity and attenuation will be affected by the resistivity of the earth, hence it is frequency dependent. Velocity at low frequencies may be approximately 75% of the speed of light.

Aerial modes [Modes 2 and 3]

In aerial modes, the current in the 3 phases tend to be cancelled. Therefore, the effect of each resistivity in this mode is very small. The aerial modes are almost frequency independent and the velocities approach the speed of light.

6.2.3 Modal impedance and velocity

A three phase system,

$$[V] = [Z_c^{(p)}][I], \tag{6.2.7}$$

where Z_c^p is the phase characteristic impedance matrix, can be written as:

$$\begin{aligned}[V^{(m)}] &= [S]^{-1}[Z_c^{(p)}][Q][I^{(m)}] \\ &= [Z_c^{(m)}][I^{(m)}],\end{aligned} \tag{6.2.8}$$

using the modal transformation, where $Z_c^{(m)}$ is the modal characteristic impedance matrix. For a fully transposed line section, $[Z_c^{(m)}]$ is diagonal:

$$[Z_c^{(m)}] = \begin{bmatrix} Z_0 & 0 & 0 \\ 0 & Z_1 & 0 \\ 0 & 0 & Z_2 \end{bmatrix}, \tag{6.2.9}$$

where Z_0 is the impedance of the earth mode and Z_1 and Z_2 are the impedances of the aerial modes. They have the values of:

$$\begin{aligned} Z_0 &= Z_{0s} + Z_{0m}, \\ Z_1 &= Z_2 = Z_{0s} - Z_{0m}, \end{aligned} \tag{6.2.10}$$

where Z_{0s} is the self impedance term of phase characteristic impedance matrix; Z_{0m} is the mutual impedance term of phase characteristic impedance matrix.

The three modes have different velocities. The velocity of earth mode depends on the ground impedance, while the velocities of the aerial mode are almost independent of the ground resistivity, hence, are close to the speed of light. Generally, Mode 3 velocity is slightly higher than that of Mode 2.

6.3 Extra-High-Voltage transmission line protection with a morphological lifting scheme

Since transient-based protection techniques are based on the extraction of the characteristics of transient components generated by a fault and its concomitant arcing, a high sampling rate is always set to guarantee that the wavefronts of travelling waves are caught. Consequently, the sampled signal of the travelling wave may easily be disturbed by noise. If noise cannot be eliminated, a transient-based protection relaying algorithm will not be applicable, since the wavefronts cannot be detected under such a noisy condition. Most of the existing tools used to extract the features of wavefronts are sensitive to noise, which may enlarge the noise by processing it while extracting the gradient of a wavefront. For example, a traditional low-pass filter is used to restrain the high-frequency noise to some extent. However, at the same time the gradients of the wavefronts are attenuated as well.

On the other hand, the wavefronts are represented as edges in some extent. Therefore, by comparing the shapes using MM, it is not difficult to discriminate the wavefronts from the travelling wave in a noisy environment. Using the MLS, which is introduced as follows, the noise can be filtered without affecting the edges. Meanwhile, the wavefronts can be identified reliably.

6.3.1 Edge-avoiding prediction

The prediction operator should be chosen according to the features of the travelling wave. To design the prediction operator for the lifting scheme, the local samples of the travelling wave are analysed to determine if it is well approximated by a low-order polynomial for each prediction window. If it is, then a high-order predictor is used with a long window, which corresponds to a smooth basis function. If the samples do not meet the smoothness criteria, it needs to determine which point in the prediction window contributes to the failure. Then the point is classified as an edge point or a discontinuity coefficient. As the predictor window moves to edges, the order of the predictor

is reduced so that the neighbourhood used for prediction never overlap the edge. In this manner, large errors are avoided around the edges in the lifting scheme.

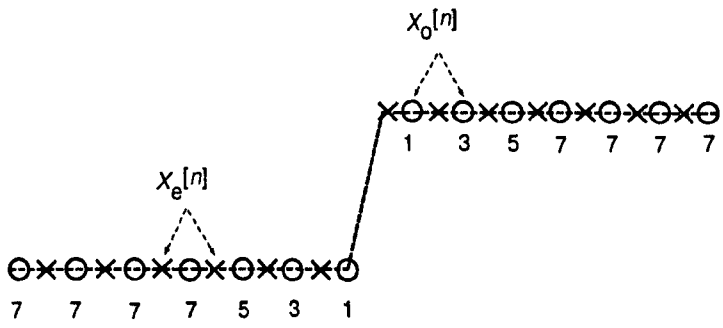

Figure 6.2: An ideal step edge.

All samples can be classified into edge and non-edge points based on edge pre-recognition using MM. In Fig. 6.2, the process of selecting these predictors near an ideal step edge is illustrated, where $x_e[n]$ and $x_o[n]$ are even and odd samples respectively. The definitions of predict and update operators are given in Chapter 1. For a region containing non-edge coefficients, a 7th-order predictor is used, while the order of the predictor is reduced near the edge to make the prediction never overlaps the edge. All relevant equations are presented in Section 6.3.3.

6.3.2 Morphological edge recognition

MM has been widely used in signal and image processing because of its simple operation and robust performance. The underlying basis of MM is to process signals by a function, known as an SE in general or a structuring function for a signal. The SE slides through the signal as a moving window, inspects its interaction with the signal, and detects specific features of the signal. Morphological operators are able to preserve or suppress the feature represented by SEs and obtain results with only components of interest. Therefore, the underlying shapes of the signal can be identified, reconstructed and enhanced

from its noisy, distorted forms. The signal with only components of interest can then be obtained by separating the waveform into various levels of details.

The edges in a waveform are identified by comparing different morphological gradients. The morphological gradient is defined as the arithmetic difference between the results of dilation and erosion:

$$\rho = f \oplus g - f \ominus g. \tag{6.3.1}$$

where f is the signal and g is an SE, $\oplus$ and $\ominus$ represent dilation and erosion respectively.

For instance, a prediction window is defined including 7 samples. As the centre of the predictor window moves to the point $s_{j,2l+1}$, the seven samples included in the window are:

$$[s_{j,2l-4}, s_{j,2l-2}, s_{j,2l}, s_{j,2l+1}, s_{j,2l+2}, s_{j,2l+4}, s_{j,2l+6}]. \tag{6.3.2}$$

Different SEs, g_i, are defined as flat lines with lengths of l_i ($l_i = i$, where $i = 2, 3, \cdots, 6$). The rightmost point of the SEs window is set at $s_{j,2l+4}$. So a group of morphological gradients are calculated as:

$$\rho_i = f \oplus g_i - f \ominus g_i. \tag{6.3.3}$$

Another group of gradients are calculated based on the point $s_{j,2l+4}$ as well:

$$\rho'_i = |s_{j,2l+2i+2} - s_{j,2l+4}|, \quad i = 2, 3, \cdots, 6. \tag{6.3.4}$$

ρ'_i and ρ_i are put together according to the index i. The maximum in each group can be found as $\rho_i \vee \rho'_i$, where $\vee$ denotes maximum or dilation. If a sequence of ρ'_i according to the index i is found to be the maxima in each group, the point $s_{j,2l+6}$ can be recognised as an edge point. Consequently, the length of the predictor window is decreased to avoid large error around edge points.

6.3.3 Noise filter

Let $(s_{0,j})_j$ denote the original signal of interest, $(s_{1,j})_j$ and $(d_{1,j})_j$ the low-pass and high-pass coefficients respectively with application of a lifting scheme.

A family of lifting transforms of Deslauriers-Dubuc wavelets are employed to eliminate the noise. The family of wavelets have names in form of $(N, \tilde{N})$, where N is the number of vanishing moments of the analysing high-pass filter, while $\tilde{N}$ is the number of vanishing moments of the synthesising high-pass filter. In the predict stage, we choose a 7th order predictor using the lifting transform of $(6,2)$ Deslauriers-Dubuc wavelet for a region non-edge detected. If an edge is detected, the order of the predictor window will be decreased to 5, 3 and 1 using the lifting transform of $(4,2)$, $(2,2)$ Deslauriers-Dubuc and Harr wavelets, respectively. The lifting transforms of these wavelets are denoted as:

$$\begin{aligned}
\text{Harr}: \quad d_{1,l} &= s_{0,2l+1} - s_{0,2l}, \\
s_{1,l} &= s_{0,2l} + d_{1,l}/2; \qquad (6.3.5) \\
(2,2): \quad d_{1,l} &= s_{0,2l+1} - 1/2(s_{0,2l} + s_{0,2l+2}), \\
s_{1,l} &= s_{0,2l} + 1/4(d_{1,l-1} + d_{1,l}); \qquad (6.3.6) \\
(4,2): \quad d_{1,l} &= s_{0,2l+1} - [9/16(s_{0,2l} + s_{0,2l+2}) \\
&\quad -1/16(s_{0,2l-2} + s_{0,2l+4})], \\
s_{1,l} &= s_{0,2l} + 1/4(d_{1,l-1} + d_{1,l}); \qquad (6.3.7) \\
(6,2): \quad d_{1,l} &= s_{0,2l+1} - [75/128(s_{0,2l} + s_{0,2l+2}) \\
&\quad -25/256(s_{0,2l-2} + s_{0,2l+4}) \\
&\quad +3/256(s_{0,2l-4} + s_{0,2l+6})], \\
s_{1,l} &= s_{0,2l} + 1/4(d_{1-1,l} + d_{1,l}). \qquad (6.3.8)
\end{aligned}$$

The noise can be eliminated while the gradient of the edge is not affected and it is kept in the prediction results. For instance, a step signal corrupted by noise is presented in Fig. 6.3(a). DWT is applied to filter the noise by decomposing the signal into a certain approximation and a set of details. Figure 6.3(b) is the de-noised approximation of DWT. Large errors are found at the points around the edge position. However, by using the proposed MLS, predictor windows never overlap the edge, so the shape of the step signal is kept as shown in Fig. 6.3(c).

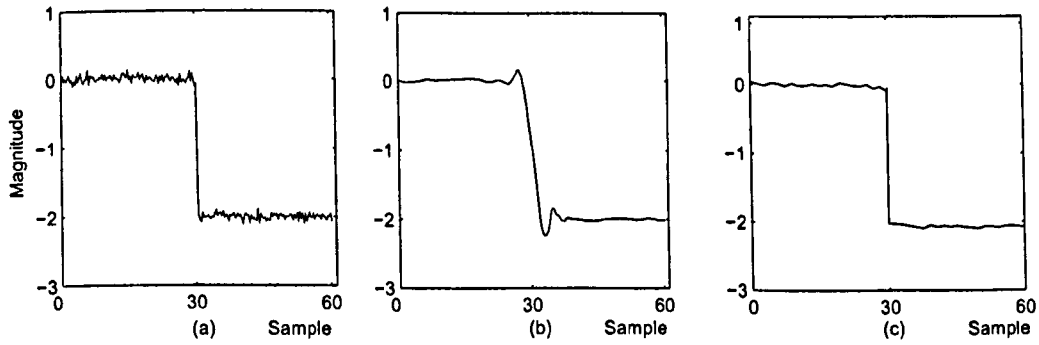

Figure 6.3: a) A step signal contaminated by noise; b) The approximation of DWT; c) The predictor result of MLS.

6.3.4 Wavefronts extraction and the protection algorithm

With the noise eliminated, there are two methods available to extract the sequence of wavefronts. The first one is the multi-scale DWT applying. A fourth-order Daubechies wavelet (Daub4) is to extract the wavefronts. The details of DWT can reveal the time-localising information of the wavefronts.

Another one is Multi-resolution Morphological Gradient (MMG) proposed in [107]. A couple of flat line SEs are defined for the purpose of the detection of both the locations and polarities of wavefronts.

The measured current or voltage is firstly processed by the proposed MLS, and then an MMG or a DWT is employed to extract the sequence of wavefronts in travelling waves. Based on the polarities and the time tags between the extracted wavefronts, the fault position or section can be identified.

6.4 Simulation and results

The proposed protection algorithm is verified using the power simulation program PSCAD/EMTDC [109][110]. A typical model of transmission line system is shown in Fig. 6.4, which is a layout of 400 kV EHV transmission lines used in the U.K. SuperGrid system. The length of the transmission line from terminal R to S is 128 km.

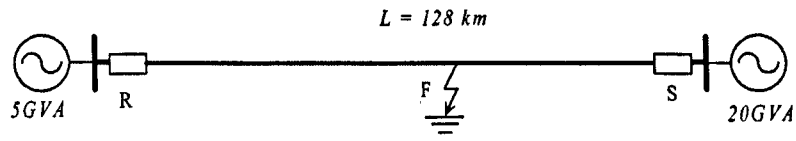

Figure 6.4: A single-line transmission line model for simulation.

A variety of fault scenarios, including different fault inception angles, fault resistances and fault types, have been simulated to evaluate the validity of the proposed algorithm. The sampling frequency in the simulation is 1 MHz. The proposed MLS selects a family of lifting transforms of Deslauriers-Dubuc wavelets to filter noise. The lifting transform of (6, 2) Deslauriers-Dubuc wavelet is applied for a region non-edge contained in a travelling wave; while the lifting transform of (4, 2), (2, 2) Deslauriers-Dubuc and Harr wavelets are used for the edge detected from the input data. The SE used in the MMG is a flat line with a length of 4 and a Daub4 wavelet is chosen as the mother wavelet in DWT.

6.4.1 Transient positional protection

Transient positional protection is a type of transient-based protection widely used in EHV transmission lines. Using the arrival of successive transient wavefronts, it can quickly and accurately pinpoint the fault position with information obtained from travelling waves.

Figure 6.5(a) shows a travelling wave generated by a solid phase-A-earth fault occurring at a distance of 80 km from busbar R indicated in Fig. 6.4. The observed currents at busbar R are firstly transformed into aerial modal signals. It is noted that the fault-generated travelling wave is superimposed on the power fundamental frequency component. For simulation purpose, the current travelling waves observed at the line terminals are polluted by Gause white noise. The mean and variance of the noise in simulation cases are 0 and 100 A, respectively.

In order to compare, a Daub4 wavelet is utilised to decompose the travelling

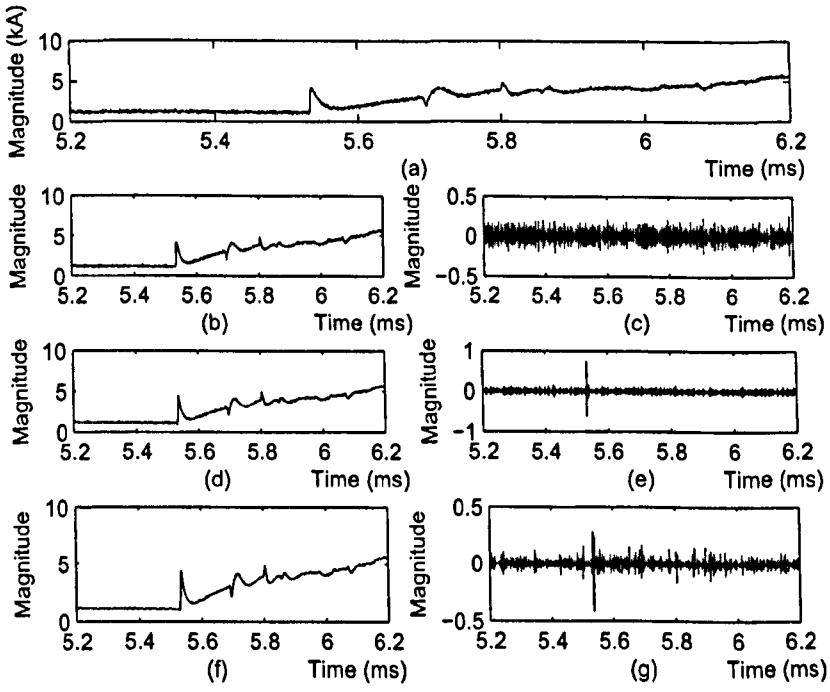

Figure 6.5: The results of DWT of the traveling wave generated by a single phase grounded fault at a distance of 80 km from busbar R. (a) The traveling wave polluted by noise; (b) The first-scale approximation of the DWT; (c) The first-scale detail of the DWT; (d) The second-scale approximation of the DWT; (e) The second-scale detail of the DWT; (f) The third-scale approximation of the DWT; (g) The third-scale detail of the DWT.

wave. As shown in Fig. 6.5, in a noisy environment, it is difficult for the DWT to detect the wavefronts in the travelling wave. All the wavefronts, except the first one, cannot be distinguished from the results of all three-scale details of the DWT, shown in Fig. 6.5(c), (e) and (g) respectively. It is not practical to decompose the travelling wave into a large scale, as it will use a longer sampling widow for the decomposition which will cause a time delay and more calculations.

Using the MLS proposed in this chapter, most part of the noise can be eliminated without affecting the gradients of the wavefronts. For the purpose of illustration, the first wavefront indicated in Fig. 6.5(a) is enlarged and then shown in Fig. 6.6(a). Figure 6.6(b) is the filter result by the MLS. In this figure,

the noise is reduced and the magnitude of the wavefront is not affected. Based on the results of the MLS, a MMG method is used to extract the wavefronts' features. The peaks in Fig. 6.7 can be recognised as location of wavefronts and the time-tags among the wavefronts are obtained. The first two wavefronts in Fig. 6.7 show opposite polarities, which indicates the second wavefront is reflected from the opposite busbar S. It can be concluded that a fault has occurred at a certain position in the second half of the transmission line. Then the distance to the fault position can be accurately calculated. The calculation process and equations are given in [106].

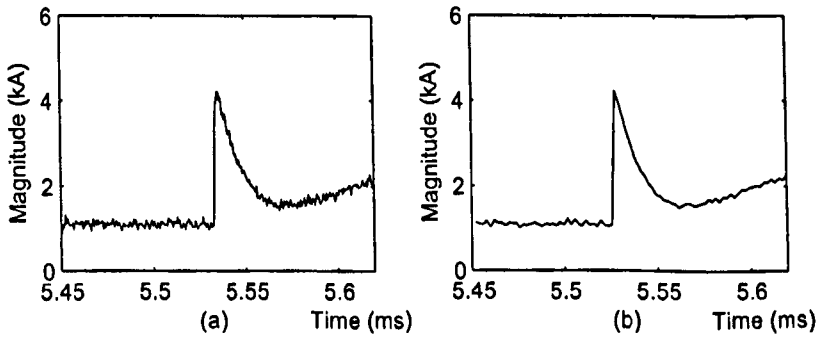

Figure 6.6: (a) The enlarged first wavefront indicated in Fig. 6.5(a); (b) The filter result of the MLS.

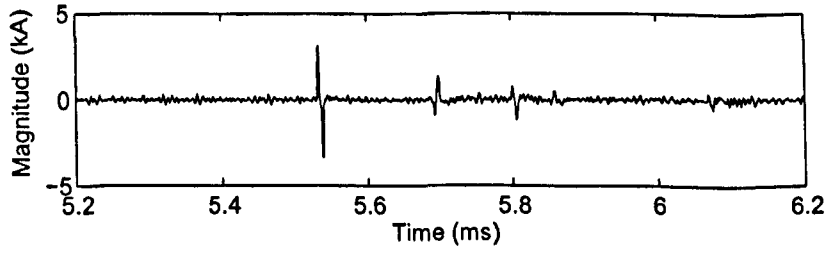

Figure 6.7: The results of the MMG for the detection of wavefronts in the travelling wave.

The satisfactory simulation results are obtained with regard to the following fault types. A double-phase grounded fault occurred at 20 km from busbar R in Fig. 6.4 and the travelling wave observed at the busbar R is shown in Fig. 6.8. To illustrate the effect of the MLS, three wavefronts indicated in Fig. 6.8

are enlarged and shown in Fig. 6.9(a). The wavefronts in Fig. 6.9(b) are more distinct than those indicated in Fig. 6.9(a) by applying the proposed MLS. After eliminating the noise by the MLS, the wavefronts can be extracted by the MMG. The detection result of the wavefronts indicates the occurring fault involves two phases. The accurate response can be given based on the results indicated in Fig. 6.10. Though the magnitudes of wavefronts are reduced due to the ground fault resistance, these indistinct wavefronts can still be recognised with the proposed MLS used for noise elimination previously.

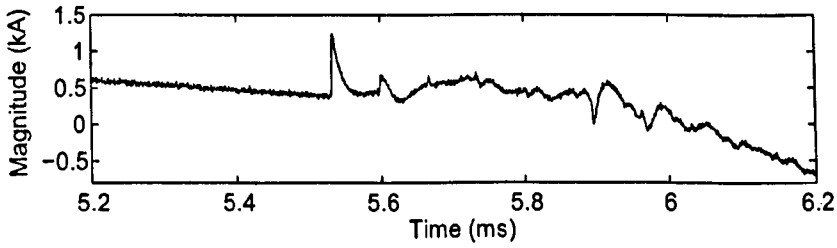

Figure 6.8: The travelling wave generated by a double-phase grounded fault in a noisy environment.

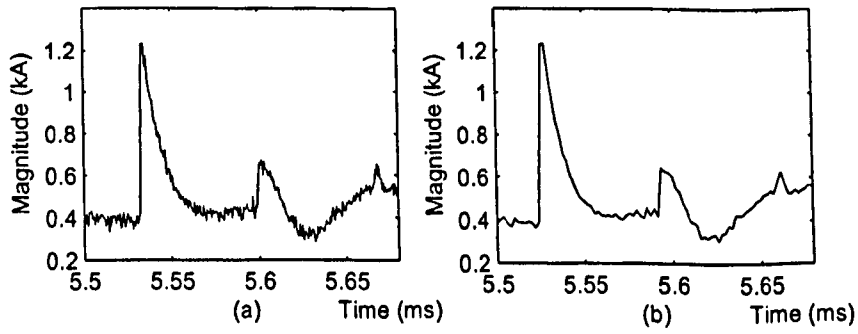

Figure 6.9: (a) The enlarged wavefronts indicated in Fig. 6.8; (b) The filter result of the MLS.

The results of fault location are not affected by the factors of different fault types, fault resistance and fault inception angle. A variety of tests were carried out with the following variations in the simulation condition:

i) *Fault locations*: Faults were introduced at 20, 68, 80, 108 and 126 km

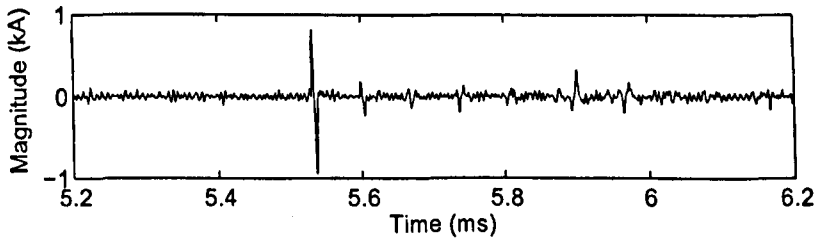

Figure 6.10: The results of the MMG for the detection of the wavefronts in the travelling wave.

from busbar R in the case of phase B and C to earth fault, and the results are listed in Table 6.1.

ii) *Fault types*: phase A to earth, phase B and C, phase A and B to earth, three-phase fault. The results are the same for different fault types.

iv) *Fault resistance*: 100 and 200 Ω. (see Table 6.2)

iii) *Fault inception angle*: $\delta = 15^o$, 45^o and 90^o. (see Table 6.3)

Table 6.1: Fault location results and error (%) for the transmission line

Actual Location (km)	Calculated Location (km)	error (%)
20	19.7321	0.2092%
68	67.8098	0.1486%
80	80.1367	0.1067%
108	107.7586	0.1886%
126	126.4668	0.3649%

For the cases of fault inception at zero crossing, theoretically, no travelling wave is generated from the fault point. Therefore, the transient-based protection relay cannot operate in this situation. A hybrid algorithm was proposed recently to overcome this theoretical shortcoming of transient-based protection, by including a traditional distance protection algorithm into the transient-based protection relay [111].

Table 6.2: Fault location results and error (%) affected by factors of fault resistance (A-G fault)

Inception Angle (degree)	Actual Location (km)	Calculated Location (km)	error (%)
100	20	19.7321	0.2092%
	68	67.8098	0.1486%
	126	126.4668	0.3649%
200	20	19.7321	0.2092%
	68	67.8098	0.1486%
	126	126.4668	0.3649%

6.4.2 Transient directional protection

Transient directional protection is used frequently to recognise the difference between currents being supplied in forward direction or backward in a transmission line. Firstly, the wavefronts of travelling waves at both ends of the protected transmission line are processed using the proposed algorithm. Then each pair of detection results of wavefronts, for each phase of currents at the two line terminals, are put together for the comparison of their polarities. Consequently, a fault can be discriminated between internal and external faults, and the fault type can be determined as well.

Another transmission system simulation model is shown in Fig. 6.11. It is composed of two sections of 400 kV transmission lines connected in series, which are represented by a distributed parameter model. The forward current direction is defined from busbars to the transmission line.

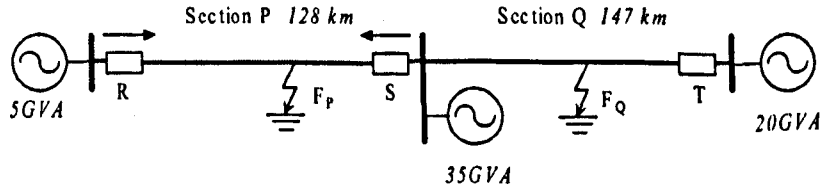

Figure 6.11: Two sections of 400 kV transmission line model for simulation.

Table 6.3: Fault location results and error (%) affected by factors of fault inception angle (A-G fault)

Inception Angle (degree)	Actual Location (km)	Calculated Location (km)	error (%)
15°	20	19.7321	0.2092%
	80	80.1367	0.1067%
	108	107.7586	0.1886%
45°	20	19.7321	0.2092%
	80	80.1367	0.1067%
	108	107.7586	0.1886%
90°	20	19.7321	0.2092%
	80	80.1367	0.1067%
	108	107.7586	0.1886%

To illustrate the identification of fault phases and fault line sections, a double-phase fault is simulated at a distance of 80 km to the right of busbar S on section Q. The travelling waves of three phase currents at both line terminals, R and S, are polluted by Gause white noise for simulation purpose. Using a MMG method followed by the MLS, the noise is eliminated and the detection results of the wavefronts at phase A and B are shown in Fig. 6.12, in which the polarities of the detected spikes of wavefronts can be recognised. Since the magnitudes of the spikes in phase A and B have large values in comparison with phase C and show different polarities for the two line terminals, an external A-B double line fault can be identified.

6.4.3 Directional protection with series compensation

Series Compensation (SC) has been widely applied to EHV transmission lines where the transmission distances are great and large power delivery is required. However, SC brings voltage and current inversions which cause difficulties for traditional power frequency component based differential relays to protect transmission lines. By exchanging the vital fault information of wave-

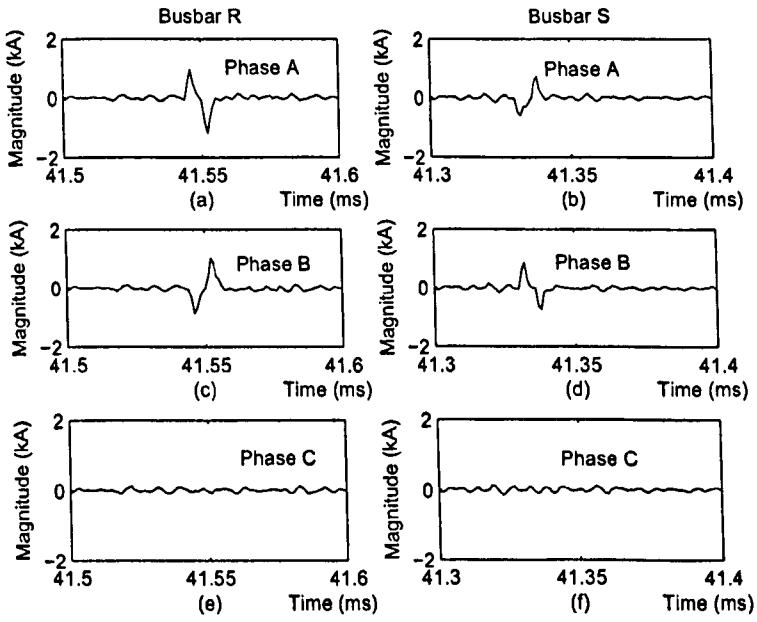

Figure 6.12: The wavefronts detection results of the three phase currents for an external double-phase (A-B) fault occurred in section Q.

fronts at both line terminals, the influence of SC is possible to be eliminated, because series capacitor has no effect on the wavefronts of travelling waves.

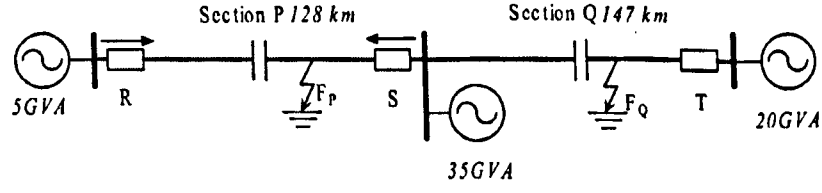

Figure 6.13: Two sections of 400 kV transmission line model with series compensation capacitor.

A simple series compensated transmission system is shown in Fig. 6.13, where the series capacitor bank is located in the middle of the lines. Figure 6.14 is the wavefront detection results of travelling waves under an external three-phase to ground fault at a distance of 47 km from busbar S in section Q. The local model current travelling waves are transmitted to a remote terminal for the comparison. The travelling wave is processed by the proposed MLS with a MMG to eliminate the noise and find the wavefronts' position for terminals

R and S. As shown in Table 6.4, to each pair of corresponding maxima M_{Ra} and M_{Sa} for detection results of wavefronts at both line terminals, the ratio δ (M_{Ra}/M_{Sa}) is calculated and the time tag τ for each pair of wavefronts is estimated. Since the values of τ and δ are quite close, the relay will tell the fault as an external fault and a correct trip signal will be issued.

The simulation case demonstrated here just gave a possibility that the transient-based directional protection could be applied in EHV transmission lines with SC. However, the simulation is based on a simple model without considering other elements such as capacitor protection. Therefore, a lot of studies relating to this issue need to be conducted in further research.

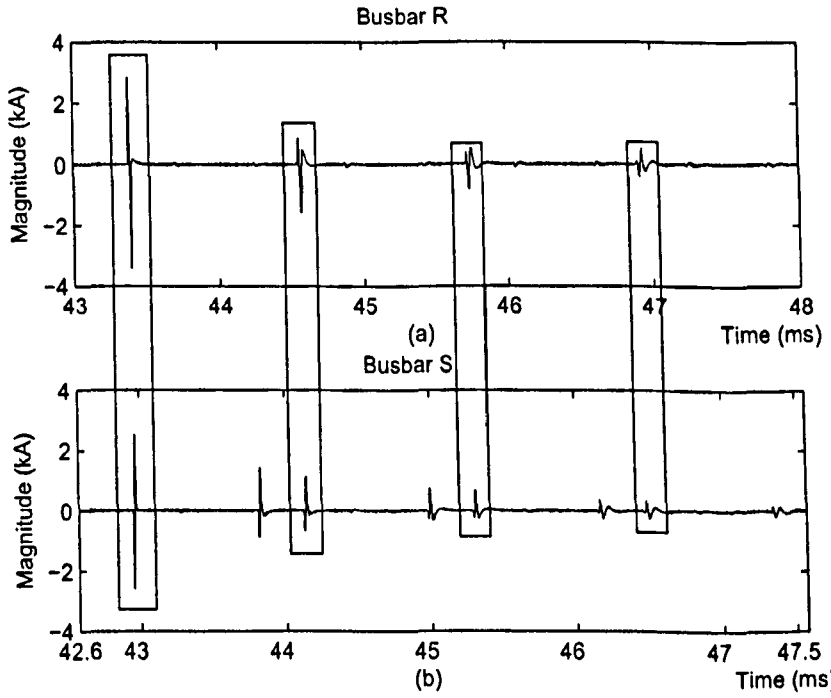

Figure 6.14: The detection results of the wavefronts of the travelling wave at two line terminals for an external three-phase ground fault occurring in section Q.

Table 6.4: The values of maxima and time tag of the wavefronts between each pair of wavefronts at two terminals

No.	1	2	3	4
M_{Ra} (kA)	3.402	1.533	0.840	0.511
M_{Sa} (kA)	2.500	1.118	0.616	0.374
σ	1.361	1.371	1.364	1.366
M_{Ra} Arrive time (ms)	43.376	44.548	45.721	46.905
M_{Sa} Arrive time (ms)	42.950	44.120	45.294	46.477
τ (ms)	0.426	0.428	0.427	0.428

6.4.4 Comparison with DWT and MMG

In order to present the merits of the proposed MLS, the results indicated in Fig. 6.7 are compared with those obtained by applying DWT solely. The travelling wave indicated in Fig. 6.5(a) is decomposed into a series of approximation and details by the DWT. The third-scale of the detail is shown in Fig. 6.15(b). For the purpose of comparison, the same travelling wave is firstly processed by the MLS twice to eliminate the noise; and the second-scale predictor result is then processed by the DWT, using the same mother wavelet, Daub4. The detection result is given in Fig. 6.15(c). Comparing the two detection results in Fig. 6.15(b) and (c), which are decomposed to the same scale (the third-scale with DWT), it can be observed that the detection result used the MLS, shown in Fig. 6.15(c), are more discriminable than the detection result using the DWT solely.

In comparison with DWT, the proposed MLS has a merit that less memory is required. In each updating or predicting step, all the samples in one stream are replaced by new samples using addition or subtraction. Each time, only the current streams are needed to update the sample values. In other words, the whole transform can be accomplished in place, without the requirement of auxiliary memory. This property makes the proposed scheme very promising for real-time implementation.

The results are also compared with those obtained using the MMG method

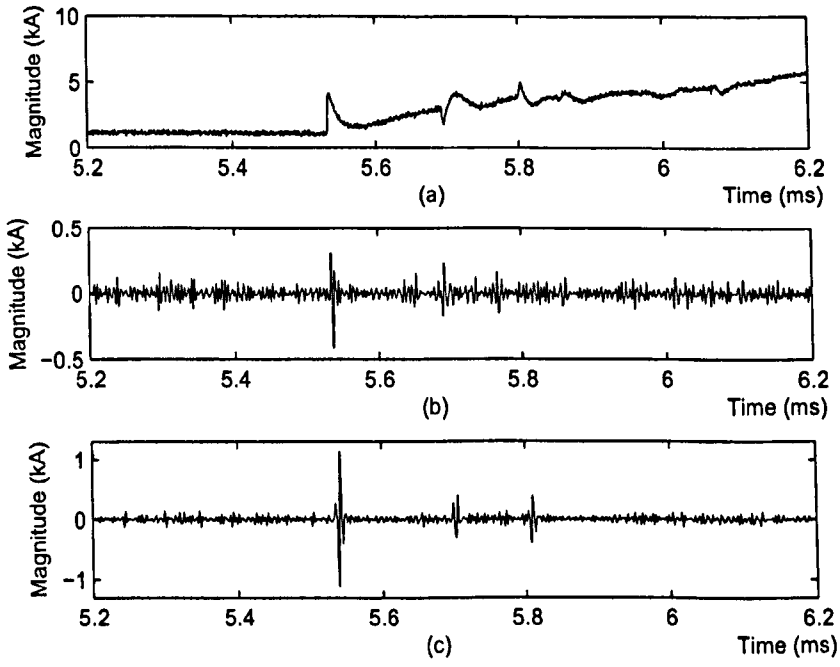

Figure 6.15: (a) The traveling wave indicated in Fig. 6.5(a); (b) The detail of the DWT at the third-scale; (c) The detail of the DWT at the first-scale with the MLS used twice.

alone. As shown in Fig. 6.16(b), the MMG is not able to distinguish the wavefronts from noise because the noise is amplified in the extraction of the wavefronts by the MMG. It denotes that the noise greatly degrades the practicability of the MMG method. However, with the use of the MLS, the wavefronts can be accurately detected based upon the peaks shown in Fig. 6.16(c).

6.5 The integration of morphological protection algorithms

A number of protection algorithms based on MM have been proposed in this thesis to deal with different faults. In order to reliably protect electric equipment, it always needs more than two different protection algorithms to work together. The coordination of these algorithms must be considered in

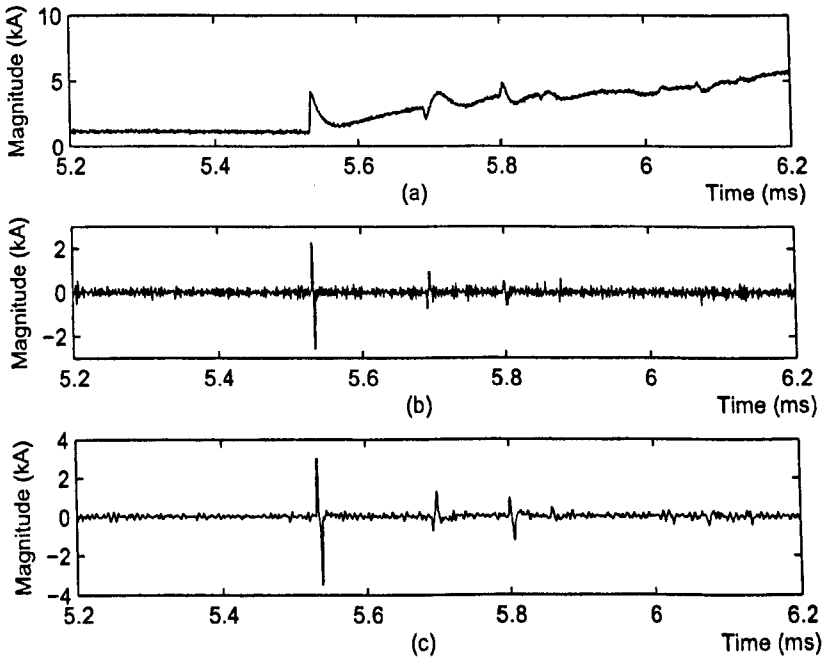

Figure 6.16: (a) The traveling wave indicated in Fig. 6.5(a). (b) The result of the MMG for the detection of the wavefronts of the traveling wave. (c) The result of the MMG after de-nosing by the MLS.

both of software design and hardware implementation for the development of a protection system in the future research.

Sampling frequency is a crucial element needing to be defined in the an early stage of the development. Usually, a relay selects a fixed sampling frequency for a whole system, which means the sampling frequencies for different morphological protection algorithms in the system should keep consistent. For the algorithms of CT saturation detection and compensation as described in Chapter 5, transformer inrush identification in Chapter 4, and DC offset cancellation in Chapter 3, the same frequency of $f = 2.4$ kHz could be selected as the sampling frequency, which represents 48 discrete samples are obtained for each fundamental cycle. For the algorithm developed for EHV transmission line protection in this chapter, it needs a higher sampling frequency up to 1 MHz to detect the features of the wavefronts. If another morphological protection algorithm, which is running in a low sampling frequency, needs to be

implemented into the UHS protection relay for an EHV transmission line, the samples for this algorithm should be recorded by consecutively selecting points in a fixed interval from samples. The value of the time interval depends on ratio of the sampling frequencies between the EHV transmission line protection relay and the morphological algorithm.

The diagram of an integration of the morphological protection algorithm developed in this thesis is illustrated in Fig. 6.17, where the process of a transformer protection is presented. Firstly, a consecutive current signal is converted into discrete samples using A/D converters. Then, the exponentially decaying DC offset of the discrete samples of the current is removed by a morphological filter. The filter results are identified by a CT saturation detection algorithm. If the input current has a saturated portion detected, the CT saturation compensation algorithm can recover the saturated waveform in realtime. Furthermore, the compensated current samples are transmitted to the block of transformer differential protection. Finally, if a trip threshold is satisfied, the current samples are decomposed by a morphological scheme as presented in Chapter 4 to distinguish between inrush and fault currents. If the current is recognised as an inrush, a block scheme is issued. Otherwise, a trip signal is given immediately.

The morphological algorithms presented in this thesis may provide more accurate and reliable protection for power system. Based the simulated cases, these algorithms can solve difficult problems in protection, such as transformer inrush identification and CT saturation detection, which can not be handled by conventional algorithms. The effectiveness of the algorithms depend on the future software design and hardware implementation. The limitation of these morphological algorithms is that it is difficult to find a fixed criterion for all situation. The criterion needs to be designed adaptively revisable in terms of system parameters.

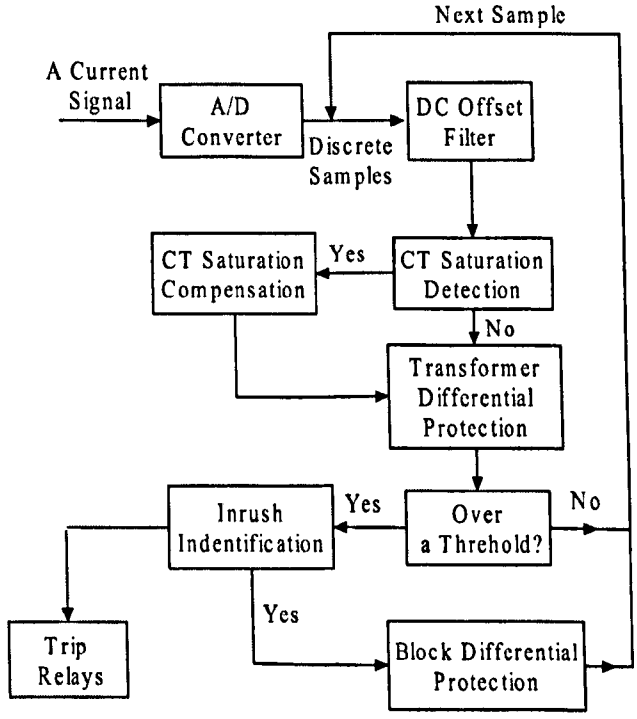

Figure 6.17: An integration of morphological protection algorithms for a power transformer.

6.6 Summary

This chapter has presented a new algorithm for EHV transmission line protection, based on an MLS which combines the advantages of lifting scheme and MM to degrade the effect of noise on fault-generated travelling waves. The MLS, a lifting scheme associating with a morphological edge detector, is used to filter the noise and preserve the gradients of wavefronts. The simulation results have demonstrated that the proposed algorithm is capable of eliminating the noise and extracting wavefronts effectively in different situations, either transient positional protection or directional protection. With the proposed MLS, traditional methods, such as MMG or DWT, can provide correct response to a transmission line fault under different fault conditions in a noisy environment. It also makes the proposed algorithm more powerful in extracting the transient features, thus greatly enhance the reliability and

sensitivity of EHV power system protection.

Chapter 7

Power Disturbances Identification and Monitoring

Power disturbances have always been an important issue to electricity consumers at all levels of usage. In the first part of this chapter, a new method, based on MM, is constructed for the detection and classification of power disturbances online. The proposed morphological transform technique extracts the features of disturbances from the signals in the time domain and detects the location and duration of the disturbances. A variety of power disturbances have been simulated to evaluate the validity of the technique. The advantages of the technique are also addressed in comparison with the WT.

In the second part of this chapter, an Empirical Mode Decomposition (EMD) technique is presented as a powerful tool for monitoring power quality in electrical power systems. As a multi-resolution signal decomposition technique, EMD has the ability to detect and localise transient features of power disturbances. Firstly, the theoretical background of EMD is briefly introduced and discussed. Then the technique is presented in detail and applied to extract the features of power disturbances. Finally the practicality and advantages of the EMD is discussed based on the simulation results obtained from several scenarios of power disturbances. The results demonstrate the potential of the proposed methodology for power quality monitoring and assessment.

7.1 Introduction

In recent years, electricity consumers are increasingly being affected by power quality issues. Power quality has been one of the main concerns over the operation of utilities and manufacturing industries [112]. The power quality is degraded largely by the use of solid state switching devices, non-linear and power electronically switched loads, lighting controls, industrial plant rectifiers and inverters and the operation of unbalanced power systems. Power quality identification has been considered as an important issue in power systems [113][114]. Low power quality can cause system equipment malfunction, computer data loss, malfunction of programmable logic controller, protection relays and sensitive loads such as computers, and erratic operation of electronic controls. Moreover, from the economical viewpoint, the utilities' revenue may also get effected at a higher cost due to the degraded power quality [115][116]. For these reasons the need for electric power quality identification and analysis is strongly increasing for both customers and electrical utilities [117, 118, 119].

7.2 Power quality

7.2.1 Definition

Electrical power quality refers to different things for different people, thus there is no commonly agreed upon definition for it. Besides, power quality at transmission level is not the same as it is at the distribution level [120]. But in general, power quality refers to the characteristics of supply voltage that affects the load performance. The most common definition of power quality is the ability of a power system to operate loads without disturbing or damaging them. It describes the state of the system voltages for which the electrical energy can be utilised from the distribution system successfully, without any interference or interruption [121].

From a broader perspective, power quality embraces the quality of service offered wave-shape, system reliability, electrical system design and construc-

tion errors, grounding errors, voltage imbalance, long-term outages and load interactions. On the other hand, a restricted definition of power quality simply focuses on waveform distortion or voltage quality at the point of common coupling, a point at which the residences are energised by the secondary distribution voltage.

7.2.2 Power quality standards

It has been widely recognised that well-established power quality standards are essential for the power quality industry. The ultimate goal of standardisation is to resolve problems and prevent social and economical losses associated with power quality disturbances. Power quality standards have defined normal and various abnormal operation conditions, provide terminology for effective communication in the industry, and reduce some of the problems caused by explicitly putting limitations on electrical equipment design and implementation. Many power quality standards have been defined by several organisations, such as the Institute of Electrical and Electronics Engineers (IEEE), American National Standards Institute (ANSI), National Institute of Standards and Technology (NIST), National Fire Protection Association (NFPA), Nation Electrical Manufactures Association (NEMA), Electrical Power Research Institute (EPRI) and International Electrotechnical Commission (IEC).

IEEE 1159 standard

The IEEE Standard 1159 defines power quality problems as a wide variety of electromagnetic phenomena that characterise the voltage and current at a given time and at a given location in the power system. The standard covers the monitoring of electrical power quality of AC power systems, definitions of power quality terminology, impact of poor power quality on utility and customer equipment and the measurement of electromagnetic phenomena [122]. The IEEE Standard 1159 serves as an important reference for the research and development activities in the field of power quality.

ITI(CBEMA) curve

The Information Technology Industry (ITI) council curve is a newer version of the Computer Business Equipment Manufacturers Association (CBEMA) curve. It describes an AC input voltage envelope that can be tolerated by Information Technology Equipment (ITE) and covers both steady-state and transient conditions. Eight types of events are described in this composite envelope, namely: steady-state, voltage swells, low-frequency decaying ring waves, high-frequency impulse and ring waves, voltage sags, dropouts, no damage events, and prohibited events [123]. However, this curve is not intended to serve as a design specification of products or for AC distribution systems.

IEC power quality standard

IEC has a series of international standards on power quality. IEC Std. 61000-1-X provides the power quality definitions and methodology. It defines the limits of harmonics emissions. IEC Standard provides guidelines on tests and measurements. In addition, as well as provides information on low frequency Electro Magnetic Compatibility (EMC) phenomena, which is essential for the equivalent of power quality. IEC SC77A/WG1 is on harmonics and other low-frequency disturbances; SC77A/WG2 is on voltage fluctuations and other low-frequency disturbances; SC77A/WG6 is on low frequency immunity tests; SC77A/WG8 is on electromagnetic interference related to the network frequency; SC77A/WG9 is on power quality measurement methods; and SC77A/PT 61000-3-1 is on EMC.

7.2.3 Power quality disturbance types

In general sense, anything that causes the power system voltage or current to deviate from the ideal sinusoidal waveform could be considered a power quality disturbance. IEEE 1159 Standard divides power quality disturbances into several different categories. A given disturbance can generally be considered to belong to one of two broader classes: transient disturbances and steady-state

disturbances.

Steady-state disturbances

The class of steady-state disturbances encompasses the long-term variations on power system. The term "steady-state" implies disturbances of long duration that change little with time. Example of steady-state power quality problems include sustained interruptions, *i.e.*, power outages lasting longer than one minute, long-term over-voltage or under-voltage conditions and steady-state waveform disturbances caused by power system harmonics. Several of the steady-state disturbances are well-quantified by measures such as reliability indices or total harmonic distortion levels. For the purpose of helping limit the effects of such disturbances, steady-state voltage tolerance limits [124] and harmonic levels [125] are specified by power quality standards.

Transient disturbances

The duration of transient power quality disturbances are less than than steady-state disturbances, with is shorter than one minute or only a few cycles. The transient disturbances may be further subdivided into three subcategories: impulsive transients, oscillatory transients and short duration variations. A number of different disturbance types are contained in these three subcategories. In contrast to steady-state disturbances, which persist for a relatively long time, transient disturbances appear as a temporary interruption in the steady-state, and then the power system typically returns to normal or possibly to a new steady-state condition.

An impulsive transient, often caused by lighting, is defined as a sudden, non-power frequency change in steady-state condition of voltage or current. An oscillatory transient is typically caused by switching of various types of power system equipment, is similar to an impulsive transient except that it includes both positive and negative polarities. Both impulsive and oscillatory transients may be characterised by quantities such as frequency content, peak magnitude, rate of change and duration [126]. Short duration variations are

still transient in nature even though they differ in type and duration from impulsive and oscillatory transients. The short duration variations typically last longer, having a normal duration of at least a few cycles, as opposed to fraction of a cycle for the other two classed. Short duration variations include transient voltage increases (swells) and decreases (interruptions) with durations of less than one minute. These short duration variations can be further sub-categorised by duration as instantaneous (lasting from 0.5 to 30 cycles), momentary (from 30 cycles to 3 seconds), and temporary (3 seconds to one minute). Voltage sags are the most common of the three types of short-duration variations, are typically associated with faults or changes in the system configuration, such as the starting of large electrical motors.

7.2.4 Disturbance analysers

The DFT is applicable to the recorded data and has been a popular tool in the analysis of power disturbances. Implemented by various algorithms, the DFT has been regarded as the basis of modern spectral and harmonic analysis. Its calculations capability has been added to some disturbance analysers to obtain a clear picture of the harmonic content within the distorted signal.

However, the DFT can not provide any information about the time domain, which is very important for power quality analysis since time-frequency information is needed to analyse some particular distorted portion of the signal. Therefore, in contrast to its successful application to periodic signals, the Fourier transform is not as efficient in tracking a transient signal due to the limitation of getting time-frequency information simultaneously.

In order to overcome this limitation, some proposals based upon the WT were introduced in the early 1990s which provide time information as well as frequency information [127, 128, 129]. In contrast to the Fourier transform where a uniform window is used for different frequencies, the WT uses short windows at high frequencies and long windows at low frequencies. Thus the WT is capable to identify the details of localised transients than the Fourier transform. Using this technique, the characteristics of non-periodic distur-

bances can be more closely monitored. However, the WT is calculated using the sampled data of the signal which covers a certain period of time to reveal the periodic characteristics of the signal. Therefore, the extraction of disturbance features requires the use of a window of adequate length and a high sampling frequency to ensure that the detail is extracted, which increases the computational burden and reduces the attractiveness of the technique.

MM has become increasingly important in image and signal processing. In contrast to the Fourier transform and WT, MM is concerned with the shape of a signal waveform in the complete time domain rather than the frequency domain. MM only involves comparisons for finding maxima/minima, or the addition/subtraction of signals, thus making calculation significantly faster [130]. In this chapter the concept of MM is used to develop an analyser, which is applied to several popular power system disturbances to extract meaningful components from the signals. The concept of MM and the proposed method are introduced in Section 7.3. Tests on several different disturbances are simulated and discussed in comparison with WT in Section 7.4.

7.3 The morphological transform for power disturbance identification

7.3.1 Noise filter

It is well known that a morphological transform, such as a Morphological Filter (MF), is based on erosion and dilation. A widely used MF is the Morphological Mean Filter (MMF) which is derived from the addition of dilation and erosion. Letting S and G represent the input signal and the SE respectively, the MMF is denoted by ψ:

$$\psi_G = \frac{1}{2}(\delta_G(S) + \varepsilon_G(S)), \tag{7.3.1}$$

where $\delta_G(S)$ and $\varepsilon_G(S)$ denote the dilation and erosion of the signal S by the SE G.

An illustration of the MMF in action with a flat line SE can be seen in Fig. 7.1. MMF plays an important role in noise suppression especially for Gaussian white noise.

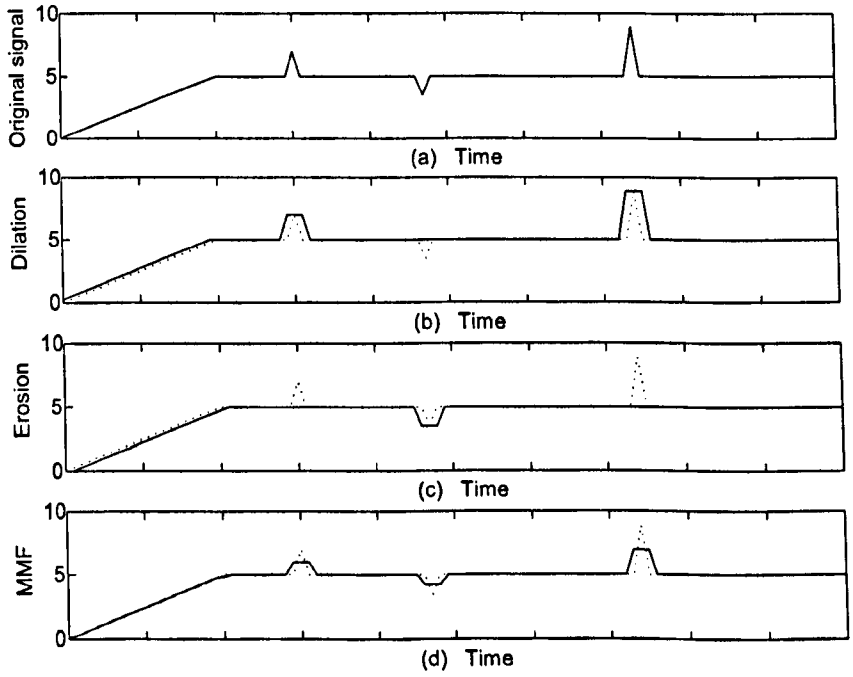

Figure 7.1: Illustration of the Morphological Mean Filter (MMF)
a) Original signal; b) Dilation of the signal; c) Erosion of the signal; d) Result of MMF.

7.3.2 Feature extraction

The Morphological Gradient (MG) is defined as the subtraction of erosion from dilation. The MG is denoted by ρ:

$$\rho_G = \delta_G(S) - \varepsilon_G(S). \tag{7.3.2}$$

MG can detect sudden changes of waveforms.

In [131] a Multi-resolution Morphological Gradient (MMG) was proposed to extract a travelling wavefront, which can suppress the steady-state components and enhance the transient ones.

A pair of scalable flat line SEs with different origins are designed as follows:

$$G^+ = \{g_1, g_2, \cdots, g_{l-1}, \underline{g_l}\}, \tag{7.3.3}$$

$$G^- = \{\underline{g_1}, g_2, \cdots, g_{l-1}, g_l\}, \tag{7.3.4}$$

where G^+ is the SE used to extract the rising edges and G^- is to extract the falling edges of the signal. The origin of G^+ is g_l and that of G^- is g_1. The length of the SE is represented by $l = 2^{1-a}l_G$, where a is the "level" of the SE and l_G the primary length of G, *i.e.*, its length at $a = 1$. For the example demonstrated in Fig. 7.2, $l_G = 3$ and $a = 1$.

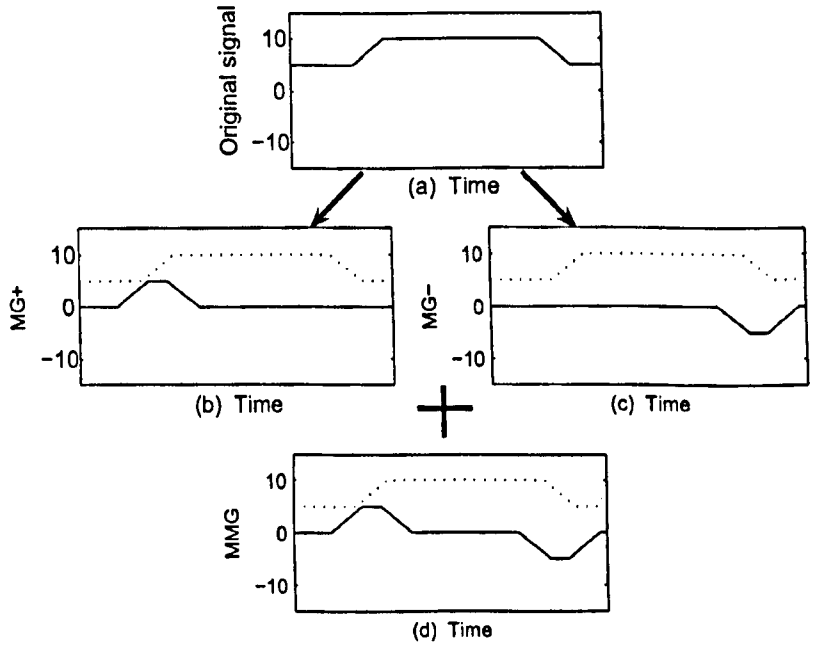

Figure 7.2: Illustration of Multi-resolution Morphological Gradient (MMG) a) Original signal; b) Result of MG+ using the SE, G^+; c) Result of MG- using the SE, G^-; d) Result of MMG.

Based on the definition of MG and SE, the dyadic MMG with level a can be defined as:

$$\rho^a_{G+} = \delta_{G+}(\rho^{a-1}) - \varepsilon_{G+}(\rho^{a-1}), \tag{7.3.5}$$

$$\rho^a_{G-} = \varepsilon_{G-}(\rho^{a-1}) - \delta_{G-}(\rho^{a-1}), \tag{7.3.6}$$

$$\rho^a = \rho^a_{G+} + \rho^a_{G-}. \tag{7.3.7}$$

When $a = 1$, $\rho^0 = S$ is the input signal. Since $\{\delta_G(\rho^{a-1}) \subset \varepsilon_G(\rho^{a-1}) : G \neq \varnothing\}$, then $\rho^a_{G+} > 0$ and $\rho^a_{G-} < 0$, which corresponds to the rising and falling edges of the signal.

Figure 7.2 illustrates the use of MMG. From Figure 7.2 it can be seen that ρ^a can detect not only the location of the waveform changes but also their polarities. In addition, the higher the level, a, the more details are revealed.

7.3.3 Proposed method

The core of the MM method proposed in this chapter is based upon combining the MMF and the MMG. The signal is first processed by an MMF to reduce the noise and then by the technique of quadratic MMG (level $a = 2$) to extract the features of the disturbances.

The extracted results can be used to detect and locate the disturbances. Since the result of MMG reflects the polarities of the sudden change of the waveform, the feature is also helpful for the classification of certain kinds of transients.

7.4 Detection and analysis of power disturbances

In order to verify the applicability of MM to power quality analysis, the proposed approach has been applied to investigate various types of disturbances: voltage dip, periodical notch, momentary interruption, voltage swell, oscillatory transients and voltage sag, respectively.

The disturbances have been simulated numerically, added to the fundamental sinusoidal wave, in addition the whole signal was polluted by white noise. The sampling frequency used was 5 kHz and the value of Signal to Noise Ratio (SNR) is 30 dB in each case of the simulation studies.

7.4.1 Case A: voltage dip

A voltage dip is a significant voltage reduction for a relatively short duration. It is caused by faults, increased load demand and transitional events such as starting large electrical motors.

Figure 7.3(a) shows a dip occurring in the period of a sinusoidal fundamental. Figure 7.3(b) displays the signal after filtering using MMF, and Fig. 7.3(c) illustrates the detection of the voltage dip by the MMG algorithm. Figure 7.3(c) shows that the voltage dip affecting the fundamental can be properly extracted by the MMG analysis. More tests have been carried out, by varying the duration and magnitude of the voltage dip, and similar results were obtained from these tests.

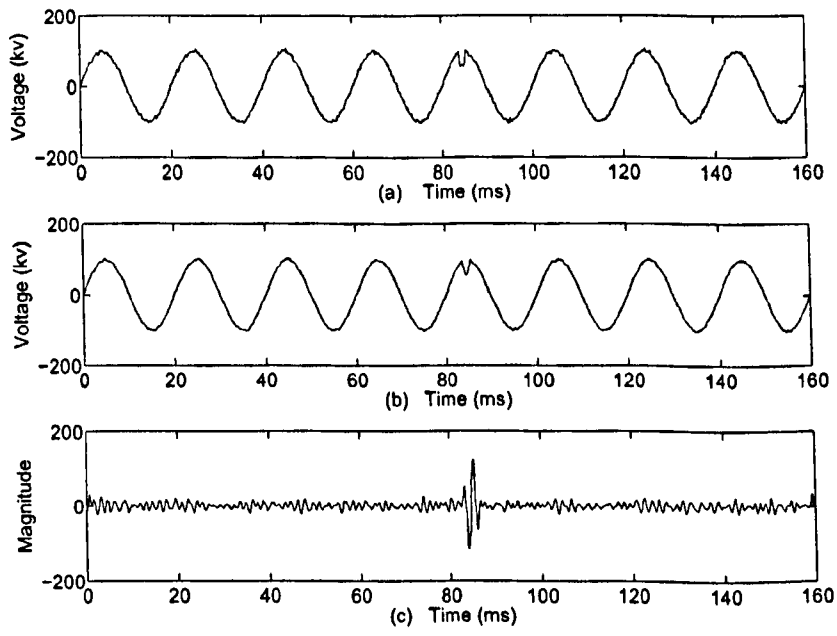

Figure 7.3: Analysis results for Case A - Voltage Dip
a) Fundamental with a voltage dip; b) Result of MMF; c) Result of MMG for detection of the dip.

7.4.2 Case B: periodical notch

A notch is a disturbance of opposite polarity from the waveform. It may be caused by lightning, static discharges, utility switching operations, starting or stopping major equipment or machinery, *etc.*

A fundamental waveform affected by a periodical sinusoidal notch from the third to sixth cycle is shown in Fig. 7.4(a). The result of the signal processed by MMF is illustrated in Fig. 7.4(b). Figure 7.4(c) is the result obtained using MMG to detect the notch based on the signal after MMF. Figure 7.4(c) illustrates that the disturbance time duration can be evaluated and estimated based on a series of points with distinct large magnitude values. Different tests have been undertaken by changing the notch frequency, amplitude and shape. Similar results have been achieved.

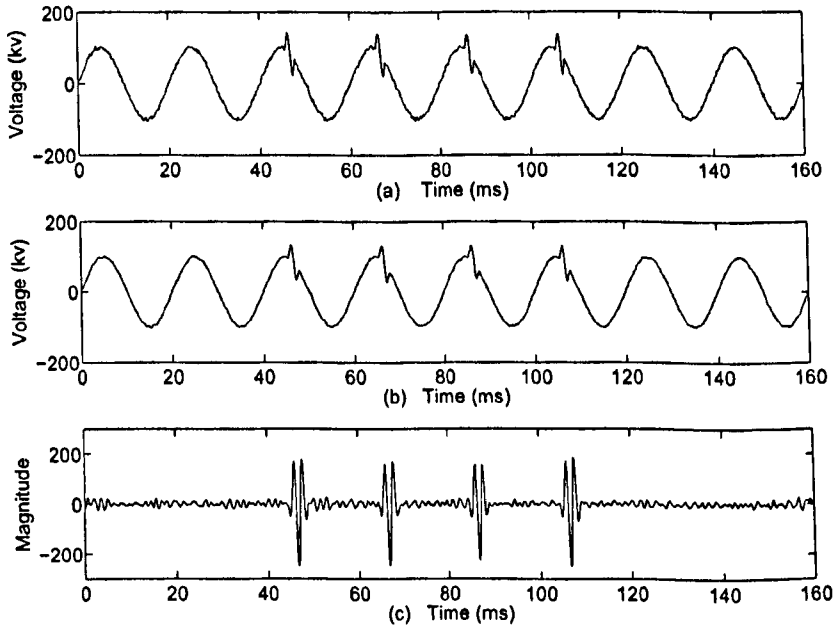

Figure 7.4: Analysis results for Case B - Periodical Notch
a) Fundamental with a periodical sinusoidal notch; b) Result of MMF; c) Result of MMG for detection of the notch.

7.4.3 Case C: momentary interruption

A momentary loss of voltage on a power system can be called a momentary interruption. Such a disturbance describes a drop of 90-100 percent of the rated system voltage lasting from 10 ms to 1 minute. They are often detected down-line from switch-gear such as circuit breakers, re-closers, or fuses.

Figure 7.5(a) depicts a momentary interruption beginning from the 3rd cycle of the signal. The disturbance was simulated to last 4 cycles in this test. Figure 7.5(b) shows the output of the MMF. The two peaks contained in Fig. 7.5(c) indicate the start and end of the occurrences of the disturbances respectively.

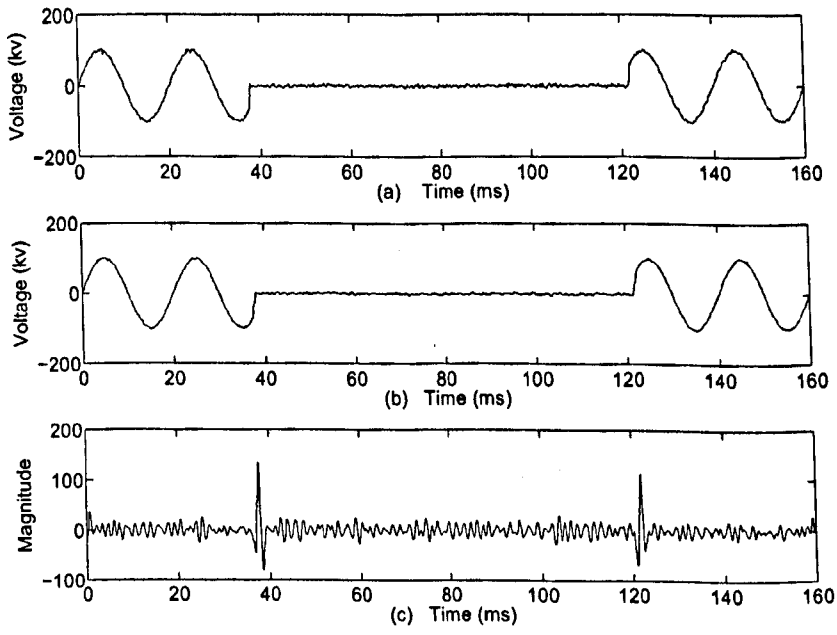

Figure 7.5: Analysis results for Case C - Momentary Interruption
a) Fundamental with a momentary interruption; b) Result of MMF; c) Result of MMG for detection of the momentary interruption.

7.4.4 Case D: voltage swell

A voltage swell is a short-term increase of system voltage. Such an event is often caused by an abrupt reduction in load or appears on the un-faulted phases of a three-phase circuit, where a single-phase short circuit has occurred. Swell may stress any delicate equipment components causing premature failure.

In Fig. 7.6(a), a voltage swell lasts from the 3rd cycle to the 6th in a fundamental sinusoidal waveform. Figure 7.6(b) illustrates the output of the MMF. The period of the voltage swell is detected by the second stage of the process, *i.e.* the application of the MMG. In Fig. 7.6(c), the start and end of the swell period are clearly indicated. More tests have also been undertaken by varying the swell amplitude range and the similar results have been obtained.

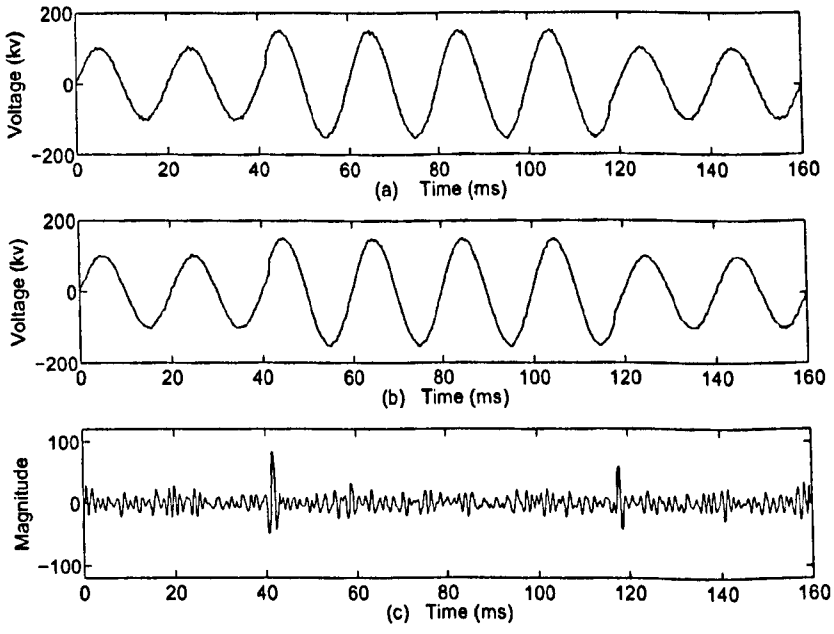

Figure 7.6: Analysis results for Case D - Voltage Swell
a) Fundamental with a voltage swell; b) Result of MMF; c) Result of MMG for detection of the voltage swell period.

The waveform of voltage swell in Fig. 7.6(a) is totally different from the momentary interruption waveform indicated in Fig. 7.5(a). However, both

the waveforms involve sudden changes, which can be seen from Fig. 7.6(a) where the voltage changes suddenly at 41 ms in the 3rd cycle and at 119 ms in the 6th cycle, and from Fig. 7.5(a) the voltage is disturbed at 39 ms and 121 ms respectively. These disturbances make the voltages change with the same characteristic which can be captured accurately by the proposed MMG. Therefore, the detection results shown in Fig. 7.6(c) are similar to the results indicated in Fig. 7.5(c). The difference between them can be recognised with a classification method introduced in the following section.

7.4.5 Case E: oscillatory transients

A transient is an undesirable momentary deviation of the supply voltage or load current. Transients are generally classified into two categories: impulsive and oscillatory.

The fifth case-study is related to an oscillatory transient. Such an oscillatory transient occurring during the period of a sinusoidal wave is shown in Fig. 7.7(a). Figure 7.7(b) illustrates the output of the MMF and the detection of the oscillatory disturbance by the MMG is shown in Fig. 7.7(c). From these figures, the location of the peak is found to correspond with the time scale when the oscillatory transient occurs. For the Fourier transform based methods, such a disturbance may not be easily detected. On the contrary, the MMG can extract the transients efficiently. More oscillatory transients have been simulated, by varying the oscillatory frequency, amplitude and damping exponent. The results obtained follow a similar pattern to that shown in Fig. 7.7(c).

7.4.6 Comparison with Wavelet transform

A WT can be applied to all the disturbances for comparison with the proposed method. As an example, a voltage sag is simulated in a noisy environment and detected by WT and the morphological transform respectively.

A voltage sag is a sudden reduction of the voltage magnitude, lasting 10 ms

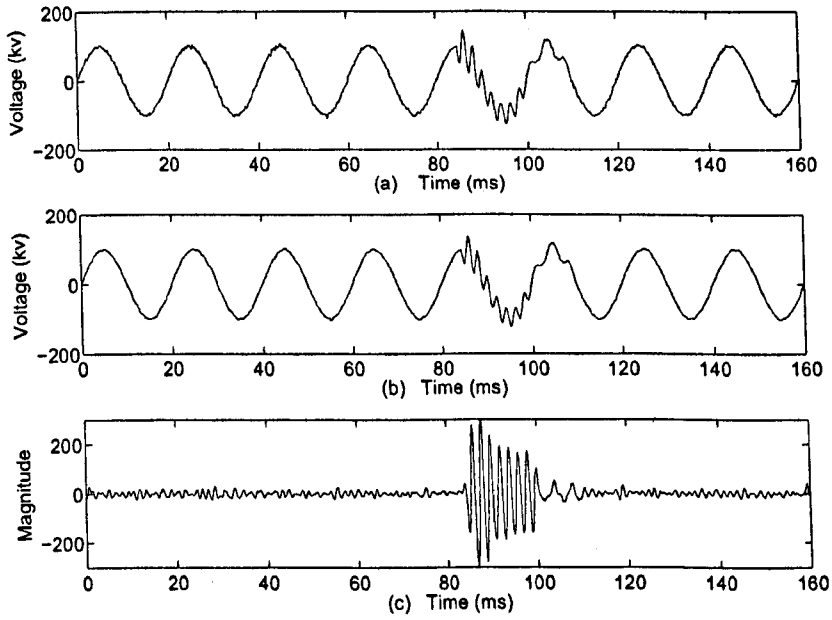

Figure 7.7: Analysis results for Case E - Oscillatory Transients
a) Fundamental with an oscillatory transient; b) Result of MMF; c) Result of MMG for detection of the oscillatory transients.

to several seconds. It may be caused by switching operation associated with temporary disconnection of supply, flow of heavy current associated with the starting of large motors or the flow of fault currents. The effect of the voltage sag on equipment depends on both its magnitude and duration.

WT and morphological transform have been used to investigate the sag characteristics respectively. For the purpose of comparison, both the approaches are used to extract the same sag waveform at the second-scale. Figure 7.8(a) shows a voltage sag beginning from the 3rd cycle of a sinusoidal wave. The high-frequency detail of WT at the second-scale is illustrated in Fig. 7.8(b). In this case, it is difficult to distinguish between the disturbance signals and noise. However, the sag disturbance period can be easily detected using the MMG combining the MMF as revealed in Fig. 7.8(c). Compared with the WT, it can be seen that the proposed morphological transform has a greater ability in detecting the disturbance in a noisy environment.

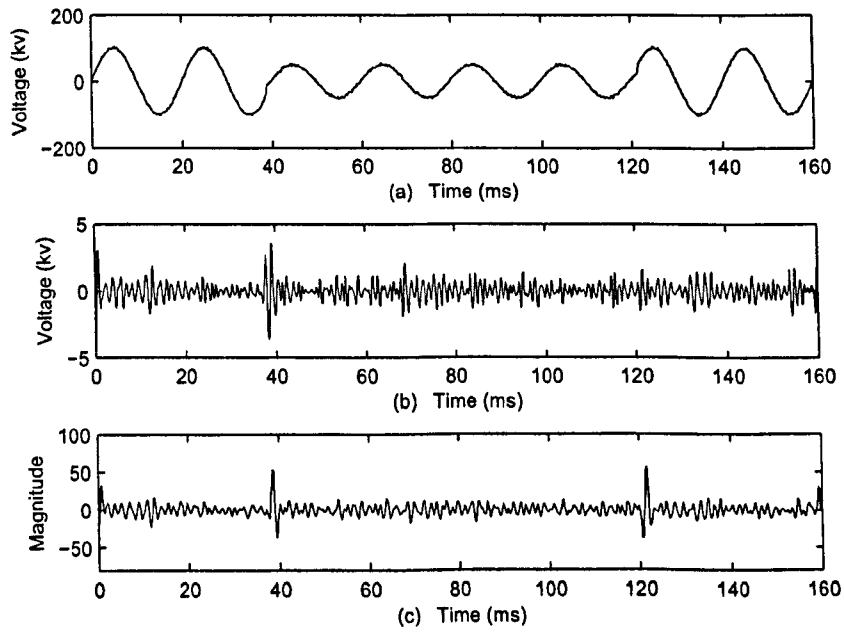

Figure 7.8: Analysis results compared with the WT method
a) Fundamental with a voltage sag; b) Result of the second-scale WT coefficients; c) Result of morphological transform for detection of the voltage sag period.

7.4.7 Classification of power disturbances

Many artificial intelligence-based algorithms were proposed for the classification of power quality disturbances. Some of the algorithms make use of neural networks [132] and expert systems [133]. Merged with different detection approaches, they can provide satisfactory classification results. However, all of these techniques rely on massive data for training, which greatly limits their practical applications.

In this chapter, the classification of disturbances can be undertaken based on feature extraction using the MMG. The classification process is depicted in Fig. 7.9, in which the six disturbances are firstly classified into two classes according to the variation of the magnitudes of fundamental voltage, and then the disturbances in each class are distinguished considering the extracted features

and the polarities of voltage magnitude variations.

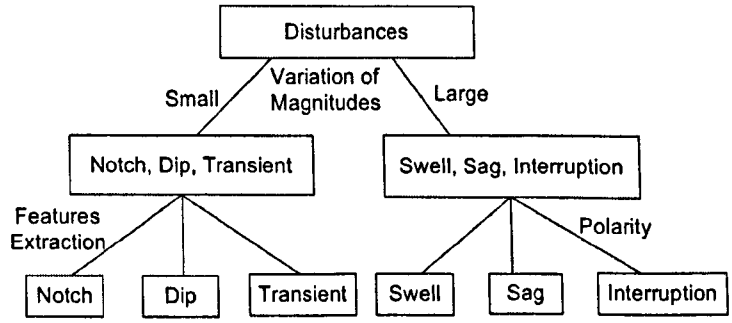

Figure 7.9: The process of disturbance classification.

First of all, for all the disturbances obtained from the simulation results presented in subsections 7.4.1 to 7.4.6, the feature extraction indicates the time instants at which the disturbances start, thus the magnitudes of the fundamental voltage can be calculated using DFT. The variations of the magnitudes are shown in Fig. 7.10. In order to classify the disturbances, the ranges of the voltage magnitude variations are calculated. Let V_n be the magnitude of the voltage prior to the disturbances, and V_d be the maximum or minimum magnitude during the period of disturbances, the range of the voltage magnitude variations can be calculated as:

$$\%\text{range} = \frac{V_d - V_n}{V_n} \times 100. \tag{7.4.1}$$

For each case of the disturbances, the corresponding range is calculated and listed in Table 7.1. The disturbances which have a large range value of their voltage magnitude variations, such as voltage swell, sag and momentary interruption, are classified to the first class. The disturbances which have a small range value is classified into the second class.

The ranges of voltage magnitude variations, for the interruption, swell and sag, are estimated to around -99.5%, 50.2% and -49.8%, respectively. The polarities observed in Fig. 7.10 are different, which are associated with voltage swell, sag and interruption respectively. The negative value represents a voltage sag occurring; while the positive denotes a voltage swell. For the case in which

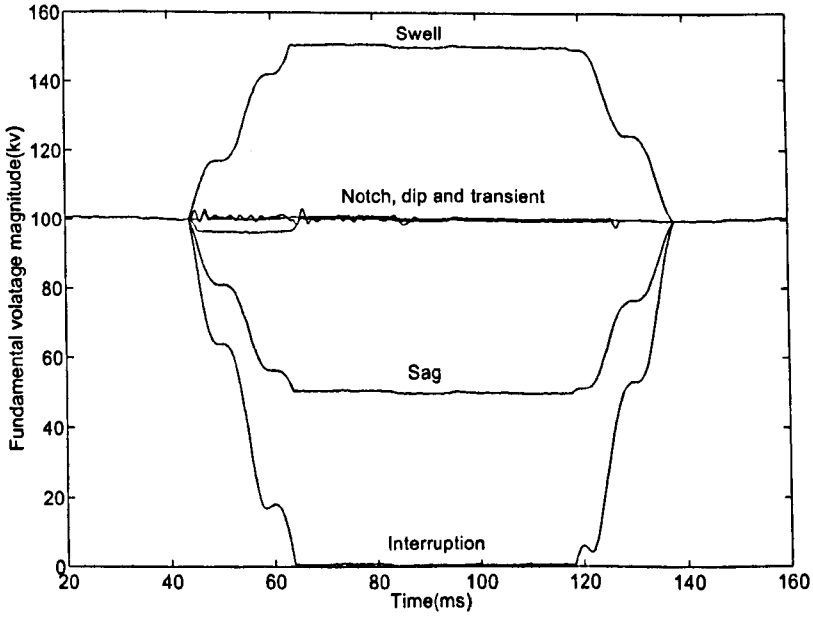

Figure 7.10: Voltage magnitude of the original signal.

the range is -99.5%, the values of voltage magnitudes are decreased to be a value almost 0 after the disturbance occurs. This case is recognised as a voltage momentary interruption.

In order to classify the disturbances in the second class, the features extracted in Cases A, B and E in subsections 7.4.1, 7.4.2 and 7.4.5 have been used. The magnitude and frequency can be calculated based on the features extracted by MMG, which are given in Figs. 7.3(c), 7.4(c) and 7.7(c) respectively.

The magnitudes of the disturbances are estimated by calculating the Root Mean Square (RMS) value of the voltage, which is:

$$V_{\text{rms}}(t_{n_0}) = \sqrt{\frac{1}{N}\sum_{n=n_0}^{n_0+N-1} V^2(t_n)}, \tag{7.4.2}$$

where $V_{\text{rms}}(t_{n_0})$ is a function of time. The data used to calculate the RMS values should cover the whole period of the disturbances which are indicated

Table 7.1: The classification of power disturbances based on the variation of voltage magnitudes

Disturbance	Range	Class
Dip	-3.4%	2nd
Notch	2.8%	2nd
Interruption	-99.5%	1st
Swell	50.2%	1st
Transients	2.6%	2nd
Sag	-49.8%	1st

Table 7.2: The properties of the features extracted by MMG

	Time	Frequency	Crest	Trough	RMS
Dip	1.2 ms	833.3 Hz	1	1	101.9 kV
Notch	2.0 ms	500.0 Hz	2	1	150.6 kV
Transients	5.0 ms	500.0 Hz	2	3	151.2 kV
	10.0 ms	500.0 Hz	5	5	136.9 kV
	10.0 ms	250.0 Hz	2	3	27.5 kv

in the features extracted by MMG. The calculation results and other properties for the extracted features are listed in Table 7.2.

The wave trough shown in Fig. 7.3(c) indicates a voltage reduction in the waveform and the following crest denotes a voltage increase. It means that the disturbance starts with a reduction and ends with an increase. Moreover, the corresponding points, the trough and crest in Fig. 7.3(c), have almost the same absolute value. Based on Fig. 7.3(c), the time duration, frequency and RMS values of the dip may be estimated and calculated as indicated in Table 7.2.

Each notch period in Fig. 7.4(a) corresponds to two crests and one trough in Fig. 7.4(c), whose values are different. The absolute value of the trough is larger than the crest. From this information it can be recognised that in

the period of disturbance, there are a rise, a large decent and another rise occurring in sequence. Obviously, a notch may be recognised based on such information. Furthermore, it is possible to estimate the amplitude of the notch by calculating its RMS value and the time and frequency also can be obtained from Fig. 7.4(c). The results are shown in Table 7.2.

A sequence of crests and troughs shown in Fig. 7.7(c) make this easily distinguishable from other transients. Three different sections could be identified according to the values of crests and troughs. The values of the time duration, frequency and RMS have been calculated and are given in Table 7.2 respectively.

7.5 Empirical Mode Decomposition for power quality monitoring

Power quality plays a major part in assessing the reliability of a power system. Thus if the reliability is to be optimised it is necessary to have quantitative information about disturbances. A power quality problem can best be described as any variation in the electrical power service, such as voltage dips and fluctuations, momentary interruptions, harmonics and transients, which result in mal-operation or failure of the end-user's equipment [134]. Such variations degrade the performance and efficiency of customers' loads and are of increasing concern to utilities and industry. They may also be reflected in high costs [115][116]. Therefore, an efficient method of monitoring these variations is valuable for both the utilities and consumers.

In order to improve the power quality, voltage or current waveforms may be recorded continuously using power monitoring instruments that generate time series of sampled data [135]. The monitoring requirement depends on the type of power quality problem. Some problems require monitoring for several months and others for several hours.

Disturbance analysers have been developed specifically for power quality measurements. They typically measure a wide variety of system disturbances

from very short duration transient voltages to long variations, outages or under-voltages. Conventional analysers summarise events with specific information such as over/under-voltage magnitudes, sags/surge magnitude and duration, transient magnitude and duration, *etc.* Graphics-based analysers save and print the actual waveform along with the descriptive information, which would be generated, by one of the conventional analysers.

However, it is often difficult to use these devices to classify the type of the disturbance or transient from the available information. Therefore, graphics analysers must be used with the conventional one. Disturbance analysers have very limited harmonic analysis capabilities. Traditional signal processing methods have been applied for monitoring power quality. The Short-Time discrete Fourier Transform (STFT) [136] is most often used to monitor electric power quality as a harmonic analyser. This transform has been successfully used for stationary signals where the properties of signals do not change over time. For non-stationary signals, the STFT cannot be successfully used to properly analyse the characteristics of signals.

Many new signal processing methods have been proposed in recent years. To analyse non-linear and non-stationary signals, a new method, called EMD [137, 138, 139], is introduced in this chapter, as a powerful multi-resolution signal decomposition technique for monitoring power quality. This new method is intuitive, and the basis of extracting signal components used in this method, is generated directly using a posteriori and adaptive decomposition method. Contrary to most of the previous methods, this decomposition method is adaptive and highly efficient. It is able to detect and localise transient signals, in time scale, by generating a collection of intrinsic mode functions. The EMD can be applied to detect the features of electric power disturbances.

7.5.1 Empirical Mode Decomposition and Hilbert transform

Many existing methods analyse signals simultaneously in the time and frequency domain, such as Wavelets and short-time Fourier transform. These

methods are based on the expansion of the signal into a set of basis functions defined by the method. EMD is a method of decomposing a signal in the time domain. The decomposition is based on the direct extraction of the signal energy associated with various intrinsic modes in different time scales and the most important parameters of the signal components.

The principle of this method is to adaptively decompose a given signal into a collection of oscillating components, called Intrinsic Mode Functions (IMFs), by a sifting procedure. Therefore, the signal can be regarded as an expansion of the sampled signal data in terms of the IMFs.

The essence of EMD is to identify the IMFs which are decomposed in time scales and defined locally by a time lapse between two extrema of an oscillatory signal or between two zero crossings of the signal. In some sense, the method can be regarded as a type of adaptive filtering. A signal is no longer decomposed in fixed overlapping frequency sub-bands but decomposed in time-varying sub-bands. The process is useful for analysing non-linear and non-stationary signals.

An IMF is a function that satisfies the following two conditions: (1) the number of extrema and the number of zero crossing in a whole sampled data set must either equal or differ at most by one; (2) at any point, the mean value of the envelope defined by the local maxima and the envelope defined by the local minima is zero. An IMF represents a simple oscillatory mode as a counter part of the simple harmonic function, but it allows the modulation of amplitude and frequency. Therefore it is much more generic than other signal processing methods.

IMF represents the oscillation mode imbedded in the data. In each cycle, IMF is defined by the zero crossings, involves only one mode of oscillation, and no complex riding waves are allowed. With the definition, an IMF is not restricted to a marrow band signal, and it can be both amplitude and frequency modulated. In fact, it can be non-stationary. Therefore, purely frequency or amplitude modulated functions can be IMFs even though they have finite bandwidth according to the traditional definition.

With the definition of IMF, any signal can be simply decomposed by its local maxima and minima. Once the extrema of the signal are identified, all the local maxima can be connected by a cubic spline line as the upper envelope. Repeating the procedure, the local minima and the lower envelope can be obtained. All the data between the upper and lower envelopes should be covered. The mean of the upper and lower envelopes is designated as M_1, and the difference between the original data $X(t)$ and M_1 is the first component, H_1, *i.e.*,

$$X(t) - M_1(t) = H_1(t). \tag{7.5.1}$$

Ideally, H_1 should be an IMF since the construction of H_1 described above should have made it satisfy all the requirements of IMF. In reality, however, overshoots and undershoots are common, which can also generate new extrema, and shift or exaggerate the existing ones. If H_1 does not meet the definition of a true IMF, the sifting process has to be repeated many times to correct this until the extracted signal is reduced as an IMF. In the following sifting process, H_1 is treated as the processing data. Then

$$H_1(t) - M_{11}(t) = H_{11}(t), \tag{7.5.2}$$

where M_{11} is the mean of upper and lower cubic spines fitting to maxima and minima of the signal H_1, and H_{11} is the subsequent trial IMF. The sifting process can repeat k times until H_{1k} is a true IMF, that is:

$$H_{1(k-1)}(t) - M_{1k}(t) = H_{1k}(t). \tag{7.5.3}$$

Then the first IMF component of the data can be designated as:

$$C_1(t) = H_{1k}(t). \tag{7.5.4}$$

C_1 should contain the finest scale or the shortest period component of the signal. C_1 can be separated from the rest of the data by:

$$X(t) - C_1 = R_1. \tag{7.5.5}$$

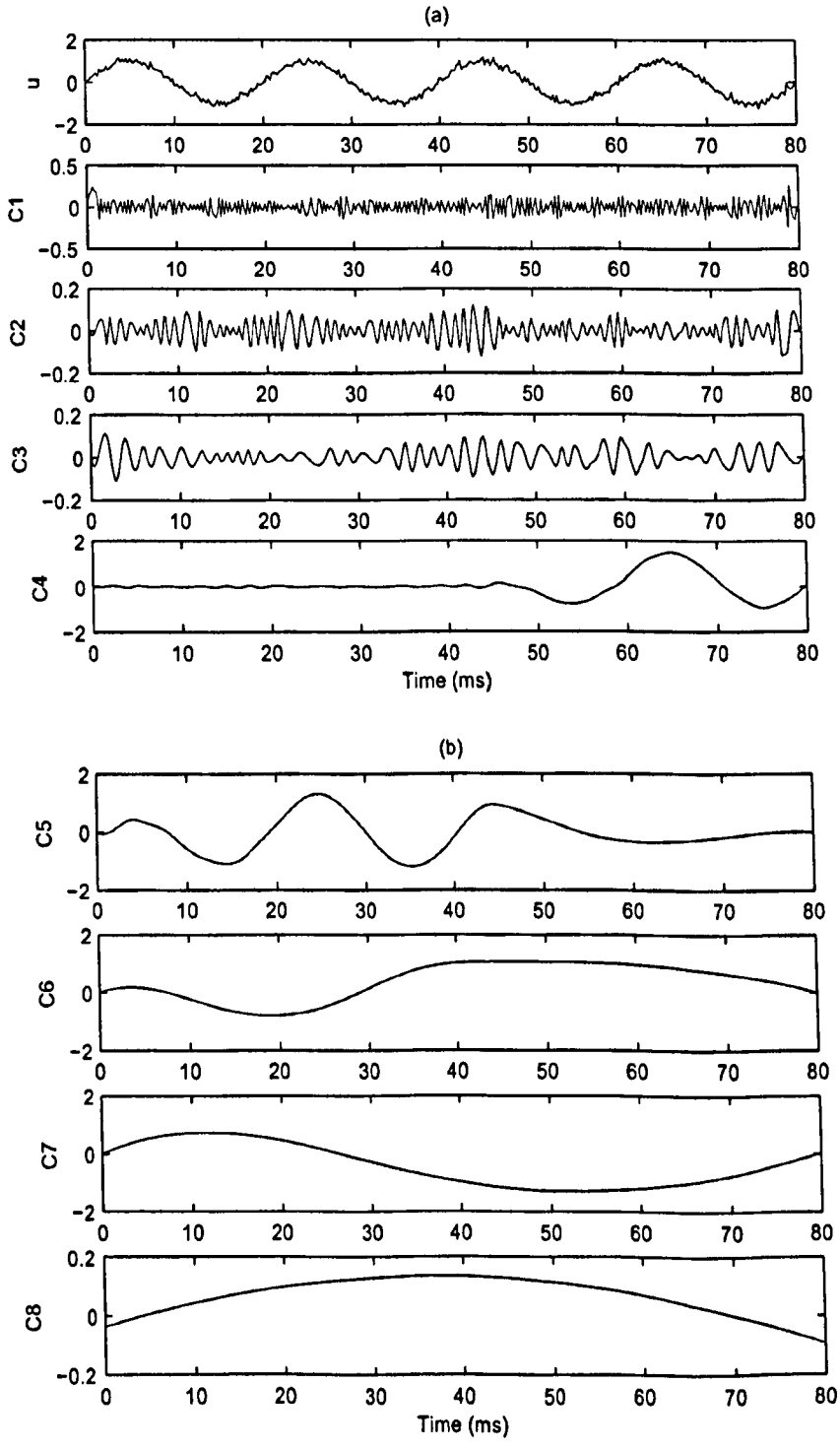

Figure 7.11: The resulting EMD components from the power data: (a) the original data u and the components C_1-C_4; (b) the components C_5-C_9.

Since the residue still contains longer period components, it should be treated as the new data and subjected to the same sifting process as described above. This procedure can repeat for all the subsequent R_js, and the result is

$$\begin{aligned} R_1(t) - C_2(t) &= R_2(t), \\ R_2(t) - C_3(t) &= R_3(t), \\ &\cdot \\ &\cdot \\ &\cdot \\ R_{n-1}(t) - C_n(t) &= R_n(t). \end{aligned} \tag{7.5.6}$$

The sifting process can be stopped by any of the following predetermined criteria: either when the component, C_n, or the residue, R_n, becomes less than the predetermined value of substantial consequence, or when the residue, R_n, becomes a monotonic function and no another IMF can be extracted from it.

By summing up (7.5.5) and (7.5.6), the original signal is represented in the following equation:

$$X(t) = \sum_{i=1}^{n} C_i + R_n. \tag{7.5.7}$$

which is decomposed into n-empirical modes, and a residue R_n, which can be either a monotonic function or a single cycle. When applying the EMD method, a mean or zero reference is not required; EMD only needs the locations of the local extrema. The sifting process generates the zero reference for each component, except for the residue. The components of the EMD are usually physically meaningful, for the characteristic scales are defined by the physical data themselves.

The sifting process can be illustrated by applying to a sinusoidal signal in power systems. In Fig. 7.11, u represents a voltage waveform and the IMFs $C_1 - C_8$ are components decomposed used the EMD method.

Unlike the frequency filtering methods that cause deformation to the original signal if it is either non-linear or non-stationary, a time-space filtering can be devised by reconstruction using the IMFs. The EMD filter can preserve

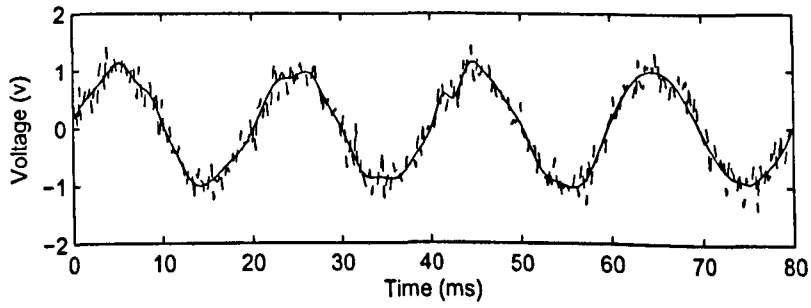

Figure 7.12: The result of reconstruction using a low-pass EMD filter: the dashed line is the original signal u; the real one is the signal after reconstruction.

the full non-linearity and non-stationarity in the physical space since both non-linear and non-stationary signal generate harmonics of all ranges. For example, low-pass filtered results of a signal having n IMF components can be expressed simply as:

$$X_{lk}(t) = \sum_{j=k}^{n} C_j(t) + R_n(t). \tag{7.5.8}$$

High-pass results can be expressed as:

$$X_{hk}(t) = \sum_{1}^{k} C_j(t), \tag{7.5.9}$$

and a bandpass result can be expressed as:

$$X_{bk}(t) = \sum_{b}^{k} C_j(t), \tag{7.5.10}$$

where b and k are the selected intermediate modal numbers. Band-cut filters may be designed simply by omitting selected components in the reconstruction progress. The advantage of this time-space filtering is that the results preserve the full non-linearity and non-stationarity in the physical space.

In Fig. 7.11, the noise contained in the signal u can be filtered by a low-pass filter using reconstruction of IMFs. Set $k = 2$ in (7.5.8), the result obtained by adding the components from C_3 to C_9 is shown in Fig. 7.12.

7.5.2 The Hilbert transform analysis

Once all the IMFs are found and since each IMF admits the "well-behaved" Hilbert Transform (HT), the time-dependent (instantaneous) phase angles, frequencies and amplitudes of each component can be readily obtained utilising the HT.

For a given data, $C(t)$, its HT is defined as:

$$Y(t) = \frac{1}{\pi} P \int_{-\infty}^{\infty} \frac{C(t')}{t - t'} dt', \tag{7.5.11}$$

where P indicates the Cauchy principle value. With the definition, $C(t)$ and $Y(t)$ can be combined to give an analytical complex signal as:

$$Z(t) = C(t) + jY(t) = a(t)e^{j\theta(t)}, \tag{7.5.12}$$

in which the amplitude, $a(t)$, and phase $\theta(t)$ of the signal is given by:

$$a(t) = \sqrt{C^2(t) + Y^2(t)}, \tag{7.5.13}$$

$$\theta(t) = \tan^{-1} \frac{Y(t)}{C(t)}. \tag{7.5.14}$$

Equation (7.5.12) is just a polar representation of $C(t)$, in terms of time-varying amplitude and phase. Its instantaneous frequency can be defined as:

$$\omega(t) = \frac{\mathrm{d}\theta(t)}{\mathrm{d}t}. \tag{7.5.15}$$

By applying the HT to calculate a meaningful instantaneous frequency for each component, the original data $X(t)$ can be expressed as:

$$X(t, w) = \sum_{j=1}^{n} a_j(t) \exp(i \int w_j(t) dt), \tag{7.5.16}$$

where a_j is a time-dependent expansion coefficient and the argument of the exponential w_j is the instantaneous frequency of each component as a function of time, respectively, and the residue, R_n, is omitted. Comparing the equation with the Fourier transform, the IMF represents a more general expansion with variable amplitude and the instantaneous frequencies. This not only greatly

improves the efficiency, but also makes it able to accommodate non-linear and non-stationary signals.

The HT of the IMFS has the advantage of proving a physical interpretation of what it is accomplishing. The essence of the EMD is to first identify the appropriate time scales that will reveal the physical characteristics of the studied system and then to decompose the data accordingly. The decomposition for a for a given set of data is based on direct extraction of the energies associated with various time scales and can be viewed as an expansion of the data in terms of the corresponding IMFs, which are derived from the data.

Contrary to almost all the previous methods, the EMD decomposition is intuitive, direct and simple. It generates IMFs through an adaptive algorithm where the basis of decomposition is derived from the data. The original data can be completely reconstructed by summing up the IMF components and the residual trend. The instantaneous frequency obtained by applying the HT to the functions derived by EMD, is very localised in the time-frequency domain and reveals important characteristics of the signal. Therefore, it is possible to detect the changing frequencies of components, which provides a more precise time-frequency representation of signal data than the Fourier-based methods.

The EMD is wholly different from other methods because the result produced by the HHT is the only one that is adaptive without a priori assumption imposed, as in Fourier-based methods. Since it preserves intrinsic properties of data on the time-scale, it offers a microscopic view of data that is more accurate and representable of the original data. It operates and yields physically meaningful results in a real time scale. Ideally, each component has a physical meaning. Therefore, it provides quantitative measurements that enhance understanding of underlying phenomena.

7.6 Monitoring of power quality events

As mentioned, power quality events comprise various kinds of electrical disturbances such as voltage sags, voltage swells, harmonic distortions, flickers,

imbalances, oscillatory transients and momentary interruptions, *etc* [134]. The EMD method can be applied to detect, localise and estimate the features of such electrical disturbances.

In order to verify the method applicability to power quality monitoring, various disturbances have been considered and simulated numerically, added up to the fundamental and extracted successively using the EMD method. The whole signal has been corrupted by white noise in an opportune number of simulations. The sampling frequency used here is always 5 kHz, and the number of SNR value for each case is of about 26.

7.6.1 Case A: periodical notch

Figure 7.13(a) reports the case of a fundamental sinusoid ($2V_{pp}$-50 Hz) affected by a periodical high-frequency sinusoidal notch ($\Delta T = 2$ ms, $A = 1V_{pp}$). Figures 7.13(b)-(d) show the IMF components C_1, C_2 and C_3 respectively extracted using the EMD method. The disturbance extracted from the fundamental by reconstructing the components C_1 to C_3 is illustrated in Fig. 7.14(b). The notch period time can easily be estimated in this figure.

The original notch plus the noise are also illustrated in Fig. 7.14(a) for the comparison with the extracted results. The similar pattern of the results indicates the validity of the proposed method. Other tests have been carried out by varying the notch frequency, amplitude and shape and the same trend of the discussed case has been obtained.

7.6.2 Case B: voltage dip

A classical example of voltage dip, with duration $\Delta T = 1.4$ ms and amplitude $A = 1$ V superimposed on the same fundamental of the case of periodical notch, is represented in Fig. 7.15(a). The figure shows the voltage dip affecting the fundamental has been extracted into a series of IMF components using the EMD method. The dip can be properly reconstructed by adding up the IMF components C_1, C_2 and C_3 which are illustrated in Fig. 7.16(b). Compared

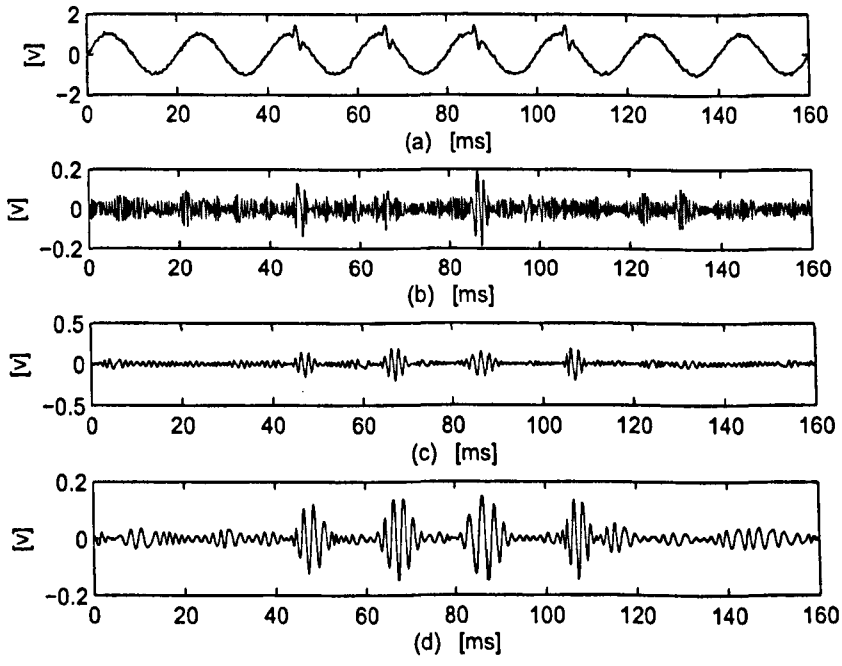

Figure 7.13: a) Fundamental with a periodical sinusoidal notch; b) IMF component C_1; c) IMF component C_2; d) IMF component C_3.

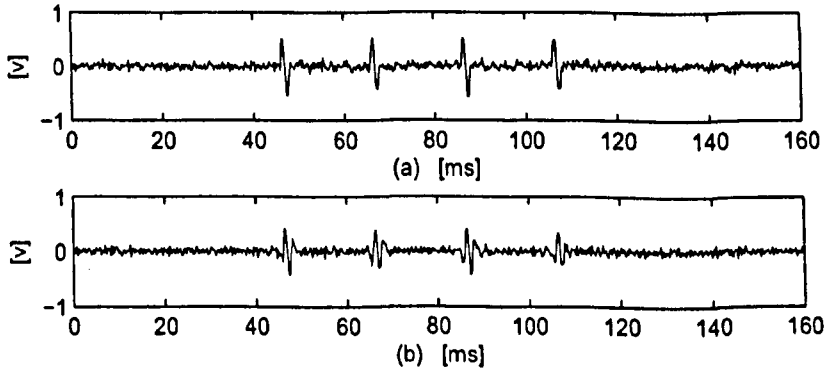

Figure 7.14: Comparison of the extracted results with the original disturbance. a) sum of the noise and the periodical notch; b) the periodical notch obtained by adding C_1, C_2 and C_3.

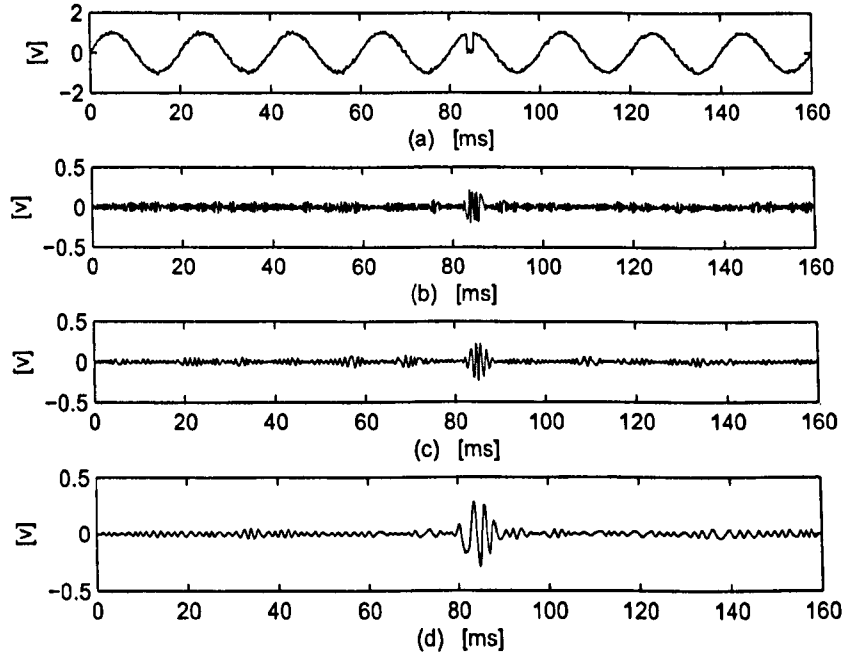

Figure 7.15: a) Fundamental with a voltage dip; b) IMF component C_1; c) IMF component C_2; d) IMF component C_3.

with the original dip adding with the noise showing in Fig. 7.16(a), the extracted dip is symmetrical to the time axis and has half amplitudes, $A = 0.5$ V, at both sides. It can be regarded as a DC shift of the original dip. Other tests have been carried out, varying the duration and amplitude of the voltage dip; similar results are obtained for these tests.

7.6.3 Case C: oscillatory transients

An example of an oscillatory transient with period $\Delta T = 25$ ms and amplitude $A = 1$ V (0.6, 0.4) is superimposed on the same fundamental voltage as showing in Fig. 7.17(a). By applying the EMD method, the signal can be decomposed into IMF components. Figure 7.18(b) is the result of the disturbance affecting the fundamental reconstructed by the selected IMF components: C_1, C_2 and C_3. In contrast with Fig. 7.18(a) which shows the original oscillatory transients, the similar extracted results obtained by the EMD method

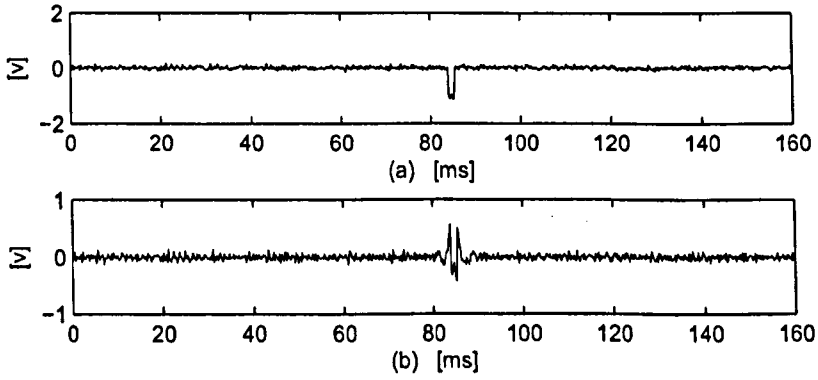

Figure 7.16: Comparison of the extracted results with the original disturbance. a) sum of the noise and the voltage dip; b) dip extracted from the fundamental and obtained by adding up C_1, C_2 and C_3.

indicates the applicability of proposed method. Other tests have been carried out by varying the oscillatory transient frequency ($1/\Delta T$) and amplitude. The same trend of the discussed case has been obtained.

7.7 Summary

The morphological transform method combining the MMF with MMG has been proposed to extract the features of various power disturbances. The extracted features may be used to classify different disturbances. The simulation studies have demonstrated that the proposed method is capable of detecting, localising and classifying different types of power disturbances. The main characteristics of the proposed method, in comparison with Fourier transform and WT, are:

(1) The basic disturbances in electrical power systems can be detected and localised even in a noisy environment;

(2) The features extracted by the proposed method can be used to classify various disturbances;

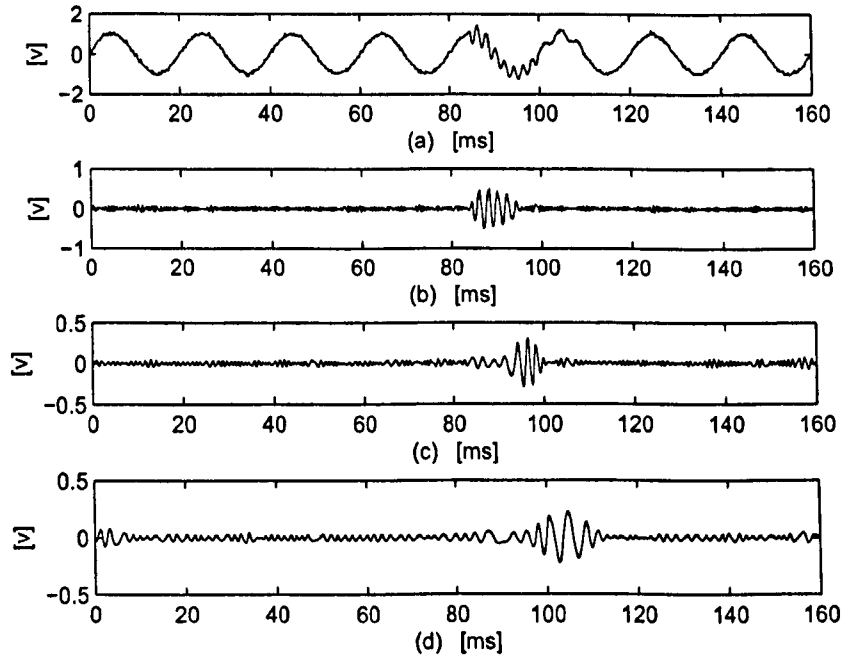

Figure 7.17: a) Fundamental with an oscillatory transient; b) IMF component C_1; c) IMF component C_2; d) IMF component C_3.

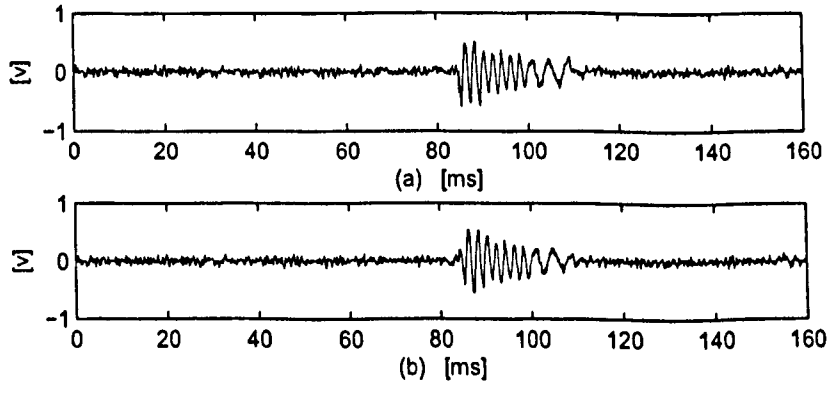

Figure 7.18: Comparison of the extracted results with the original disturbance. a) sum of the noise and the oscillatory transient; b) oscillatory transient extracted from the fundamental and obtained by adding up C_1, C_2, C_3.

(3) The proposed method has capability of fast calculation which involves only addition, subtraction and comparison operations and it is able to be implemented in real time for analysis of power disturbances.

Furthermore, A new method named EMD has been proposed in this chapter for power quality monitoring and assessment. It is based on the multi-resolution signal decomposition and reconstruction and offers as a powerful means for analysis of non-linear and non-stationary data. The properties of multi-resolution signal decomposition shows the ability of the technique to extract important features from distorted transient signals of power disturbances. Several types of power disturbances have been considered in the simulation study and they are analysed and discussed in detail to evaluate the EMD. The results show that the EMD method is able to provide accurate monitoring and assessment on the degree and characteristics of power disturbances.

Chapter 8

Power System Harmonic Estimation Using a Morphological Filter

This chapter presents a new method based on MM for accurate estimation of harmonics and detection of inter-harmonics or sub-harmonics in power systems. This method, using a morphological transform as a low-pass filter, is developed based on a well-known technique: instantaneous reactive power theory. The simulation results are presented to show the accuracy and capability of the proposed method. The extraction of a sub-harmonic component, from ferroresonant voltage of a power transformer, is also discussed as an example of the inter-harmonic detection. The calculation simplicity of the morphological operators furnishes the proposed method with ease of real-time implementation.

8.1 Introduction

With a wide range of power electronics-related applications in power systems, harmonic currents are increasing at an alarming rate which has greatly deteriorated the power quality in electrical power networks [140]. Moreover,

some of electronic controlled equipments used in power systems, such as cyclo-convertors, produce sub-harmonics [141], a type of waveform distortion that can severely degrade the power system performance. Therefore, it is desired to develop methods of estimating the harmonic currents, based on selected measurements of power systems.

The Fast Fourier Transform (FFT) has been applied to analyse harmonic currents for a long time [142]. In recent years, a growing interest has been placed to sub-harmonics and inter-harmonics by electrical power engineers investigating the current and voltage waveform distortion in power systems. It has been shown that great difficulties arise in the sub-harmonic or inter-harmonic detection and measurement, with acceptable levels of accuracy, due to the spectral leakage and resolution limit of FFT. FFT cannot accurately analyse waveforms containing inter-harmonics because the synchronisation of the sampling procedure to inter-harmonics is practically infeasible. The detection of inter-harmonics requires an approach different from that used for harmonic analysis.

It has been testified that the approach of active power filter, based on instantaneous reactive power theory, is one of the most successful methods for detection and compensation of harmonic currents as well as sub-harmonics and inter-harmonics [143, 144, 145]. The accuracy of this approach mainly depends on the design of the low-pass filter, which can be implemented with an analog or digital filter. The analog low-pass filters used in the detection system result in large errors in the reference current because of the spectral leakage [146]. Their credibility and accuracy would become suspect over time.

A digital low-pass filer is based on either Infinite Impulse Response (IIR) or Finite Impulse Response (FIR) filter, which does not suffer from these shortcomings. However, IIR filters require a feedback loop to calculate the output value and the rounding off in the computation may hamper their accuracy [147]. An FIR filter does not have a feedback loop, but it ought to achieve the sufficient accuracy in a high order because of its worse roll-off characteristics. Although a high-order filter with a high-order cutoff frequency can increase the

calculation accuracy to a certain extent, it will also increase the computational burden.

In this chapter, a morphological filter, based on instantaneous reactive power theory, is proposed for the estimation of harmonic currents and detection of inter-harmonics. The proposed filter is used to minimise the spectral leakage effect and reduce the errors in measuring the harmonics. The simple calculation of morphological filter is one of major merits, which makes this method not only meet the requirements of accuracy for detection of harmonics for compensation purpose, but also suitable for real-time implementation. Simulation studies, with an example of extracting the sub-harmonics from a ferroresonant voltage, have been conducted to verify the proposed filter. The simulation results show that the greater accuracy can be achieved with the new method in comparison with conventional techniques.

8.2 Sub-harmonics and inter-harmonics

Harmonics are spectral components at frequencies that are integer multiple of the system fundamental frequency. Inter-harmonics are spectral components at frequencies that are not integer multiple of the system fundamental frequency. Sub-harmonics are inter-harmonics with frequencies lower than system fundamental frequency.

Sub-harmonic currents are generated by modern loads such as cyclo-converters, arc furnaces and integral cycle controlled furnaces or any type of pulse-burst-modulation power conditioned loads, *i.e.*, forges, drop hammers, stamping tools, saws, compressors and reciprocating pumps. Wind generators, adjustable speed drives and automated spot-welders are also the sources of sub-harmonic currents generators.

The voltage sub-harmonics, even with small amplitudes superimposed to the fundamental will cause lighting system flicker or display and monitor image fluctuations. It is also responsible for saturation of power and measurement transformers, AC motor aging, torque oscillations in turbogenerators and

erroneous firing of thyristor apparatus, malfunctioning of remote control system and erroneous behaviour of instrumentation based on Phase Locked Loop (PLL).

International standard are fixing limits for inter-harmonics, which gives high importance to inter-harmonic monitoring. IEC Standard 61000-4-7 [148] introduces definitions and signal processing recommendations for harmonic and inter-harmonic measurement. The presence of inter-harmonic and sub-harmonic components strongly increase the difficulties in both modelling and measuring the distorted waveforms. This is mainly due to the variability of the frequencies and amplitudes of inter-harmonics or sub-harmonics, and a great sensitively to the spectral leakage phenomenon.

8.3 Instantaneous reactive power theory

The instantaneous reactive power theory was formulated at the beginning of the 1980s [143], which has suffered the largest diffusion along these years. It is most used as control strategy for the active power filter. This theory is based on a coordinates transformation from the phase reference system *abc* to the $0\alpha\beta$ system.

At time t, 3-phase instantaneous currents, i_a, i_b, i_c, in a 3-phase 3-wire power distribution system can be expressed as:

$$\begin{aligned} i_a(t) &= \sqrt{2}\sum_{i=1}^{\infty}[I_k \sin(k\omega t + \varphi_k)], \\ i_b(t) &= \sqrt{2}\sum_{k=1}^{\infty}[I_k \sin(k\omega t + \varphi_k - 120°)], \\ i_c(t) &= \sqrt{2}\sum_{k=1}^{\infty}[I_k \sin(k\omega t + \varphi_k - 240°)], \end{aligned} \tag{8.3.1}$$

where $\omega = 2\pi f$, $f = 50$ Hz, is the system frequency. I_k and φ_k are the amplitude and phase angle of the respective fundamental and harmonic currents respectively. The currents can be expressed in an instantaneous space vector

as:

$$i_{a,b,c} = \begin{bmatrix} i_a \\ i_b \\ i_c \end{bmatrix}. \tag{8.3.2}$$

The 3-phase current vector $i_{a,b,c}$ is transformed into an $\alpha - \beta - 0$ coordinate using the following operations:

$$C_{32} = \sqrt{\frac{2}{3}} \begin{bmatrix} 1 & -1/2 & -1/2 \\ 0 & \sqrt{3}/2 & -\sqrt{3}/2 \end{bmatrix}, \tag{8.3.3}$$

$$i_{\alpha,\beta} = C_{32} \begin{bmatrix} i_a \\ i_b \\ i_c \end{bmatrix} = \begin{bmatrix} i_\alpha \\ i_\beta \end{bmatrix}, \tag{8.3.4}$$

$$\begin{bmatrix} i_\alpha(t) \\ i_\beta(t) \end{bmatrix} = \begin{bmatrix} \sqrt{3} \sum_{k=1}^{\infty} [I_k \sin\varphi_k \cos(k\omega t) + I_k \cos\varphi_k \sin(k\omega t)] \\ \sqrt{3} \sum_{k=1}^{\infty} [I_k \sin\varphi_k \sin(k\omega t) - I_k \cos\varphi_k \cos(k\omega t)] \end{bmatrix} \tag{8.3.5}$$

The instantaneous active and reactive power of the k'th-order harmonic component can be obtained as:

$$\begin{bmatrix} i_{k'p}(t) \\ i_{k'q}(t) \end{bmatrix} = C \begin{bmatrix} i_\alpha(t) \\ i_\beta(t) \end{bmatrix} = \begin{bmatrix} \bar{i}_{k'p} \\ \bar{i}_{k'q} \end{bmatrix} + \begin{bmatrix} \tilde{i}_{k'p}(t) \\ \tilde{i}_{k'q}(t) \end{bmatrix}, \tag{8.3.6}$$

$$C = \begin{bmatrix} \sin(k'\omega t) & -\cos(k'\omega t) \\ -\cos(k'\omega t) & -\sin(k'\omega t) \end{bmatrix}, \tag{8.3.7}$$

$$\begin{bmatrix} \bar{i}_{k'p} \\ \bar{i}_{k'q} \end{bmatrix} = \begin{bmatrix} \sqrt{3} I_{k'} \cos\varphi_{k'} \\ -\sqrt{3} I_{k'} \sin\varphi_{k'} \end{bmatrix}, \quad k = k', \tag{8.3.8}$$

$$\begin{bmatrix} \tilde{i}_{k'p}(t) \\ \tilde{i}_{k'q}(t) \end{bmatrix} = \sqrt{3} \begin{bmatrix} \sum_{k=1}^{\infty} I_k \cos[(k-k')\omega t + \varphi_{k'}] \\ -\sum_{k=1}^{\infty} I_k \sin[(k-k')\omega t + \varphi_{k'}] \end{bmatrix} \quad k \neq k'. \tag{8.3.9}$$

Using a synchronous detector C shown in (8.3.7) with a frequency of k' times of fundamental, the specific kth ($k = k'$) harmonic component can be measured. The result is separated into two parts by the detection process as shown in (8.3.6). The first part is a constant while the other is a time-variant component. If the frequency of the synchronous detector matches the kth-order harmonic frequency of the signal, the first component would represent the magnitude of the kth harmonic component as shown in (8.3.8). Since the signal is not just composed of this kth harmonic component, the second part would be non-zero as shown in (8.3.9). This component can be considered as a spectral leakage effect. To ensure the accuracy of the measurement of the constant current component, it is needed to eliminate the oscillating ripples of the second component by a low-pass filter.

Using an ideal low-pass filter, the constant component can be accurately obtained. Then the kth harmonic current could be reconstructed as follows:

$$\begin{bmatrix} i_{ka}(t) \\ i_{kb}(t) \\ i_{kc}(t) \end{bmatrix} = C_{23}C^{-1} \begin{bmatrix} \bar{i}_{kp} \\ \bar{i}_{kq} \end{bmatrix}$$

$$= \begin{bmatrix} \sqrt{2}I_k \sin(k\omega t + \varphi_k) \\ \sqrt{2}I_k \sin(k\omega t + \varphi_k - 120°) \\ \sqrt{2}I_k \sin(k\omega t + \varphi_k - 240°) \end{bmatrix}, \tag{8.3.10}$$

where

$$C_{23} = \sqrt{\frac{2}{3}} \begin{bmatrix} 1 & 0 \\ -1/2 & -\sqrt{3}/2 \\ -1/2 & \sqrt{3}/2 \end{bmatrix}. \tag{8.3.11}$$

The calculated harmonic components in the $\alpha - \beta - 0$ coordinate are converted back to the $a - b - c$ coordinate using the transformation of $C_{23}C^{-1}$. With the integral harmonics extracted, the inter-harmonic or sub-harmonic components are detected by subtracting all the integral harmonics from the original signal.

The above instantaneous reactive power theory is limited to multi-phase circuits. The instantaneous values of three-phase currents are needed to estimate the harmonic currents if this theory is used. However, in a single-phase

situation, we can conceive the values of the other two-phases using one-phase current [149]. The other two-phase currents can be obtained by lagging the phase values for 120° and 240° respectively. For an example, to extract the nth harmonic current, the other two-phase currents are built by time lags and the total three-phase currents are denoted as:

$$\begin{bmatrix} \sqrt{2}\sum_{k=1}^{\infty}[I_k \sin(k\omega t + \varphi_k)] \\ \sqrt{2}\sum_{k=1}^{\infty}[I_k \sin(k\omega(t - 120°/n) + \varphi_k)] \\ \sqrt{2}\sum_{k=1}^{\infty}[I_k \sin(k\omega(t - 240°/n) + \varphi_k)] \end{bmatrix}. \tag{8.3.12}$$

8.4 A low-pass morphological filter

Morphological operators are set transformations which are very efficient for ameliorating the quality of signals or for extracting some of their features. If appropriately used, they can process signals and preserve their intrinsic characteristics.

Morphological filters have been widely used in many signal and image processing applications, due to their simple operation and robust performance. Different morphological filters can be constructed by the different combinations of morphological operators. A morphological filter is an operator on a complete lattice that is increasing and idempotent. Two well-known classes of morphological filters are opening and closing. They can be used to compose a class of alternative sequential filters [40].

Two alternative sequential filters are the open-closing filter and close-opening filter which are realised through cascade connection of the opening and closing transform in different order. There is a statistical deviation problem existing in the open-closing filter and closing-opening filter due to the expansibility of the opening transform and the inverse expansibility of the closing transform. So the output of the open-closing filter is small, while that of the close-opening filter is large. Under most circumstances, in order to lower the output deviation and achieve the best performance, the two filters can be cascaded to form

a new combined filter, the average of open-closing and close-opening. Its iterative repetition can be employed to construct a low-pass filter. Let y_j represents the output of the filter at level j and g_j is an SE at level j, the filter process is described as:

$$\begin{aligned} y_j &= [(y_{j-1} \circ g_{j-1}) \bullet g_{j-1} \\ &\quad +(y_{j-1} \bullet g_{j-1}) \circ g_{j-1}]/2. \end{aligned} \tag{8.4.1}$$

When $j = 1$, $y_0 = y$ is the input signal. The iteration will not stop until there is not a big difference between the outputs of the filter, y_n and y_{n-1} at level n and $n-1$ respectively, which can be represented as:

$$\left| \sum_t y_n(t) - \sum_t y_{n-1}(t) \right| < \delta, \tag{8.4.2}$$

where δ is a threshold to be set.

The DC component in the waveform can be extracted as the output of the filter. In fact, the SE acts as a filtering window to remove the high-frequency components. The accuracy and effectiveness of the morphological filter is depended on the shape and width of the SE. Usually the SE has a simple geometrical shape such as a triangle, round or line. Here, g_j is a flat line with a length of $j+2$ at level j, increased by one for each iteration.

Most parts of high frequency components will be filtered by this morphological low-pass filter. The result of the filtered signal is then convolved with a narrow Hamming window based FIR filter to reduce the errors in the measurement. As a result, the DC component of the reactive power in (8.3.7) can be obtained accurately.

8.5 Simulation results

8.5.1 Harmonic estimation

Simulation results presented in this section are all obtained from MATLAB and they show a fair comparison with other methods. In all simulation cases,

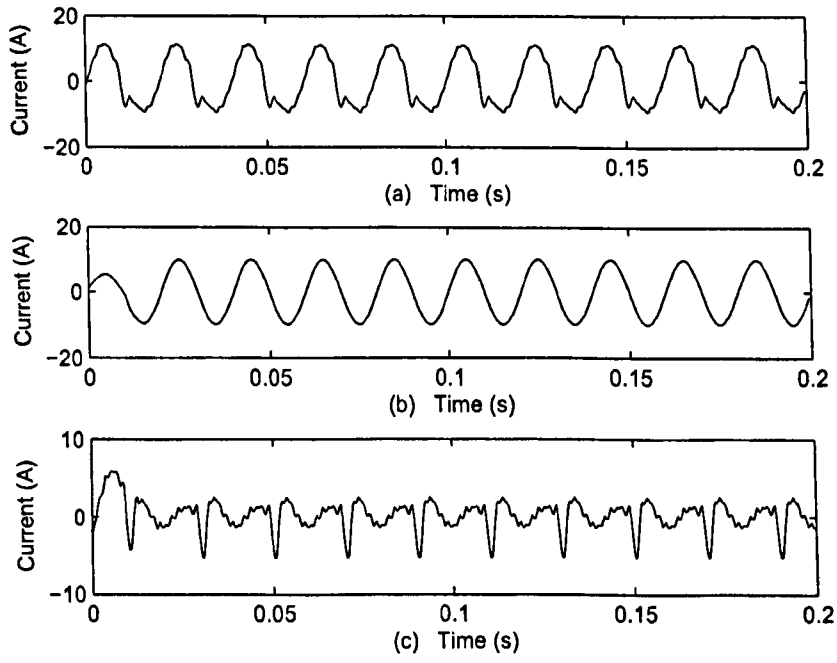

Figure 8.1: Extraction results using the proposed method. a) The pre-defined current signal with harmonic distortion; b) The extracted fundamental component; c) The residual harmonics.

the sampling frequency is 2.4 kHz, and the nominal frequency is assumed to be 50 Hz. A pre-defined signal is used to simulate a measured current. The signal is a typical current waveform with some harmonic contents. The magnitudes and phase angles of the harmonics are shown in Table 8.5.1, where I_j ($j = 1, 2, \cdots, 12$) denotes the jth-order harmonic component.

Table 8.1: The magnitudes and phase angles of current components

Current(A)	I_1	I_2	I_3	I_4	I_5	I_6	I_7	I_8	I_{12}
Magnitude	10.0	1.80	1.10	0.90	0.64	0.56	0.45	0.40	0.34
Phase	0	$-\pi/2$	$\pi/3$	$-\pi/4$	$\pi/5$	$-\pi/6$	$\pi/7$	$-\pi/8$	$\pi/12$

Figure 8.1(a) indicates the waveform of the pre-defined current signal. To extract the fundamental component, the instantaneous reactive power is trans-

formed through the proposed morphological low-pass filter. The fundamental component is extracted and reconstructed as shown in Fig. 8.1(b).

The residual harmonics are shown in Fig. 8.1(c). It is re-processed by the instantaneous reactive power transformation using the same morphological low-pass filter. All inter-harmonics can be obtained by repeating the extraction process. Figure 8.2(a) is the 2nd harmonic component obtained using the proposed method, while Fig. 8.2(b) and (c) illustrate the 4th and 6th harmonic components respectively. They are coincident with the values of the predefined current in Table 8.5.1. Based on the extracted results in these figures, it can be seen that the proposed method works effectively.

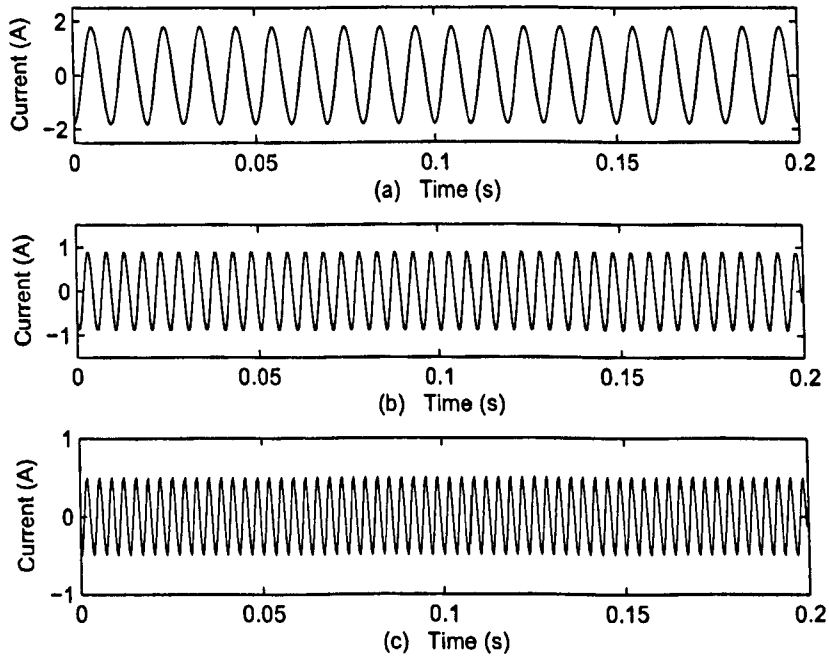

Figure 8.2: a) The 2nd harmonic current; b) The 4th harmonic current; c) The 6th harmonic current.

The proposed method is compared with other digital low-pass filters such as Butterworth IIR and wavelet filters respectively. A wavelet of the Daubechies 4 is selected to realise a low-pass filter to extract the constant values based on the instantaneous reactive power. The fundamental and harmonic components

Table 8.2: Comparison of the calculation results by three detection methods

Frequency	50	100	150	200	250	300	350	400	600
Standard	10.000	1.8000	1.1000	0.9000	0.6400	0.5600	0.4500	0.4000	0.3400
Wavelet	9.998	1.7770	1.0866	0.8825	0.6304	0.5068	0.4358	0.3962	0.3055
IIR	9.999	1.7997	1.0921	0.8998	0.6340	0.5080	0.4381	0.3994	0.3085
MF	10.000	1.8000	1.0937	0.9000	0.6363	0.5100	0.4398	0.4000	0.3096

obtained using three different methods, the wavelet, IIR and morphological filters are reported in Table 8.5.1. The results show that the IIR and wavelet low-pass filters cause a larger error, while the filtering accuracy of morphological low-pass filter is greatly improved.

8.5.2 Inter-harmonics and Sub-harmonics detection

The proposed method is also able to detect the sub-harmonic and inter-harmonic components. If a signal is distorted by some sub-harmonic or inter-harmonic components, it is difficult for the traditional method such as FFT to estimate it. In FFT process, the sampling is synchronised with the harmonics, undesirable asynchronous deviation to the sub-harmonics or inter-harmonics may exist. Consequently, possibly large leakage errors may occur.

Using the proposed method, the fundamental component in the signal can be extracted accurately, and the sub-harmonic will be manifested in the residual. Figure 8.3(a) is a signal constructed by a fundamental component with a sub-harmonic of 20 Hz. Using the morphological low-pass filter, the fundamental component is extracted as shown in Fig. 8.3(b). The residue in Fig. 8.3(c) is the sub-harmonic component detected. Another case is concerned with a signal which contains a sub-harmonic and a inter-harmonic component shown in Fig. 8.4(a). The frequencies of the sub-harmonic and inter-harmonic are 20 Hz and 70 Hz respectively. The extracted fundamental is illustrated in Fig. 8.4(b). The inter-harmonics are revealed in Fig. 8.4(c) as the residual.

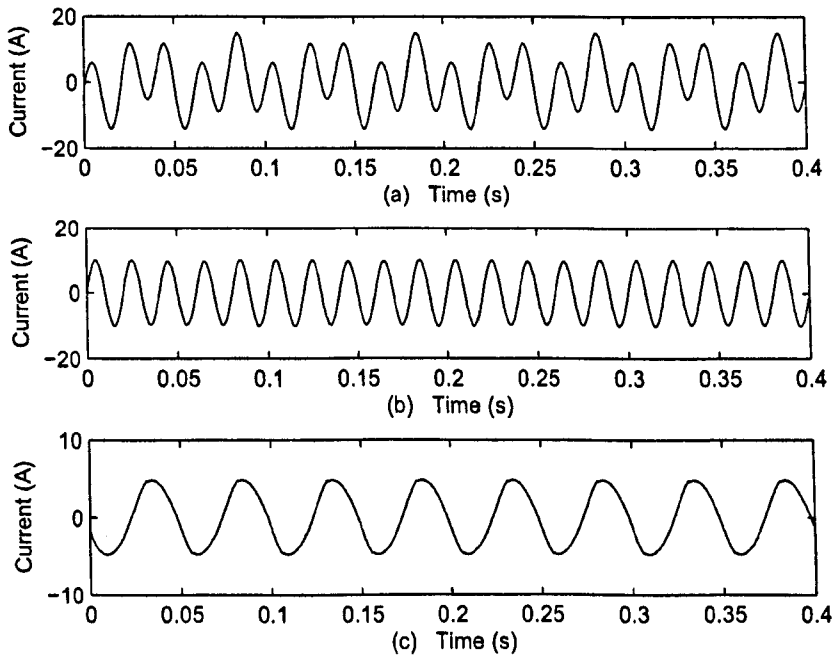

Figure 8.3: Extraction of a sub-harmonic component. a) The current waveform distorted by a 20 Hz sub-harmonic; b) The fundamental component; c) The sub-harmonic current.

8.5.3 Transformer ferroresonance

Power transformer ferroresonance is a complex electrical phenomenon that, though identified since the early 1920s, remains little understood today [150]. It is characterised by the sudden onset of very high sustained over-voltages concurrent with a high level of harmonic distortion. Ferroresonance has been known to be responsible for equipment damage and protection malfunctions.

A registered three phase ferroresonance detection method is available [151]. The operating principle is to measure the voltage unbalance of all 3 phases. The ratio of the peak values of the ferroresonant voltages on the three phases will be approximately 1, -1/2, -1/2. Ferroresonance devices look for a unbalanced voltage ratio of 2:1:1. However, in practice, the voltage ratio may be different from the expected. In some situations this lead the detection devices to fail in recognising ferroresonance.

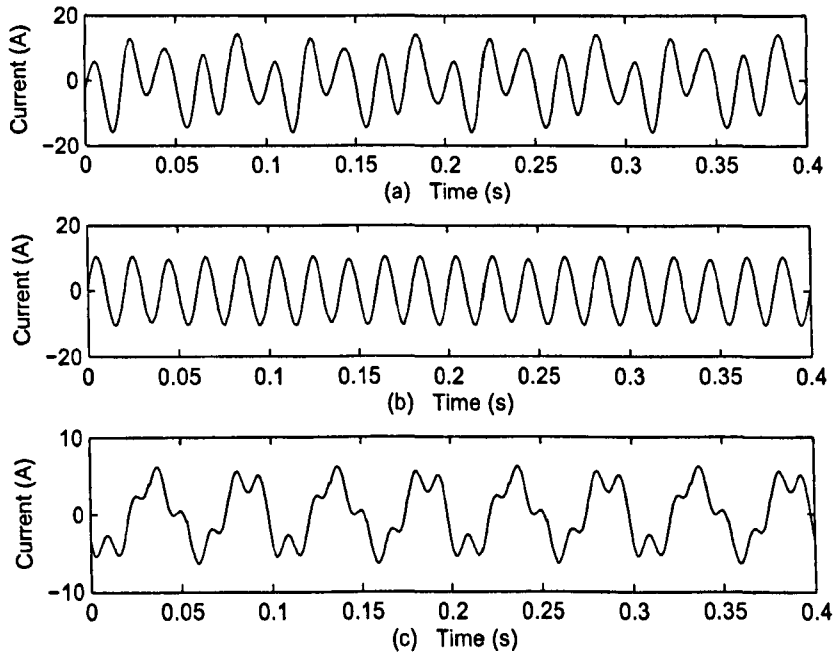

Figure 8.4: Extraction of a inter-harmonic and a sub-harmonic component. a) The current waveform distorted by inter-harmonics; b) The fundamental component; c) The inter-harmonic components in 20 Hz and 70 Hz.

The high level of sub-harmonics in the ferroresonant voltages can be recognised by the proposed method. Figure 8.5(a) shows a voltage waveform of ferroresonance provided by National Grid Transco, U.K. Besides the fundamental component, it is imposed by some harmonic and sub-harmonic components. The fundamental component, extracted and reconstructed using the proposed method, is shown in Fig. 8.5(b). With all the harmonic components subtracted, the residual, shown in Fig. 8.5(c) represents a sub-harmonic ferroresonance with a frequency of $16\frac{2}{3}$ Hz.

8.6 Summary

A new method for the estimation of harmonic components, using a morphological filter, has been presented in this chapter. The method, based on instan-

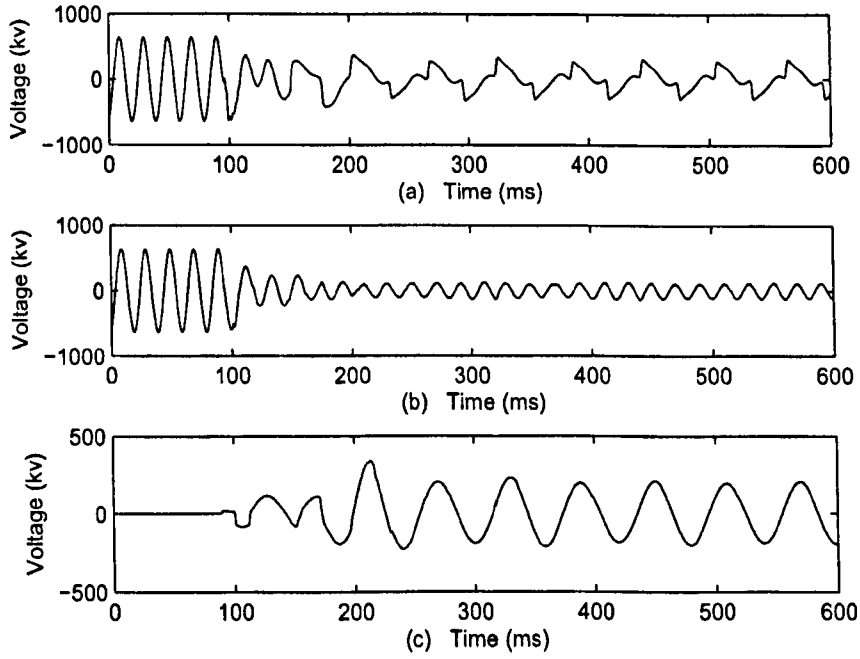

Figure 8.5: Extraction of harmonic and sub-harmonic components from a ferroresonant voltage. a) The recorded ferroresonance voltage waveform; b) The extracted fundamental component in the voltage; c) The estimated $16\frac{2}{3}$ Hz sub-harmonic.

tancous reactive power theory, is suitable for the estimation of fundamental and harmonic currents. Compared with other existing methods, the morphological filter improves the estimation accuracy. Simulation results have demonstrated the satisfactory performance of the proposed method. Moreover, the method can be extended for the detect of inter-harmonics. The results presented have shown that it can provide accurate extraction of sub-harmonic components from transformer ferroresonance voltages. Compared with the FFT which cannot be used for processing of inter-harmonics or sub-harmonics, the proposed method provides a new approach to inter-harmonic problems, requires a small computation time and can be easily implemented in real time.

Chapter 9

Multi-resolution Morphological Filter

9.1 Introduction

In this chapter, a multi-resolution morphological filter is proposed for noise removal. Firstly, a morphological filter is constructed by combining morphological operators in different orders. And then, the filter is developed at a multi-resolution level with the introduction of a multi-resolution decomposition scheme. The filter is very effective for eliminating noise from signals, especially in the case of pulse noise. The performance of this multi-resolution morphological filter is improved by a compensation step, which is a step of update in a lifting scheme. The simulation results validate the advantage and potential of the filter.

9.2 Multi-resolution decomposition scheme

A signal analysis technique, named the multi-resolution method, has found wide application in recent years. It has been recognised as an important signal processing tool for various reasons: (i) there is strong evidence that the human visual system processes information in a "multi-resolution" fashion; (ii)

signals usually consist of features of physically significant structure at different resolutions; (iii) sensors may provide signals of the same source at multiple resolutions; (iv) multi-resolution algorithms offer computational advantages and, moreover, appear to be robust.

In order to remove the high frequencies in signals or images, the most popular and earliest multi-resolution approach is to obtain a coarse level signal by sub-sampling a fine-resolution signal with a method called linear smoothing. A detailed pyramid can then be derived by subtracting from each level; the best known example is the Laplacian pyramid [152].

It has been recognised that multi-resolution decomposition schemes provide convenient and effective ways to process information. Many linear and non-linear multi-resolution signal decomposition schemes, including wavelet and many morphological schemes have been presented. All these multi-resolution techniques are not fundamentally different. In order to provide a unified standpoint for linear and non-linear pyramids, a set of foundation theories, named morphological pyramid and morphological wavelet, are derived from traditional wavelet and pyramid theories which are presented by John Goutsias and Henk J. A. M. Heijmans [153][154].

9.2.1 Pyramid transform

To obtain a mathematical representation for a multi-resolution signal decomposition scheme, a sequence of signal domains are assigned to each level of the scheme, and analysis and synthesis operators between the different levels are needed. In order to simplify signal representation, the analysis operators are designed to reduce the information, while the synthesis operators are designed to undo this process and resume the loss of information. These theories have been widely accepted as approaches to multi-resolution signal decomposition [155]. Moreover, the analysis and synthesis operators depend on the application at hand and a sound theory should be able to treat them from a general point of view.

Let $J \subseteq \mathbb{Z}$ be an index set indicating the levels in a multi-resolution signal

decomposition scheme. J is considered to be finite or infinite. A domain V_j of signals is assigned at each level j. No particular assumptions on V_j are made at this point. In this framework, signal analysis consists of decomposing the signal in the direction of increasing j. An analysis operator is presented to accomplish this task $\psi_i^{\uparrow} : V_j \rightarrow V_{j+1}$. On the other hand, signal synthesis proceeds in the direction of decreasing j, by means of synthesis operator $\psi_i^{\downarrow} : V_{j+1} \rightarrow V_j$, where the upward arrow indicates that the operator $\psi^{\uparrow}$ maps a signal to a level higher in the pyramid, whereas the downward arrow indicates that the operator $\psi^{\downarrow}$ maps a signal to a level lower in the pyramid.

The analysis operator $\psi_j^{\uparrow}$ is designed to reduce information in order to simplify signal representation at level $j+1$, whereas the synthesis operator $\psi_j^{\downarrow}$ is designed to map this information back to level j.

A signal can be transferred from any level in the pyramid to a higher level j by successively composing consecutive analysis operators: $\psi_{i,j}^{\uparrow} = \psi_{j-1}^{\uparrow}\psi_{j-2}^{\uparrow}\cdots\psi_i^{\uparrow}$, which maps an element in V_i to an element in V_j $(j > i)$. On the other hand, the composed synthesis operator, $\psi_{j,i}^{\downarrow} = \psi_i^{\downarrow}\psi_{i+1}^{\downarrow}\cdots\psi_{j-1}^{\downarrow}$, takes the signal back from level j to level i. Finally, the composition can be defined as: $\hat{\psi}_{j,i} = \psi_{j,i}^{\downarrow}\psi_{i,j}^{\uparrow}$, which takes a signal from level i to level j and back to level i again.

Synthesis operators and analysis operators play an important role in constructing decomposition schemes. A family $\psi_{i,j}^{\uparrow}$ of analysis operators map the signal in domain V_j into V_{j+1} and a family of synthesis operators $\psi_{j,i}^{\downarrow}$ map the signal from domain V_{j+1} back into V_j. If the analysis and synthesis operator $\psi_{i,j}^{\uparrow}$, $\psi_{j,i}^{\downarrow}$ satisfy the pyramid condition $\psi_{i,j}^{\uparrow}\psi_{j,i}^{\downarrow} = \mathrm{id}$ on V_{j+1}, where id is the identity operator, no information will lost by synthesis and analysis. It is the fundamental principle to construct multi-resolution decomposition schemes.

Analysis of a signal $x \in V_j$, followed by synthesis, yields an approximation $\hat{x} = \psi_j^{\downarrow}\psi_j^{\uparrow} \in \hat{V}_j$ of x. It is assumed here that there exists a subtraction operator $(x, \hat{x}) \rightarrow x \dot{-} \hat{x}$ mapping $V_j \times \hat{V}_j$ into a set Y_j. Furthermore, it is assume that there exists an addition operator $(\hat{x}, y) \rightarrow \hat{x} \dot{+} y$ mapping $\hat{V}_j \times Y_j$ into V_j. The details $y = x \dot{-} \hat{x}$ contains information about x which is not present in $\hat{x}$ and the details y. As a result, the assumption of perfect reconstruction is introduced

as follows:

$$\hat{x}\dot{+}(x\dot{-}\hat{x}) = x, \text{ if } x \in V_j \text{ and } \hat{x} = \hat{\psi}_{j,j+1}(x), \tag{9.2.1}$$

which leads to the following recursive signal analysis scheme:

$$x \to \{y_0, x_1\} \to \{y_0, y_1, x_2\} \to \cdots \{y_0, y_1, \cdots, y_j, x_{j+1}\} \to \cdots \tag{9.2.2}$$

$$\begin{cases} x_0 = x \in V_0 \\ x_{j+1} = \psi_j^{\uparrow}(x_j) \in V_{j+1},\ j \geq 0 \\ y_j = x_j\dot{-}\psi_j^{\downarrow}(x_{j+1}) \end{cases} \tag{9.2.3}$$

If the perfect reconstruction condition is satisfied, signal $x \in V_0$ can be exactly reconstructed from $x_{j+1}, y_0, y_1, \cdots, y_j$ by means of the backward recursion:

$$x = x_0, x_j = \psi_j^{\downarrow}(x_{j+1})\dot{+}y_j, j \geq 0. \tag{9.2.4}$$

9.2.2 Coupled wavelet

Compared with the structure of the morphological pyramid, morphological coupled wavelet is comprised of two analysis operators: a signal analysis operator, a detailed analysis operator and one synthesis operator.

V_j represents the signal space at level j and W_j is the detailed space at level j. $\psi_j^{\uparrow} : V_j \to V_{j+1}$ is defined as the signal analysis operator and $\omega_j^{\uparrow} : W_j \to W_{j+1}$ as the detailed analysis operator. The synthesis operator $\Psi_j^{\downarrow}$ maps the information back to the lower levels.

In order to guarantee that no information is lost and that the decomposition is non-redundant, the analysis operators $\psi_j^{\uparrow}, \omega_j^{\uparrow}$ and synthesis operator $\Psi_j^{\downarrow}$ must follow the condition below:

$$\begin{aligned} &\psi_j^{\uparrow}(\Psi_j^{\downarrow}(x,y)) = x, \text{ if } x \in V_{j+1}, y \in W_{j+1}, \\ &\omega_j^{\uparrow}(\Psi_j^{\downarrow}(x,y)) = y, \text{ if } x \in V_{j+1}, y \in W_{j+1}. \end{aligned} \tag{9.2.5}$$

Furthermore, it is required to yield a complete signal representation, in the sense that the mapping $(\psi_j^{\uparrow}, \omega_j^{\uparrow}) : V_j \to V_{j+1} \times W_{j+1}$ and $\Psi_j^{\downarrow} : V_{j+1} \times W_{j+1} \to V_j$ are inverses of each other. This leads to the following condition:

$$\Psi_j^{\downarrow}(\psi_j^{\uparrow}(x), \omega_j^{\uparrow}(x)) = x, \text{ if } x \in V_j. \tag{9.2.6}$$

So, given an input signal $x_0 \in V_0$, consider the following recursive analysis scheme:

$$\begin{aligned} x_0 \rightarrow \{x_1, y_1\} &\rightarrow \{x_2, y_2, y_1\} \rightarrow \cdots \\ &\rightarrow \{x_k, y_k, y_{k-1}, \cdots, y_1\} \rightarrow \cdots, \end{aligned} \tag{9.2.7}$$

where

$$\begin{aligned} x_{j+1} &= \psi_j^{\uparrow}(x_j) \in V_{j+1}, \\ y_{j+1} &= \omega_j^{\uparrow}(x_j) \in W_{j+1},\ j \geq 0. \end{aligned} \tag{9.2.8}$$

The original signal x_0 can be exactly reconstructed from x_k and y_1, y_2, $\cdots$, y_k by means of the following recursive synthesis scheme:

$$x_j = \Psi_j^{\downarrow}(x_{j+1}, y_{j+1}),\ j = k-1,\ k-2,\ \cdots,\ 0. \tag{9.2.9}$$

This signal representation scheme is referred as the coupled wavelet decomposition scheme.

The un-decimated algorithm applies the wavelet transform and omits both down-sampling in the forward and up-sampling in the inverse transform. It applies the transform at each point of the signal saves the detailed coefficients and uses the low frequency coefficients for the next level. By using all coefficients at each level, the high-frequency information is allocated very well [156].

9.3 A multi-resolution morphological filter for noise removal

The underlying basis of a morphological filtering technique is to process signals by an SE. Two well-known classes of morphological filters, opening and closing are denoted as $\circ$ and $\bullet$ respectively. In order to eliminate both of the positive noise and negative noise using the same SE, a open-closing and a close-opening filter can be realised through cascade connection of the opening and closing transform in different orders. The two filters are defined as follows:

$$\mathrm{OC}(f(t)) = (f \circ g \bullet g)(t), \tag{9.3.1}$$

$$\mathrm{CO}(f(t)) = (f \bullet g \circ g)(t), \tag{9.3.2}$$

where $f(t)$ and $g(t)$ represent a signal and an SE respectively.

As discussed in Chapter 8, there is a statistical deviation problem existing in the open-closing filter and closing-opening filter. In order to lower the output deviation and achieve the best performance, two filters can be cascaded to form a combined filter. The output of the filter is defined as:

$$\gamma(f(t)) = [\mathrm{CO}(f(t) + \mathrm{OC}(f(t))]/2. \tag{9.3.3}$$

In this filter, the SE acts as a moving window through the signal to extract the high-frequency components. If the length of the SE is longer than the width of the noise in a segment of the signal, the noise in this segment can be eliminated.

A multi-resolution morphological filter can be constructed by combining the operators of opening and closing with the application of a coupled wavelet scheme. The signal analysis operator $\psi_j^{\uparrow}$, $\omega_j^{\uparrow}$ and synthesis operator $\Psi_j^{\downarrow}$ are designed as:

$$\begin{aligned}
&\psi_j^{\uparrow} = x_{j+1} = \gamma(x_j), \\
&\omega_j^{\uparrow} = y_{j+1} = (\mathrm{id} - \gamma(x_j)), \\
&\Psi_j^{\downarrow}(\psi_j^{\uparrow}(x_j), \omega_j^{\uparrow}(x_j)) = x_j = (\mathrm{id} - \gamma(x_j) + \gamma(x_j), \\
&\gamma(x_j) = (\mathrm{OC} + \mathrm{CO})(x_j)/2,
\end{aligned} \tag{9.3.4}$$

where $x_j \in V_j$, $x_{j+1} \in V_{j+1}$ and $y_{j+1} \in W_{j+1}$. When $j = 1$, x_1 is the input signal. The multi-resolution morphological filter is effective for enhancing a contaminated signal from its noisy background. A flat SE is selected for its simpleness. The initiatory length of the SE is 2 at level 1 and increases to $j+1$ at level j.

9.4 Applications in noise removal

A sinusoidal voltage waveform polluted by white noise is dealt with the proposed filter, and the results are shown in Fig. 9.1. The value of Signal to

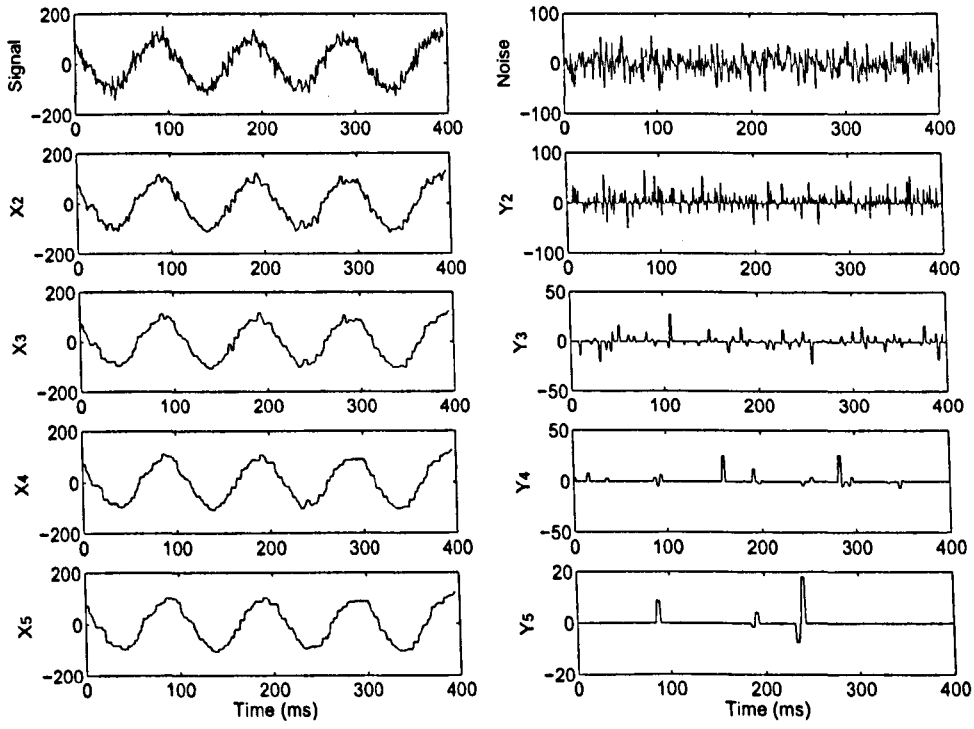

Figure 9.1: The De-noising results using a flat SE.

Noise Ratio (SNR) in this case is 27.96 dB. Using the proposed multi-resolution morphological filter, the decomposition results, including the scale signals X_i and details Y_i $(i = 1, 2, \cdots, 5)$, are arranged in row respectively as shown in Fig. 9.1. In the waveform of X_5, a part of the noise has been filtered. However, the curves, corresponding to the samples processed by the filter, are replaced by flat lines, which causes the loss of the sinusoidal features in X_5. The detailed performance of the noise elimination at each level is listed in Table 9.1.

Table 9.1: The performance of the noise reduction of the multi-resolution morphological filter

Signal	X_2	X_3	X_4	X_5
27.96 dB	34.23 dB	37.26 dB	38.16 dB	38.19 dB

9.5 A morphological lifting filter for feature recovery

As discussed in the previous section, a multi-resolution morphological filter using a flat line SE causes the loss of some features in the approximation waveforms. The filter simply replaces the curves with a series of flat lines. As a result, the signal becomes more distorted as the length of the SE increases. Therefore, a compensation process needs to be applied for the recovery of the waveform.

The lifting scheme [157][158] was originally developed to adjust wavelet transforms to complex geometries and irregular sampling, which leads to the so-called second generation wavelet. Lifting amounts to modifying the analysis and synthesis operators in such a way that the properties of the modified scheme are better than those of the original one, *i.e.*, wavelets may be adapted to situations that do not allow translation and dilation like non-Euclidean spaces. First generation wavelets are all translations and dilations of one or a few basic shapes, so the Fourier transform is the crucial tool for wavelet construction. Lifting, on the contrary, is built entirely spatial therefore ideally suited for building the second generation wavelets when Fourier techniques are no longer available. As it is restricted to the translation and dilation invariant, lifting comes down to well-known ladder type structures and certain factoring algorithms.

Using lifting it is particulary easy to build non-linear wavelet transforms. A typical example is that wavelet transforms map integers to integers. Also, lifting allows for adaptive wavelet transforms, which means that the analysis of a function can be started from the coarsest levels and then the finer levels can be built by refining the areas of interest [159].

A typical lifting stage is comprised of three steps: split, predict and update. In the process of update, the signal analysis operator $\psi^{\uparrow}$ and the detailed synthesis operator $\omega^{\downarrow}$ in the uncoupled case could be modified respectively to improve the quality of the filter. The information in the details y_j is used to

modify the scale signal x_j to $x_j^{'}$, and then y_j can also be updated according to the new scale signal $x_j^{'}$:

$$x_j^{'} = x_j - \lambda(y_j), \tag{9.5.1}$$

$$y_j^{'} = y_j - \pi(x_j^{'}). \tag{9.5.2}$$

Here, λ and π are operators mapping W_j to V_j and V_j to W_j respectively.

Upon to the proposed morphological multi-resolution filter, the details, Y_i, left in each level can provide information for the step of update. In the details Y_i, the samples are divided into two groups, zero and non-zero, according to the values. The non-zero samples correspond to the points needing update. These samples can be replaced by a linear, cubic or polynomial interpolation. The process is introduced as follows.

For example, in level j, if the samples $\{s_{j,k-1}, s_{j,k}, s_{j,k+1}\}$ have correlative non-zero values in the detailed signal at the same level, the three samples could be updated by a linear or cubic interpolation.

$$\begin{aligned} s_{j,k-4}, s_{j,k+2} &\Longrightarrow s_{j,k-1}, \\ s_{j,k-2}, s_{j,k+2} &\Longrightarrow s_{j,k}, \\ s_{j,k-2}, s_{j,k+4} &\Longrightarrow s_{j,k+1}. \end{aligned} \tag{9.5.3}$$

$$\begin{aligned} s_{j,k-7}, s_{j,k-4}, s_{j,k+2}, s_{j,k+5} &\Longrightarrow s_{j,k-1}, \\ s_{j,k-4}, s_{j,k-2}, s_{j,k+2}, s_{j,k+4} &\Longrightarrow s_{j,k}, \\ s_{j,k-5}, s_{j,k-2}, s_{j,k+4}, s_{j,k+7} &\Longrightarrow s_{j,k+1}. \end{aligned} \tag{9.5.4}$$

In general, if n samples in a segment of a signal are updated, a polynomial p in degree $n-1$ is constructed. The value at point l can be calculated as:

$$s_{j,l} = p(x_{j,k+l}), \tag{9.5.5}$$

while l belongs to the non-zero points in the details Y_j at level j, and the points at $k+j$ have zero values in the corresponding detailed level. The values of these samples are updated by the constructed polynomial. In implementation, it is necessary to adopt a method to evaluate the interpolating polynomial at a single location with the values and locations of some samples given.

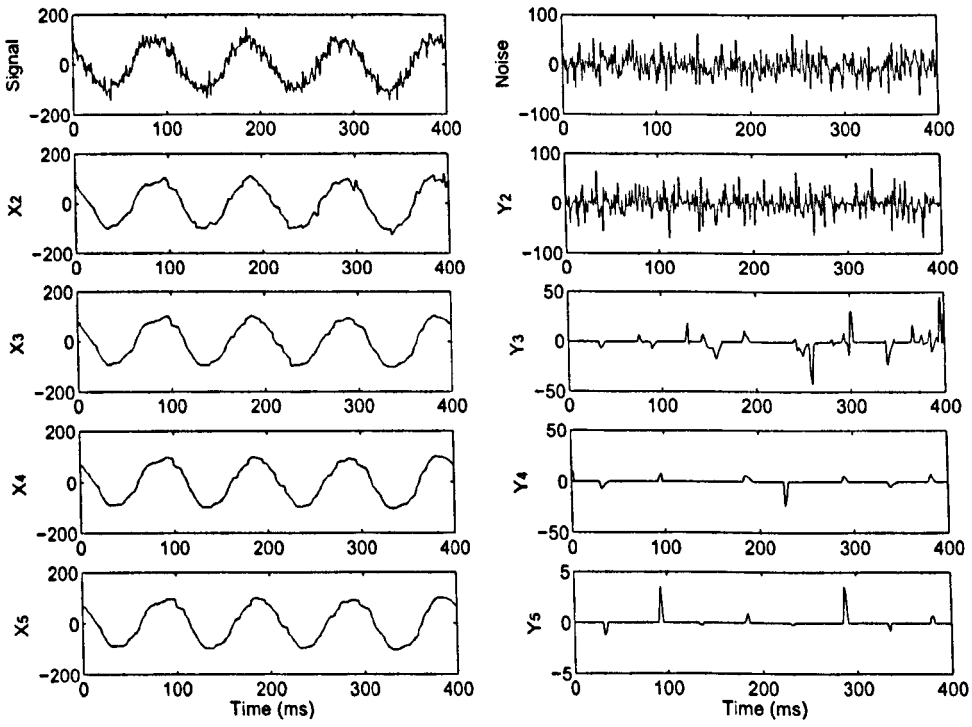

Figure 9.2: The De-noising results using the improved filter.

9.6 Recovery results

To evaluate the effectiveness of the proposed multi-resolution morphological lifting filter, the same voltage waveform is used as a reference. The de-noised scale signals X_i and residual details Y_i are shown in Fig. 9.2. The linear interpolation is utilised for update.

The performance of the noise removal can be seen from Table 9.2. In comparison with the results shown in Table 9.1, the values of SNR are increased which indicates that the effect of the filter has been improved with the updating process applied. In concomitant with the noise filtered, the sinusoidal features of the voltage waveform are kept in the results of X_i as shown in Fig. 9.2.

Table 9.2: The performance of the noise reduction after updating

Signal	X_2	X_3	X_4	X_5
27.96dB	40.60dB	42.99dB	43.38dB	43.62dB

9.7 Summary

The basic principles of morphological pyramid and morphological wavelet have been briefly introduced in this chapter. Based on the combination of morphological operations with basic multi-resolution decomposition schemes, a multi-resolution morphological filter has been proposed. The desirable properties demonstrated in the analysis of the proposed filter, manifest the morphological multi-resolution filter as a promising method for noise removal in signals.

Furthermore, the lifting scheme is introduced as an extension of the multi-resolution morphological filter. Results obtained indicate the performance of this approach in noise removal is greatly improved. This chapter has provided a method in designing flexible non-linear filters in different situations. The proposed multi-resolution morphological filter is numerically simple and adapts itself to the content of signals. Compared with linear filters, it has a better performance for pulse noise removal.

Chapter 10

Conclusion and Future Work

This chapter concludes this thesis, summarises the major results of the presented research work and indicates possible directions for further investigation of morphological protection relays.

10.1 Conclusion

The objective of this thesis is to develop a new generation of protection relays based on MM. MM is a new branch of mathematics which is totally different from the integral transforms, *i.e.*, Fourier transform and WT. This thesis focuses, in depth, on the investigation of a new methodology based on MM for extracting components of transient and non-periodic signals to develop advanced algorithms for protection relays.

Mathematical morphological filters are constructed using various sequences of morphological operators. A variety of morphological filters have been constructed for different purposes in this thesis. These morphological filters have shown satisfying performance in noise reduction, feature and shape extraction in different cases.

In order to accurately extract fundamental frequency components from post-fault signals, a morphological filter has been presented to extract exponentially decaying DC offset components. The simulation results have demonstrated that the morphological filter can estimate and subtract the exponen-

tially decaying DC components from the post-fault signals. It is very effective for solving the problem of waveform distortion caused by a fault. As a result, the fundamental frequency components are extracted accurately without long time delay.

With the application of morphological synthesis and analysis operators, a multi-resolution morphological filter has been constructed. Using this filter, an observed current signal can be decomposed into a group of peaks and valleys which explore the features of the current in details. Through the comparison of the values of these peaks and valleys, the discrimination between an inrush and a fault current is achieved. The simulation studies have shown that the filter works satisfactorily using a sampling window which is much shorter than that adopted by the conventional methods.

The advancement of lifting schemes provides a useful and alternative way to construct WTs, which makes it possible to extend wavelets into non-linear domains because lifting schemes are able to provide an entire spatial-domain interpretation of the transforms. The morphological operators can be intergraded into the predicting and updating stage of the lifting schemes, and make linear operators be replaced by non-linear ones. The combination of lifting schemes with MM forming, a new class of schemes, named MLSs, have been implemented in this thesis as effective tools for identifying the shapes of distorted waveforms.

For protection relaying purpose, a promising MLS has been implemented for the detection of current transformer saturation in this thesis. With the scheme applied, the non-sinusoidal characteristics of the distorted secondary current waveform are extracted during the saturation period in the predicting stage of the lifting scheme. The distorted saturation section is distinguished from the healthy sections in the secondary current and the current in the distorted section is compensated in real time once saturation begins by using a compensation algorithm. The simulation results have validated that the scheme is able to detect the sections of the distorted secondary currents accurately in all the test cases.

In addition, a new algorithm for EHV transmission line protection, based on another MLS, has been presented to degrade the effect of noise on fault-generated travelling waves. A lifting scheme, associating with a morphological edge detector which combines the advantages of the lifting scheme and MM, has been used to filter the noise and preserve the gradients of the wavefronts. It has demonstrated that the scheme has an excellent capability for the extraction of the transient features in travelling waves.

In a noisy environment, to detect different power disturbances online, a morphological filter combining an MMG has been developed to extract the features of the disturbances. The different disturbances can be classified based upon the extracted features. Furthermore, the harmonics in a signal can be estimated using a morphological low-pass filter. In addition, another morphological filter, based on a multi-resolution decomposition scheme, has been developed for noise removal in this thesis. The filter is numerically simple and locally adaptive. Compared with linear filters, it has better performance in eliminating of pulse noise, and leads to a simpler calculation. Moreover, it provides a methodology of designing flexible non-linear filters.

10.2 Future work

With an understanding of the presented methods and schemes, the following aspects would be worthy of further investigations:

- The developed morphological protection schemes require much less computation than conventional protection algorithms, as the computation only involves a few mathematical operations and time delay shifts. Reliability is a crucial issue for protection relay design. The current protection relays suffer low reliability due to complex calculations for sampling, filtering, integral transform and fault identification, which requires many integrated circuits to implement. Therefore, a morphological-based relay could be built into a single integrated circuit and the reliability of the protection will be greatly improved. The hardware design for the devel-

oped morphological protection scheme, especially with the application of Very-Large-Scale Integration (VLSI) and embedded system technology, deserves to be investigated in the future.

- The primary function of protection relays was to simply protect the power system equipment in the early days. However, with the emergence of microprocessor relays, protection relays are capable of providing both protection and measurement functions. Furthermore, concomitant with the development of embedded system technology, the relays can communicate with each other, and the availability of broadband communication links allows them to share information that could be used for a variety of purposes. The advancement of this technology, with the time synchronising capability of GPS, is the basis of designing a wide-area protection system. With the implementation of morphological protection algorithms, a system can be built for fault diagnosis, including fault detection, location and classification, by comparing the shapes of current or voltage waveforms from different relays in a wide area. A framework including algorithm development and system coordination needs to be studied and analysed in the future.

References

[1] G. D. Rockerfeller. Fault protection with digital computer. *IEEE Trans. on Power Apparatus and Systems*, 88(4):438–461, Apr., 1969.

[2] G. D. Rockerfeller, C. L. Wagner, J. R. Linders, K. L. Hicks, and D. T. Rizy. Adaptive transmission system relaying concepts for improved performance. *IEEE Trans. on Power Delivery*, 3(4):1146–1458, Oct., 1988.

[3] J. S. Thorp, A. G. Phadke, S. H. Horowitz, and M. M. Begovic. Some applications of phasor measurements to adaptive protection. *IEEE Trans. on Power Delivery*, 3(2):197–798, May, 1988.

[4] C. Aguilera, E. Orduna, and G. Ratta. Adaptive noncommunication protection based on traveling waves and impedance relay. *IEEE Trans. on Power Delivery*, 21(3):1154–1162, Jul., 2006.

[5] M. J. Damborg, M. Kim, J. Huang, S. S. Venkata, and A. G. Phadke. Adaptive protection as preventive and emergency control. *IEEE Power Engineering Society Summer Meeting*, 2:1208–1212, 16-20 Jul., 2000.

[6] A. T. Johns and R. K. Aggarwal. Digital simulation of faulted ehv transmission lines with particular reference to very-high-speed. *IEE Procedings Part C*, 123(4):354–359, Apr., 1976.

[7] L. V. Bewley. *Travelling waves on transmission systems.* John Wiley and Sons, New York, 1951. Second edition.

[8] R. K. Aggarwal, A. T. Johns, Y. H. Song, R. W. Dum, and D. S. Fitton. Neural-network based adaptive single-pole autoreclosure technique for

ehv transmission systems. *IEE Proceedings-Generation, Transmission and Distribution*, 141(2):155–160, Mar., 1994.

[9] M. Chamia and S. Liberman. Ultra high speed relay for ehv/uhv transmission lines - development, design and application. *IEEE Trans. on Power Apparatus and Systems*, 97(6):2104–2116, Mar./Apr., 1978.

[10] R. K. Aggarwal, Y. H. Song, and A. T. Johns. Adaptive three-phase autoreclosure for double-circuit transmission systems using neural networks. *IEE 2nd International Conference on Advances in Power System Control, Operation and Management, Hong Kong*, pages 389–392, Dec., 1993.

[11] R. K. Aggarwal, Q. Y. Xuan, R. W. Dunn, A. T. Johns, and A. Bennett. A novel fault classification technique for double-circuit lines based on a combined unsupervised/supervised neural network. *IEEE Trans on Power Delivery*, 14(4):1250–1256, Oct., 1999.

[12] Z. Q. Bo, R. K. Aggarwal, A. T. Johns, H. Y. Li, and Y. H. Song. A new phase selection technique based on fault generated high frequency noise using neural networks. *IEEE Trans. on Power Delivery*, 12(1):106–115, Jan., 1997.

[13] S. Mallat. A theory for multiresolution signal decomposition: The wavelet representation. *IEEE Trans. on Pattern Analysis and Machine Intelligence*, 11(7):674–693, Jul., 1989.

[14] A. H. Osman and O. P. Malik. Transmission line distance protection based on wavelet transform. *IEEE Trans. on Power Delivery*, 19(2):515–523, Apr., 2004.

[15] O. A. S. Youssef. New algorithm to phase selection based on wavelet transforms. *IEEE Trans. on Power Delivery*, 17(4):908–914, Oct., 2002.

[16] W. Chen, O. P. Malik, X. G. Yin, D. S. Chen, and Z. Zhang. Study of wavelet-based ultra high speed directional transmission line protection. *IEEE Trans. on Power Delivery*, 18(4):1134–1139, Oct., 2003.

[17] S. A. Saleh and M. A. Rahman. Modeling and protection of a three-phase power transformer using wavelet packet transform. *IEEE Trans. on Power Delivery*, 20(2):1273–1282, Apr., 2005.

[18] G. Matheron. *Random Sets and Integrated Geometry.* Wiley, New York, 1975.

[19] J. Serra (ed.). *Image Analysis and Mathematical Morphology.* Academic Press, New York/London, 1982.

[20] J. Serra. *Image Analysis and Mathematical Morphology II: Theoretical Advances.* Academic Press, London, 1988.

[21] J. Serra. Automatic scanning device for analysing textures. *Patent, Patendted in: Belgium, Canada, Great-Britain, Japan, Sweden, USA.*, 23(273), Jul., 1965.

[22] G. Matheron. *Elments pour une thorie des milieux poreux.* Paris: Masson, 1976.

[23] L. Koskinen, J. Astola, and Y. Neuvo. Soft morphological filters. *In Proceedings of SPIE Symposium on Image Algebra and Morphological Image Processing*, pages 262–270, 1991.

[24] P. Kuosmanen and J. Astola. Soft morphological filtering. *Mathematical Imaging and Visions*, 5(3):231–262, 1995.

[25] A. Gasteratos and I. Andreadis. Soft mathematical morphology: Extensions, algorithms and implementations. *Advances in Imaging and Electron Physics*, 110:63–99, 1999.

[26] D. Shinha and E. R. Dougherty. Fuzzy mathematical morphology. *Visual Communication and Image Representation*, 3(3):286–302, 1992.

[27] A. Gasteratos, I. Andreadis, and P. Tsalides. Realisation of soft morphological filters. *IEEE Proceedings: Circuits Devices and Systems*, 145(3):201–206, 1998.

[28] I. Bloch and H. Maitre. Fuzzy mathematical morphology: Extensions, algorithms and implementations. *Advances in Imaging and Electron Physics*, 110:63–99, 1999.

[29] Z. Lu, D. R. Turner, Q. H. Wu, J. Fitch, and S. Mann. Morphological transform for detection of power quality disturbances. *2004 International Conference on Power System Technology, PowerCon 2004*, 2:1644 – 1649, Nov. 21-24, 2004. Singapore.

[30] Z. Lu, J. S. Smith, Q.H. Wu, and J. Fitch. Empirical mode decomposition for power quality monitoring. *Transmission and Distribution Conference and Exhibition: Asia and Pacific, 2005 IEEE/PES*, pages 1–6, Aug. 15-18, 2005. Dalian, China.

[31] Z. Lu, J. S. Smith, Q. H. Wu, and J. Fitch. Identification of power disturbances using morphological transform. *Transactions of the Institute of Measurement and Control*, to be appear in 2006.

[32] Z. Lu, Q. H. Wu, and J. Fitch. A morphological filter for estimation of power system harmonics. *2006 International Conference on Power System Technology, Powercon 2006*, Oct. 22-26, 2006. Chongqing, China.

[33] Y. Nakagawa and A. Rosenfeld. A note on the use of local min and max operations digital picture processing. *IEEE Trans. Systems Man Cybernet SMC*, 8(8):632–635, 1978.

[34] H. J. A. M. Heijmans. *Morphological Image Operators*. Academic Press, Boston, 1994.

[35] J. L. Kelly. *General Topology*. Springer-Verlag, 1975.

[36] H. Minkovski. Volumen und oberflache. *Math. Annalen*, 57:447–495, 1903.

[37] E. W. Weisstein. *MathWorld.* A Wolfram Web Resoure. http://mathworld.wolfram.com.

[38] K. Ciesielski. *Set Theory for the Working Mathematician.* Cambridge University Press, 1997.

[39] J. Serra and L. Vincent. An overview of morphological filtering. *Circuits Systems and Signal Processing*, 11(1):48–108, 1992.

[40] H. J. A. M. Heijmans. Composing morphological filters. *IEEE Trans. on Image Processing*, 6(5):713–723, May, 1997.

[41] D. Wang and D. C. He. A fast implementation of 1-d grayscale morphological filters. *IEEE Trans. on Circuits and Systems*, 41(9):634–636, 1994.

[42] J. Goutsias and H. J. A. M. Heijmans. Nonlinear multi-resolution signal decomposition schemes - part i: Morphological pyramids. *IEEE Trans. on Image Processing*, 9:pp.1862–1876, Nov., 2000.

[43] H. J. A. M. Heijmans and J. Goutsias. Nonlinear multi-resolution signal decomposition schemes - part ii: Morphological wavelet. *IEEE Trans. on Image Processing*, 9:1897–1913, Nov., 2000.

[44] P. J. Burt and E. H. Adelson. The laplacian pyramid as a compact image code. *IEEE Trans. on Communications*, COM-31:532–540, 1983.

[45] R. Claypoole, G. David, W. Sweldens, and R. Baraniuk. Nonlinear wavelet transforms for image coding. *Proc. 31st Asilomar Conf. Signals, Systems, Computers, Pacific Grove, CA*, 1:662–667, 1997.

[46] R. L. Claypoole, R. G. Baraniuk, and R. D. Nowak. Adaptive wavelet transforms via lifting. *Proc. IEEE Int. Conf. Acoustics, Speech, Signal Processing, Seattle, WA*, May 12-15, 1998.

[47] R. Claypoole et al. Lifting construction of nonlinear wavelet transforms. *Proc. IEEE-SP Int. Symp. Time-Frequency Time-Scale Analysis, Pittsburgh, PA*, pages 49–52, Oct., 1998.

[48] R. L. Claypoole, R. G. Baraniuk, and R. D. Nowak. Adaptive wavelet transforms via lifting. *Dept. Elect. Comput. Eng., Rice Univ., Houston, TX, Tech. Rep. 9304*, Apr., 1999.

[49] Henk J. A. M. Heijmans and John Goutsias. Nonlinear multiresolution signal decomposition schemes-part ii: Morphological wavelets. *IEEE Trans. on Image Processing*, 9(11):1897–1913, Nov., 2000.

[50] M. Vetterli and C. Herley. Wavelets and filter banks: Theory and design. *IEEE Trans. on Signal Processing*, 40:2207–2232, 1992.

[51] I. Daubechies. Ten lectures on wavelets. volume 61, Society for Industrial and Applied Mathematics, Philadelphia, PA, US, 1992.

[52] W. Sweldens. The lifting scheme: a construction of second generation wavelets. *SIAM Journal on Mathematical Analysis*, 29(2):511–546, 1998.

[53] Sun-Li Yu Jyh-Cherng Gu. Removal of dc offset in current and voltage signals using a novel fourier filter algorithm. *IEEE Trans. on Power Delivery*, 15(1):73–79, Jan., 2000.

[54] M. S. Sachdev and M. A. Baribeau. A new algorithm for digital impedance relays. *IEEE Trans. on Power Apparatus and Systems*, 98:2232–2240, Nov./Dec., 1979.

[55] G. Gabriel Benmouyal. Removal of dc-offset in current waveforms using digital mimic filtering. *IEEE Trans. on Power Delivery*, 10:621–630, Apr., 1995.

[56] S. Franco. *Electric circuits fundamentals.* Saunders College Publishing, Fort Worth, 1995.

[57] B. J. Mann and I. F. Morrison. Digital calculation of impedance for transmission line protection. *IEEE Trans. on Power Apparatus and Systems*, 90(1):270–279, Jan./Feb., 1971.

[58] B. D. Russel and M. E. Council. *Power System Control and Protection.* NY: Academic Press, New York, 1978.

[59] M. T. Heideman, D. H. Johnson, and C. S. Burrus. Gauss and the history of the fast fourier transform. *IEEE Acoustics Speech and Signal Processing Magazine*, 1(4):14–21, 1984.

[60] P. Duhamel and M. Vetterli. Fast fourier transforms: A tutorial review and a state of the art. *Signal Processing*, 19:259–299, 1990.

[61] M. Yalla. A digital multifunction protective relay. *IEEE Trans. on Power Delivery*, 7(0885-8977):193–201, 1992.

[62] A. T. Johns and S. K. Salman. *Digital Protection for Power Systems.* Institution of Electrical Engineers, London, UK, 1995.

[63] E. Kreyszig. *Advanced Engineering Mathmatics.* John Wiley and Sons, New York, NY, 1995.

[64] M. S. Sachdev and M. A. Baribeau. A new algorithm for digital impedance relays. *IEEE Trans. on Power Apparatus and Systems*, 98(6):2232–2240, 1979.

[65] K. Karsai, D. Kerenyi, and L. Kiss. *Large Power Transformers.* Elsevier, 1987.

[66] W. A. Elmore. *Protective Relaying. Theory and Applications.* Marcel Dekker Inc., New York, 1994.

[67] T. Giuliante and G. Clough. Advances in the design of differential protection of power transformers. *Texas A and M University Conference for Protective Relay Engineers*, 1995. College Station, Texas, USA.

[68] S. H. Horowitz and A. G. Phadke. *Power System Relaying.* Wiley and Sons, New York, 1992.

[69] J. E. Waldron and S. E. Stanley. Design considerations for a new solid state transformer differential relay with harmonic restraint. *Western Protective Relay Conference*, 1978.

[70] J. A. Sykes and I. F. Morrison. A proposed method of harmonic restraint differential protection of transformers by digital computer. *IEEE Trans. on Power Apparatus and Systems*, 91:1266–1272, May/Jun., 1972.

[71] T. S. Sidhu, M. S. Sachdev, H. C. Wood, and M. Nagpal. Design, implementation and testing of a micor-processor-based high speed relay for detecting transformer winding faults. *IEEE Trans. on Power Delivery*, 7(1):108–117, 1992.

[72] P. Liu, O. P. Malik, C. Chen, G. S. Hope, and Y. Guo. Improved operation of differential protection of power transformers for internal faults. *IEEE Trans. on Power Delivery*, 7(4):1912–1919, 1992.

[73] G. D. Rockfeller. Fault protection with a digital computer. *IEEE Trans. on Power Apparatus and Systems*, 98:438–464, 1969.

[74] A. M. Dmitrenko. Semiconductor pulse-duration differential restraint relay. *Radiophysics and Quantum Electronics*, (3):335–339, Mar., 1970.

[75] A. Giuliante and G. Clough. Advances in the design of differential protection for power transformers. *1991 Georgia Tech. Protective Relaying Conference, Atlanta, U. S.*, pages 1–12, May 1-3, 1991.

[76] ALSTOM T and D Control Ltd. *Type MBCH Biased Differential Relay*, 1999. Service Manual.

[77] Summary of iece guide for protection of network transformers. *IEEE Trans. on Power Delivery*, 15:1496–1505, 1990.

[78] L. G. Perez, A. J. Flechsig, J. L. Meador, and Z. Obradoviic. Training an artificial neural network to discriminate between magnetizing inrush and internal faults. *IEEE Trans. on Power Delivery*, 9:434–441, Jan., 1994.

[79] Z. Moravej, D. N. Vishwakarma, and S. P. Singh. Ann-based protection scheme for power transformer. *Electric Machines and Power Systems*, 28:875–884, Dec., 1999.

[80] A. Wiszniewski and B. Kasztenny. A multi-criteria differential transformer relay based on fuzzy logic. *IEEE Trans. on Power Delivery*, 10:1786–1792, Oct., 1995.

[81] M. Gomez-Morante and D. W. Nicoletti. A wavelet-based differential transformer protection. *IEEE Trans. on Power Delivery*, 14:1351–1358, Oct., 1999.

[82] O. A. S. Youssef. A wavelet-based technique for discrimination between faults and magnetizing inrush currents in transformers. *IEEE Trans. on Power Delivery*, 18:170–176, Jan., 2003.

[83] P. Sun, J. F. Zhang, D. J. Zhang, and Q. H. Wu. Morphological indentification of transformer magnetising inrush current. *IEE Electronics Letters*, 38(9):437–438, Apr., 2002.

[84] B. Kasztenny and A. Kulidjian. An improved transformer inrush restraint algorithm increases security while maintaining fault response performance. *5rd Annual Conference for Protective Relay Engineers*, Apr., 2000. College Station, Texas, USA.

[85] A. Kulidjian, B. Kasztenny, and B. Campbell. New magnetizing inrush restraining algorithm for power transformer protection. *Proceedings of the 7th International Conference on Developments in Power System Protection*, pages 181–184, Apr. 09-12, 2001. Amsterdam, Netherlands.

[86] I. Pitas and A. N. Venetsanopoulos. Morphological shape decomposition. *IEEE Trans. on Pattern Analysis and Machine Intelligence*, 12(1):38–45, Jan., 1990.

[87] D. Coltuc and I. Pitas. Morphological residual representations of signals. *IEEE Trans. on Image Processing*, 5(11):1169–1572, Nov., 1996.

[88] Patrick Bastard, Pierre Bertrand, and Michel Meunier. A transformer model for winding fault studies. *IEEE Trans. on Power Delivery*, 9(2):690–699, Apr., 1994.

[89] P. Bertrand, A. Devalland, and P. Bastard. A simulation model for transformer internal faults base for the study of protection and monitoring systems. *12th International Conference on Electricity Distribution, Birmingham, U.K.*, 1:1.21/1–1.21/5, 1993.

[90] B. Kasztenny and M. Kezunovic. Improved power transformer protection principles for multi-citeria power transformer relaying. *Proceedings of the 12th Power Systems Computation Conference*, pages 107–113, Aug. 19-23, 1996. Dresden, Germany.

[91] A. G. Phadke and J. S. Thorp. Computer relaying for power systems. *Research Studies Press Ltd.*, pages 185–186, 1988.

[92] Y. C. Kang, J. K. Park, S. H. Kang, A. T. Johns, and R. K. Aggarwal. An algorithm for compensating the secondary current of current transformers. *IEEE Trans. on Power Delivery*, 12:116–124, Jan., 1997.

[93] T. Bunyagul, P. Crossley, and P. Gale. Overcurrent protection using signals derived from saturated measurement cts. *Proc. IEEE Power Eng. Soc. Summer Meeting, Vancouver, BC, Canada*, Jul. 15-19, 2001.

[94] C. Fernandez. An impedance-based ct saturation detection algorithm for bus-bar differential protection. *IEEE Trans. on Power Delivery*, 16:468–472, Oct., 2001.

[95] Y. C. Kang, S. H. Ok, and S. H. Kang. A ct saturation detection algorithm. *IEEE Trans. on Power Delivery*, 19(1):78–85, Jan., 2004.

[96] D. C. Yu, Z. Wang, J. C. Cummins, H.-J. Yoon, L. A. Kojovic, and D. Stone. Neural network for current transformer saturation correction. *Proc. IEEE Transm. Distrib. Conf., New Orleans, LA*, Apr., 1999.

[97] M. Chamia and S. Liberman. Ultra-high-speed relay for ehv/uhv transmission lines - development design and application. *IEEE Trans. on Power Apparatus and Systems*, PAS-97:2104–2016, Nov./Dec., 1978.

[98] M. Vitins. A fundamental concept for high speed relaying. *IEEE Trans. on Power Apparatus and Systems*, PAS-100:163–173, Jan., 1981.

[99] A. T. Johns, R. K. Aggarwal, and Z. Q. Bo. Non-unit protection technique for ehv transmission systems based on fault-generated noise, part1: signal measurement. *Proc. Inst. Elect. Eng. Gen., Transm. Dist.*, 141(2):133–140, Mar., 1994.

[100] Z. Q. Bo. A new noncommunication protection technique for transmission lines. *IEEE Trans. on Power Delivery*, 13:1073–1078, Oct., 1998.

[101] I. Daubechies. *Ten Lectures on Wavelets.* Capital City Press, 1992.

[102] H. M. Fernando and A. Ali Abur. Fault location using wavelets. *IEEE Trans. on Power Delivery*, 13:1475–1480, Oct., 1998.

[103] S. J. Huang and C. T. Hsieh. High-impedance fault detection utilizing a morlet wavelet transform approach. *IEEE Trans. on Power Delivery*, 14:1401–1410, Oct., 1999.

[104] A. M. Gaouda and M. M. A. Salama. Power quality detection and classification using wavelet multi-resolution signal decomposition. *IEEE Trans. on Power Delivery*, 14:1469–1475, Oct., 1999.

[105] X. Z. Dong, Y. Z. Ge, J. L. He, X. J. Guo, and Z. Q. Bo. Status quo and prospect of traveling waves protection of transmission lines. *Autom. Electr. Power Syst.*, 24:56–61, May, 2000.

[106] D. J. Zhang, Q. H. Wu, Z. Q. Bo, and B. Caunce. Transient positional protection of transmission lines using complex wavelets analysis. *IEEE Trans. on Power Delivery*, 18(3):705–710, Jul., 2003.

[107] Q. H. Wu, J. F. Zhang, and D. J. Zhang. Ultra-high-speed directional protection of transmission lines using mathematical morphology. *IEEE Trans. on Power Delivery*, 18(4):1127–1133, Oct., 2003.

[108] E. Clarke. *Circuit Analysis of AC Power Systems*, volume I. New York: Wiley, 1943.

[109] D. Woodford. *Introduction to PSCAD/EMTDC V3.* Manitoba HVDC Research Center Inc., Winnipeg, Manitoba, Canada, Mar., 2000.

[110] A. M. Gole, O. B. Nayak, T. S. Sidhu, and M. S. Sachdev. A graphical electromagnetic simulation laboratory for power systems engineering programs. *IEEE Trans. on Power Systems*, 11(2):599–606, 1996.

[111] V. Pathirana and P. G. McLaren. A hybrid algorithm for high speed transmission line protection. *IEEE Trans. on Power Delivery*, 20(4):2422–2428, Oct., 2005.

[112] D. D. Sabin and A. Sundaram. Quality enhances reliability. *IEEE Spectrum*, 33(2):34–41, Feb., 1996.

[113] R. C. Dugan and M. F. McGranaghan. *Electric Power Systems Quality.* 1996.

[114] G. T. Heydt. Electric power quality: A tutorial introduction. *IEEE Computer Applications in Power*, 11(1):15–19, 1998.

[115] A. Domijan, G. T. Heydt, A. P. S. Meliopoulos, S. S. Venkata, and S. West. Directions of research on power quality. *IEEE Trans. on Power Delivery*, 8(1):429–436, Jan., 1993.

[116] J. Douglas. Solving power quality problems. *EPRI Journal*, 18(8):6–15, Dec., 1993.

[117] C. J. Melhorn and M. F. McGranaghan. Interpretation and analysis of power quality measurements. *IEEE Trans. on Industry Applications*, 31(6):1363–1370, Nov.-Dec., 1995.

[118] L. Cristaldi and A. Ferrero. A method and related digital instrument for the measurement of the electric power quality. *IEEE Trans. on Power Delivery*, 10(3):1183–1189, Jul., 1995.

[119] P. Daponte, A. Falcomata, and A. Testa. A multiple attenuation frequency window for harmonic analysis in power systems. *IEEE Trans. on Power Delivery*, PD-9(2):863–871, Apr., 1994.

[120] G. T. Heydt. *Electrical Power Quality.* West Lafayette, IN: Stars in a Circle Publications, 1991.

[121] G. T. Heydt. Electrical power quality: a tutorial introduction. *IEEE Computer Applications in Power*, 11(1):15–19, Jan., 1998.

[122] IEEE Standards Coordinating Committee 22 on Power Quality. Iece recommended practice for monitoring electric power quality. *IEEE Std 1159-1995*, Nov., 1995.

[123] CEMP-SP. Adp/computer electrical installation and inspection for command control, communications, computer, intelligence, surveillance, and reconnaissance (c4isr) facilities. *Army Technical Manual TM5-689*, Sep., 2001.

[124] ANSI C84.1-1995. Electric power systems and equipment-voltage ratings (60 hz). 1995.

[125] IEEE 519-1992. Ieee recommended practices and requirements for harmonic control in electrical power systems. Apr., 1993.

[126] IEEE P1159/D6. Recommended practice on monitoring electric power quality. Dec., 1994.

[127] S. Santoso, E. J. Powers, W. M. Grady, and P. Hofmann. Power quality assessment via wavelet transform analysis. *IEEE Trans. on Power Delivery*, 11(2):924–930, Apr., 1996.

[128] P. Pillay and A. Bhattachariee. Applicaition of wavelets to model short-term power system disturbances. *IEEE Trans. on Power Delivery*, 11(4):2231–2237, Nov., 1996.

[129] D. C. Robertson, O. I. Camps, J. S. Mayer, and W. B. Gish. Wavelets and electromagnetic power system transients. *IEEE Trans. on Power Delivery*, 11(2):1050–1057, Apr., 1996.

[130] J. Serra and P. Soille. *Mathematical Morphology and Its Application to Image Processing.* Kluwer Academic Publishers, The Netherlands, 1994.

[131] Q. H. Wu, J. F. Zhang, and D. J. Zhang. Ultra-high-speed directional protection of transmission lines using mathematical morphology. *IEEE Trans. on Power Delivery*, 18(4):1127–1133, Oct., 2003.

[132] A. K. Ghosh and D. L. Lubkeman. The classification of power system disturbance waveforms using a neural network approach. *IEEE Trans. on Power Delivery*, 10(109-115), Jan., 1995.

[133] S. Santoso, J. Lamoree, W. M. Grady, E. J. Powers, and S. C. Bhatt. A scalable pq event identification system. *IEEE Trans. on Power Delivery*, 15:738–743, Apr., 2000.

[134] L. Angrisani, P. Daponte, M. D'Apuzzo, and A. Testa. A measurement method based on the wavelet transform for power quality analysis. *IEEE Trans. on Power Delivery*, 13(4):990–998, Oct., 1998.

[135] IEEE Task Force. Effects of harmonics on equipment. *IEEE Trans. on Power Delivery*, 8(2):672–680, Apr., 1993.

[136] NJ: Prentice-Hall E. O. Brigham. *The Fast Fourier Transform.* Englewood Cliffs, 1974.

[137] N. E. Huang, S. R. Long, and Z. Shen. The mechanism for frequency downshift in nonlinear wave evolution. *Adv. Appl. Mech.*, 32:59–117, 1996.

[138] N. E. Huang, S. R. Long, M. C. Wu, H. H. Shih, Q. Zheng, N. C. Yen, C. C. Tung, and H. H. Liu. The empirical mode decomposition and the hilbert spectrum for nonlinear and nonstationary time series analysis. *Proc. R. Soc. London, Series A*, 454:903–995, 1998.

[139] N. E. Huang, Z. Shen, and S. R. Long. A new view of nonlinear water waves - the hilbert spectrum. *Ann. Rev. Fluid Mech.*, 31:417–457, 1999.

[140] H. Akagi. New trends in active filters for power conditioning. *IEEE Trans. on Industry Applications*, 32(6):1312–1322, Nov., 1996.

[141] R. A. Gabel and R. A. Roberts. *Signal and Linear Systems.* John Wiley and Sons, 3rd edition, 1987.

[142] V. K. Jain, W. L. Collins, and D. C. Davis. High-accuracy analog measurement via interpolated fft. *IEEE Trans. on Instrument Measurement*, 26(6):113–122, Jun., 1979.

[143] H. Akagi and Y. Kapazawa. Instantaneous reactive pawer compensators comprising switching devices without energy storage components. *IEEE Trans. on Industry Applications*, 120(3):625–630, May/Jun., 1984.

[144] H. Fujita and H. Akagi. A practical approach to harmonic compensation in power systems - series connection of passive and active filters. *IEEE Trans. on Industry Applications*, 27(6):1020–1025, Nov./Dec., 1991.

[145] F. Peng, G. Ott, and D. Adams. Harmonic and reactive power compensation based on the generalized instantaneous reactive power theory for three-phase four-wire systems. *IEEE Trans. on Power Electronics*, 13(6):1174–1181, Nov., 1998.

[146] G. Andria and M. Savino. Windows and interpolation algorithms to improve electrical measurement accuracy. *IEEE Trans. on Instrument Measurement*, 38(4):856–863, Aug., 1989.

[147] Q. Wang, W. Yao, and Z. Wang. A study about influence of high and low pass filters on detecting effect of harmonics detection circuits. *Trans. of China Electrotechnical Society*, 14(5):22–26, Apr., 1999.

[148] IEC Standard 61000-4-7. General guide on harmonics and interharmonics measurements. 2002.

[149] J. Liu, J. Yang, and Z. Wang. A new approach for single-phase harmonic current detecting and its application in a hybrid active power filter. *Industrial Electronics Society, IECON '99 Proceedings, The 25th Annual Conference of the IEEE*, 2:849–854, Nov. 29-Dec. 3, 1999.

[150] Cadick corporation. *Technical Bulletin 004a: Ferroresonance*, May, 2002.

[151] Kevin Jacobs. Control of ferroresonance. *Technical Guidance Note*, 2, Jul., 2001.

[152] P. J. Burt and E. H. Adelson. The laplacian pyramid as a compact image code. *IEEE Trans. on Communications*, 31:532–540, 1983.

[153] John Goutsias and H. J. A. M. Heijmans. Nonlinear multiresolution signal decomposition schemespart i: Morphological pyramids. *IEEE Trans. on Image Processing*, 9, 2000.

[154] H. J. A. M. Heijmans and John Goutsias. Nonlinear multiresolution signal decomposition schemes-part ii: Morphological wavelets. *IEEE Trans. on Image Processing*, 9(11):1897–1913, Nov., 2000.

[155] S. Mallat. A wavelet tour of signal processing. CA: Academic, San Diego, 1998.

[156] A. C. Kamath and I. K. Fodor. *Undecimated Wavelet Transforms For Image Denoising.* Technical report, Lawrence Livermore National Laboratory, 2002.

[157] W. Sweldens. The lifting scheme: A custom-design construction of biorthogonal wavelets. *Application computer harmon. anal.*, 3(2):186–200, 1996.

[158] W. Sweldens. The lifting scheme: A construction of second generation wavelets. *SIAM J. Math. Anal.*, 29(2):511–546, 1997.

[159] P. Schroder and W. Sweldens. Spherical wavelets: Effciently representing functions on the sphere. *Computer Graphics Proceedings (SIGGRAPH 95)*, pages 161–172, 1995.